Universidade Federal do Rio Grande - FURG

Instituto de Oceanografia

Programa de Pós-Graduação em Oceanologia

Physical-biological interactions in the Northern Humboldt Upwelling Current System and the consequences to the absorption of carbon

Rodrigo Mogollón Aburto

Orientador: Prof. Dr. José Luiz Lima de Azevedo

Rio Grande, RS, Brasil

Maio 2019

Rodrigo Mogollón Aburto

Laboratório de Dinâmica e Modelagem Oceânica (DinaMO)

Physical-biological interactions in the Northern Humboldt Upwelling Current System and the consequences to the absorption of carbon

Tese apresentada ao Instituto de Oceanografía da Universidade Federal do Rio Grande (FURG), para a obtenção de Título de Doutor em Oceanología

Orientador: José Luiz Lima de Azevedo

Rio Grande, RS, Brasil

Maio 2019

Mogollón Aburto, Rodrigo

Physical-biological interactions in the Northern Humboldt Upwelling Current System and the consequences to the absorption of carbon 131 páginas

Tese (Doutorado) - Instituto de Oceanografía da Universidade Federal do Rio Grande (FURG).

1. Humboldt Current System
2. Climate Change
3. Primary production
4. Air-sea CO_2 fluxes
5. Seawater pCO_2

Instituto de Oceanografía da Universidade Federal do Rio Grande (FURG), 2019

UNIVERSIDADE FEDERAL DO RIO GRANDE - FURG
IO – INSTITUTO DE OCEANOGRAFIA
PROGRAMA DE PÓS-GRADUAÇÃ0 EM OCEANOLOGIA
E-mail: ccpofqg@furg.br – home-page: www.ppgo.furg.br

ATA ESPECIAL DE DEFESA DE TESE DE DOUTORADO – 02/2019

Às quatorze horas do dia vinte e sete de maio do ano dois mil e dezenove , na Sala Reuniões – IO - FURG/Carreiros, reuniu-se a Comissão Examinadora da Tese de **DOUTORADO** intitulada **"INTERAÇÕES FÍSICO-BIOLÓGICAS EM REGIÕES DE RESSURGÊNCIA COSTEIRA: CONSEQUÊNCIAS PARA A ABSORÇÃO DE CARBONO PELO OCEANO"**, do **Acad. RODRIGO MOGOLLÓN ABURTO** . A Comissão Examinadora foi composta pelos seguintes membros: Prof. Dr. José Luiz Lima de Azevedo- Orientador/Presidente – (IO/FURG), Prof. Dr. Rodrigo Kerr - (IO/FURG), Prof. Dr. Mauricio Magalhães Mata – (IO/FURG) e Prof. Dr. Leopoldo Rota de Oliveira – (UNIPAMPA) . Dando início à reunião, o Coordenador do Programa de Pós-Graduação em Oceanologia, e membro da Banca, Prof. Dr. Rodrigo Kerr, agradeceu a presença de todos e fez a apresentação da Comissão Examinadora. Logo após esclareceu que o Candidato teria um tempo de 45 a 60 min para explanação do tema, e cada membro da Comissão Examinadora, um tempo máximo de 30 min para perguntas. A seguir, passou à palavra ao Candidato que apresentou o tema e respondeu às perguntas formuladas. Após ampla explanação, a Comissão Examinadora reuniu-se em reservado para discussão do conceito a ser atribuído ao Candidato. Foi estabelecido que as sugestões de todos os membros da Comissão Examinadora, que seguem em pareceres em anexo, foram aceitas pelo Orientador/Candidato para incorporação na versão final da Dissertação. Finalmente, a Comissão Examinadora considerou o candidato **APROVADO,** por unanimidade. Nada mais havendo a tratar, foi lavrada a presente ATA que após lida e aprovada, será assinada pela Comissão Examinadora, pelo Candidato e pelo Coordenador do Programa de Pós-Graduação em Oceanologia.

Prof. Dr. José Luiz L. de Azevedo
Presidente

Prof. Dr. Rodrigo Kerr

Prof. Dr. Mauricio Magalhães Mata

Prof. Dr. Leopoldo Rota de Oliveira

Acad. Rodrigo Mogollón Aburto

Prof. Dr. Rodrigo Kerr
Coordenador do PPGO

Dedico esta tesis a mis padres, Juan Carlos y Elena,
quienes con su apoyo y cariño lo hicieron nuevamente posible.

"Lo único que sé es que, hasta ahora, a mi nadie me ha ganado"

—Juan Carlos M. B.

Agradecimentos

Agradezco a la agencia de fomento CAPES, al programa de posgraduación en Oceanología de la FURG y a todos aquellos quienes fueron mis profesores y colegas durante estos 6 años y, en particular, el haber tenido un orientador taõ foda como siempre demostró serlo.... infinitamente agradecido por tu tiempo, tus enseñanzas, tus consejos y también por tus geniales, pero cuestionables, costumbres. Mogollón & Calil es un dupla que dificilmente olvidaré, pues formaste un robusto criterio científico en mi, del cual maliciosamente disfruto hasta hoy, obrigado, Paulo!. También agradecer muy en especial a tres de mis colegas, Rafael, Claus y Luiz, por soportarme a diario y por tan nutritivas discusiones. A mi hno. mono Ricardo H. quien vino a visitarme, aunque casi al final, siempre será bienvenido tu compañerismo y carisma, buen gallo, compadre!. Lorena, gracias por cuidar de mi sensible cabeza, perdona por darte tamaña responsabilidad, la cual supiste llevar con entereza e inteligencia. A ti, mucho de este trabajo te lo atribuyo. Kusi, gracias por cuidar de mi hogar, perdona por darte tamaña responsabilidad, la cual supiste llevar con bravura y mucha paciencia. A ti, mucha de mi cordura te la atribuyo, vámonos?. A mi hermosa familia, quienes vinieron a visitarme dos veces durante esta aventura, apaciguando y oxigenándome el alma...y hasta cuando el simple hecho de regresar a casa en cada fin de año significaba estar de vacaciones. A ustedes, nuestro apellido en Google Académico. Quisiera agradecer al prof. José Luiz L.A., de quien aprendí mucho y me dió su aprobación para calificar de doctor. Circunstancias nos llevó a que él tomara mi orientación casi al final de mis estudios, aceptando ser mi asesor y apoyo en esta recta final.

Contents

List of Figures

List of Tables

Acronyms

Alk Alkalinity

C-GLORS V.4 Global Ocean Reanalysis System

CbPM Carbon-based Production Model

CCMP V.2 Cross Calibrated Multi Platform

CMCC Centro Euro-Mediterrano sui Cambiamenti Climatici

CS Current System

CT2016 NOAA's CarbonTracker

DIC Dissolved Inorganic Carbon

EBUS Eastern Boundary Upwelling System

ECMWF European Centre for Medium-Range Weather Forecasts

EKE Eddy Kinetic Energy

ENSO El Niño Southern Oscillation

ESP Eastern South Pacific

ETP Eastern Tropical Pacific

EUC Equatorial Undercurrent

FW Freshwater

GLODAP v2.2016b Global Ocean Data Analysis Project

GR Growth Rate

HR high resolution

ICEN Indice Costero El Niño

j-OFURO V.3 Japanese Ocean Flux Data Sets with Use of Remote Sensing Observations

LR low resolution

MERRA2 Modern Era Retrospective-Analysis for Research and Applications

MLD Mixed Layer Depth

MODIS Moderate-resolution Imaging Spectro radiometer

NHCS Northern Humboldt Current System

NL Nutrient Limitation

NODC National Oceanographic Data Center

NPZD Nutrient-Phytoplankton-Zooplankton-Detritus

OCMIP Ocean Carbon-Cycle Model Intercomparison Project

OMZ Oxygen Minimum Zone

PAR Photosynthetically Active Radiation

PCC Peruvian Coastal Current

PCUC Peru-Chile Countercurrent

PISCES V.1 Pelagic Interaction Scheme for Carbon and Ecosystem Studies

PP Primary Production

pSSCC Primary Southern Subsurface Countercurrents

QuickSCAT NASA's Quik Scatterometer

ROMS-AGRIF Regional Oceanic Modeling System

RT Residence times

SEC South Equatorial Current

sSSCC Secondary Southern Subsurface Countercurrents

SST sea surface temperature

T Temperature

TRMM_TMI V.3 Tropical Rainfall Measuring Mission

UI upwelling Index

WHOI OAFlux V.3 Woods Hole Oceanographic Institute's objectively analyzed air-sea heat fluxes

WOA 2013 V.2 World Ocean Atlas

WOCE World Ocean Circulation Experiment

ZEU euphotic zone

Abstract

It has been hypothesized that global warming will strengthen upwelling-favorable winds in the Northern Humboldt Current System (NHCS) as a consequence of the increase of the land-sea thermal gradient along the Peruvian coast. The effect of strengthened winds in this region is assessed with the use of a coupled physical-biogeochemical model forced with projected and climatological winds. Strengthened winds induce an increase in primary production of 2% per latitudinal degree from 9.5°S to 5°S. In some important coastal upwelling sites primary production is reduced. This is due to a complex balance between nutrient availability, nutrient use efficiency, as well as eddy- and wind-driven factors. Mesoscale activity induces a net offshore transport of inorganic nutrients, thus reducing primary production in the coastal upwelling region. Wind mixing, in general disadvantageous for primary producers, leads to shorter residence times in the southern and central coastal zones. Overall, instead of a proportional enhancement in primary production due to increased winds, the NHCS becomes only 5% more productive ($+5$ mol C m^{-2} $year^{-1}$), 10% less limited by nutrients and 15% less efficient due to eddy-driven effects. It is found that regions with an initial strong nutrient limitation are more efficient in terms of nutrient assimilation which makes them more resilient in face of the acceleration of the upwelling circulation.

We use the same coupled physical–biogeochemical model to investigate the drivers and mechanisms responsible for the spatiotemporal variability of the partial pressure of carbon dioxide in seawater (pCO_2) and associated air–sea CO_2 fluxes in the NHCS. Simulated pCO_2 is in good agreement with available observations with an average

absolute error of, approximately, 24 μatm. The highly productive upwelling region, 300 km from the shore and between 5 and 17°S, is shown to be a strong CO_2 source with an averaged flux of 5.60 $\pm$ 2.94 mol C m^{-2} year^{-1}, which represents an integrated carbon flux of 0.028 $\pm$ 0.015 Pg C year^{-1}. Through a series of model experiments we show that the high pCO_2 is primarily the result of coastal upwelling, which is incompletely compensated by biology. Specifically, the supply of dissolved inorganic carbon (DIC)-rich waters to the surface pushes pCO_2 up to levels around 1100 μatm. Even though biological production is high, it reduces pCO_2 only by about 300 μatm. We show that this relatively low degree of biological compensation, which implies an inefficient biological pump in the nearshore domain, results from a spatio-temporal decoupling between the counteracting effects of biological production and the transport and mixing of DIC. The contribution of the outgassing and the processes affecting CO_2 solubility, associated with the seasonal cycle of heating and cooling, are minor. Across the whole domain, the balance of mechanisms is similar, but with smaller amplitudes. We demonstrate that seawater pCO_2 is more sensitive to changes in DIC and sea surface temperature, while alkalinity plays a minor role.

The role played by El Niño-Southern Oscillation (ENSO) on modulating the oceanic carbon emittance is assessed. pCO_2^{sw} was inferred from a recent neural network methodology forced with outputs from a coupled physical-biogeochemical hindcast, which permits to reconstruct the interannual variability of pCO_2^{sw} and associated air-sea CO_2 fluxes from 1998 through 2015 at monthly timescales. Results show a large spatiotemporal variability of the CO_2 exchange to nine El Niño and La Niña episodes throughout the period of analysis and within the coastal and equatorial upwelling region that variability results from combined ENSO-driven ΔpCO_2 and wind speed

variations. It is found that the relatively weak CO_2 source behavior during an average Niño episode is mainly caused by a decrease of ΔpCO_2 which is partially compensated by more efficient gas exchange at the air-sea interface due to the strengthening of the upwelling-favorable winds, therefore increasing the CO_2 transfer velocity. Conversely, the strong CO_2 source behavior during an average La Niña episode results from more efficient upwelling which brings colder and CO_2-rich waters to the surface, thus increasing pCO_2^{sw} and the associated CO_2 efflux. Moreover, it is estimated that during an average El Niño episode the total amount of carbon retained within the coastal and equatorial upwelling region in the NHCS is about half a million metric tons of carbon that normally would have been lost to the atmosphere as CO_2. In contrast, during an average La Niña episode, one million metric tons of carbon is additionally emitted, largely contributing to the atmospheric CO_2 accumulation.

Keywords: Bakun's hypothesis, build up of atmospheric CO_2, eddy-driven effects, global warming-induced wind intensification, latitudinal variability of primary production, response of biological production, partial pressure of carbon dioxide (pCO_2), air–sea CO_2 fluxes, spatiotemporal variability of pCO_2, CO_2-carbonate system, Northern Humboldt Current System, ENSO-induced CO_2 flux variability, inferred interannual pCO_2.

Resumo

Trabalhos anteiores trazem como hipótese que o aquecimento global sería responsável por intensificar os ventos favoráveis à ressurgência no Sistema Norte da Corrente do Humboldt (NHCS), sendo consequência do aumento do gradiente termal continente-oceano adjacente ao longo da costa Peruana. O efeito dos ventos intensificados nesta região é avaliado por meio do uso de um modelo acoplado físico-biogeoquímico forçado com ventos perturbados e climatológicos. Resultados mostram que os ventos intensificados induzem um acréscimo na produção primaria de 2% por grau de latitude entre 9.5°S e 5°S. Em alguns importantes centros de ressurgência costeira a produção primaria é reduzida. Isso ocorre devido a um complexo balanço entre a disponibilidade dos nutrientes, a eficiência do uso dos nutrientes, bem como os fatores turbulentos e fatores associados ao vento. A atividade de mesoescala induz um transporte liquido dos nutrientes inorgânicos em direção ao oceano aberto, reduzindo assim a produção primaria na região da ressurgência costeira. A mistura induzida pelo vento leva a tempos de residência mais curtos na zona costeira sul e central, os quais são geralmente desvantajosos para os produtores primários. Em geral, ao invés de obter um acréscimo da produção primaria proporcional à intensificação dos ventos favoráveis, o NHCS torna-se apenas 5% mais produtivo ($+5$ mol C m^{-2} $year^{-1}$), 10% menos limitado pelos nutrientes, além de 15% menos eficiente devido a fatores turbulentos. É encontrado que as regiões com forte limitação inicial de nutrientes são mais eficientes em termos da assimilação dos mesmos, indicando que estas sejam mais resilientes perante a aceleração da circulação de ressurgência.

Dando prosseguimento, investigou-se os controladores e mecanismos responsáveis pela variabilidade espaço-temporal da pressão parcial do dióxido de carbono na agua do mar (pCO_2) e dos associados fluxos do CO_2 na interface ar-mar no NHCS. A pCO_2 simulada representa bem as observações com um erro absoluto medio de, aproximadamente, 24 μatm. A região de ressurgência altamente produtiva, até os 300 km distante da costa, entre 5°S e 17°S, mostra ser uma forte fonte de CO_2 com um fluxo medio de 5.60 $\pm$ 2.94 mol C m^{-2} $year^{-1}$, a qual representa um fluxo de carbono integrado de 0.028 $\pm$ 0.015 Pg C $year^{-1}$. Mediante uma série de experimentos demonstramos que os altos valores da pCO_2 são causados principalmente pela ressurgência costeira, a qual é incompletamente compensada pela biologia. Em particular, o suprimento de águas ricas em carbono inorgânico dissolvido (DIC) à superficie leva os valores da pCO_2 até 1100 μatm. Embora uma alta produção primaria, a biologia contribui reduzindo a pCO_2 em apenas 300 μatm. Mostramos que este relativo baixo nível de compensação biológica, o qual sugere uma ineficiente bomba biológica no dominio costeiro, resulta de um desacoplamento entre os efeitos opostos da produção biológica e o transporte e mistura do DIC. A contribuição da desgasificação e dos processos que afetam a solubilidade do CO_2, associados ao ciclo sazonal de aquecimento e resfriamento, são menores. Através de todo o dominio, o balanço dos mecanismos é similar, mas de amplitudes menores. Demonstramos também que a pCO_2 é mais sensitiva às variações em DIC e SST, enquanto a alkalinidade desempenha um papel menor.

Além do mais, o papel do El Niño-Southern Oscillation (ENSO) na modulação da emissão oceânica do carbono foi investigado. A pCO_2 foi inferida usando uma recente metodologia de redes neurais, a qual foi forçada com saídas de simulações de um modelo acoplado físico-biogeoquímico, que por sua vez permite reconstruir

a variabilidade interanual e os fluxos associados desde 1998 até 2015 em escalas mensais. Resultados mostram uma larga variabilidade espaço-temporal das trocas do CO_2 devido a nove episódios El Niño e La Niña ao longo do periodo de análises. Dentro da região da ressurgência equatorial e costeira, essa variabilidade é resultado do efeito combinado das variações na ΔpCO_2 e na velocidade do vento, ambas induzidas pelo ENSO. Foi encontrado que o comportamento de fraca fonte de CO_2 durante um episódio medio de El Niño é principalmente causado por um decréscimo da ΔpCO_2, a qual é parcialmente compensada por uma maior eficiência nas trocas de CO_2 na interface ar-mar devido à intensificação dos ventos. Em contraste, o comportamento de forte fonte de CO_2 durante um episódio medio de La Niña está relacionado a uma ressurgência mais eficiente do que condições neutrais, a qual leva águas mais frias e mais ricas em CO_2 para a superficie induzindo um acréscimo da pCO_2 e dos fluxos do CO_2. Ademais, é estimado que durante um episódio medio de El Niño a quantia de carbono retido dentro da região costeira e equatorial é aproximadamente meio milhão de toneladas métricas de carbono que normalmente deveriam ser emitidas a mais para atmosfera. Em contraste, durante um episódio medio de La Niña, um milhão de toneladas métricas de carbono são adicionalmente emitidas contribuindo largamente para a acumulação do CO_2 atmosférico.

Palavras-chave: Hipótese de Bakun, aumento do CO_2 atmosférico, efeitos turbulentos, intensificação dos ventos devido ao aquecimento global, variabilidade latitudinal da produção primaria, resposta da produção biológica, pressão parcial do dióxido de carbono (pCO_2), fluxos ar-mar de CO_2, variabilidade espaço-temporal da pCO_2, sistema carbonato-CO_2, Sistema Norte da Corrente do Humboldt, variabilidade da pCO_2 induzida pelo ENSO, pCO_2 interanual inferida.

Chapter I

Introduction

The Northern Humboldt Current System (NHCS) located at the Eastern Tropical Pacific (ETP) in front of the Peruvian coast, sustains high levels of biological productivity due to yearlong upwelling-favorable southeast Trade Winds, which induce the vertical advection of cold, nutrient-rich and oxygen-poor waters from relatively shallow depths (Strub et al., 1998, 2013). The low-latitude of the NHCS allows a strong upwelling circulation due to larger offshore Ekman transport but also makes it very sensitive to equatorial oceanic perturbations, such as El Niño Southern Oscillation (ENSO) (Sanchez et al., 2000; Colas et al., 2008; Montes et al., 2011; Mogollón e Calil, 2017). The NHCS is recognized as one of the most important Eastern Boundary Upwelling System (EBUS), which are the most productive regions of the world's oceans (Pauly e Christensen, 1995; Carr, 2001; Carr e Kearns, 2003). EBUS's are very sensitive to climate perturbations particularly in terms of ocean acidification, surface warming, and deoxygenation trends (Stramma et al., 2008; Gruber, 2011; Bakun et al., 2015). They are naturally more acidic than most of the surface ocean due to their high carbon and low oxygen contents. This can potentially induce changes in

species composition as a consequence of climate change (Hauri et al., 2009; Doney et al., 2011), rendering these systems key coastal regions to evaluate other potential consequences by understanding the biogeochemical role on the CO_2-carbonate system and its vulnerability. EBUS's contribute very significantly to the gas exchange between the ocean and the atmosphere, particularly with respect to atmospheric CO_2. While some EBUS's are strong sinks of atmospheric CO_2 (e.g the U.S Pacific coast off Oregon (Hales et al., 2005; Borges et al., 2005) others are shown to be strong sources of CO_2 (Chavez et al., 1999; Feely et al., 2002, 2006). In fact the NHCS is one of the regions with the highest seawater pCO_2 worldwide (Friederich et al., 2008; Takahashi et al., 2009), but the extent and magnitude of this source nature of CO_2 has not yet been quantified. Identifying and quantifying the underlying processes that control seawater pCO_2 in this important EBUS is essential for a more accurate assessment of the marine carbon cycle at regional and global scales. By doing so, we will be able to quantify changes in seawater pCO_2 induced by climate variations of the drivers in the region. For example, Doney et al. (2009) found that the biological export and thermal solubility effects on pCO_2 act to damp partially the circulation-driven biogeochemical variability in the tropical region. Turi et al. (2014) explained the neutral nature of air-sea CO_2 flux in the California Current System based on the fact that the uptake CO_2 flux in the offshore region compensates the outgassing in the nearshore band on an annual scale. On the other hand, another by-product of climate perturbations that also directly affect EBUS's is the acceleration of the upwelling circulation, which is a direct consequence of the increase of upwelling-favorable winds. This hypothesis was initially proposed by Bakun (1990), who anticipated that the increase in anthropogenic greenhouse gases, such as CO_2, would lead to the intensification of coastal upwelling in EBUS's, particularly in the NHCS. This is due to an

increase in the land-sea thermal gradient that has been occurring as a consequence of global warming in several EBUS's (Sydeman et al., 2014) (see section1). Lachkar e Gruber (2013) explored the response of biological production and air-sea CO_2 fluxes to the upwelling intensification in two EBUS's, namely the California and the Canary Current System using a Nutrient-Phytoplankton-Zooplankton-Detritus (NPZD)-type ecosystem model. They found that a doubling of the wind stress magnitude doubles primary production in the southern California and central/northern Canary Current System (CS), while in the central/northern California and southern Canary CS the increase in primary production in response to the same wind variation is more modest.

On the other hand, the proximity of the NHCS to the Equator renders it extremely sensitive to basin-scale modes of climate variability. The warm phase of ENSO, El Niño, is commonly associated with several negative environmental disturbances and adverse effects on nutrient supply and primary production rates (Barber e Kogelschatz, 1990), rendering the Peruvian coast a marine ecosystem characterized by transient unfavorable conditions in terms of fishery productivity (Ñiquen e Bouchon, 2004). However, El Niño may be considered as a favorable event in terms of Earth's climate. For instance, as evaporation requires large amounts of thermal energy, an El Niño episode tends to cool the ocean due to larger rates of evaporation that are induced in the Eastern Pacific (Trenberth et al., 2002). Moreover, Bakun e Weeks (2008) suggest that El Niño re-starts the Peruvian marine ecosystem from an initial highly productive state, thus interrupting any longer-lived nonlinear adverse feedback. Additionally, the NHCS goes through an oxygenated phase during El Niño (Montes et al., 2014; Espinoza Morriberón et al., 2018) modulating the spatiotemporal variability of the oxygen minimum zone. As a consequence, the physical ventilation that suppress

suboxic processes during El Niño peaks, would lead to a substantial reduction of coastal outgassing of nitrous oxide gas (N_2O) to the atmosphere (Mogollón e Calil, 2017), which is a well-known greenhouse gas with a warming potential 300 times larger than CO_2. Together with a N_2O efflux decrease, an anomaly ocean CO_2 uptake response or a significant reduction of the average CO_2 outgassing during El Niño conditions is well documented in several studies (Inoue e Sugimura, 1992; Feely et al., 1995; Rayner et al., 1999; Jones et al., 2001; McKinley et al., 2004; Doney et al., 2009; Rödenbeck et al., 2014; Brady et al., 2019). In spite of the fact that the lack of consistent low-frequency pCO_2^{sw} measurements and the paucity of spatially comprehensive observations do not allow a robust characterization of the long-term variability in the coastal region of the NHCS, limited available observations indicate that the CO_2 source behavior is significantly influenced by ENSO phenomena. However, the average effect has not been well quantified because the majority of studies focus on the Equatorial/Tropical Pacific oceanic region. For instance, Feely et al. (1997) found lower values of ΔpCO_2 in the central and eastern equatorial region during 1991-1994 ENSO period. Similarly, Feely et al. (1999) showed a reduction of the regional air-sea CO_2 flux in the equatorial Pacific region during the 1991-1994 El Niño period. Chavez et al. (1999) also found that during the 1997-1998 El Niño, the equatorial Pacific Ocean retained 0.7 Pg C.Rödenbeck et al. (2014) demonstrated a reduced CO_2 outgassing during El Niño events in the Tropical Pacific, and its magnitude depends on the relative contributions of the physical-biogeochemical caused responses. Studies undertaken in other EBUS, such as the California Current System (Chavez et al., 1999; Friederich et al., 2002), demonstrated a switching from sink to source during ENSO events. However, the Humboldt EBUS does not appear to shift to a CO_2 sink nature in response to ENSO-driven perturbations.

In this work we assess the effect of intensifying winds on primary production in the NHCS and the associated biological response in a climatological sense. Our methodology follows that of Lachkar e Gruber (2013) in that we simulate the upwelling intensification trend using an idealized experiment which consists in varying the wind forcing. Based on previous modeling studies (Doney et al., 2009; Turi et al., 2014; Arruda et al., 2015), it is also presented the first eddy-resolving (9 km) modelling work focusing on seawater pCO_2 in the NHCS. We quantify the contribution of the main drivers of seawater pCO_2, which are Dissolved Inorganic Carbon (DIC), Temperature (T), Alkalinity (Alk), and Freshwater (FW). In addition, the mechanisms that control pCO_2 variability, namely biology, air-sea CO_2 fluxes, CO_2 solubility and circulation, are also investigated by means of model sensitivity experiments. In addition, the contribution of changes in wind speed, CO_2 content, and the cross-correlations between them to the interannual air-sea CO_2 flux anomalies are diagnosed. Thus, this is the first attempt to estimate how much carbon, as CO_2, is retained or released throughout an average ENSO episode in the most productive coastal and adjacent equatorial upwelling region. A better understanding of how the carbon cycle responds to ENSO may provide valuable insight into how the NHCS may respond to future climate change since it resembles an El Niño-like warming pattern (Meehl e Washington, 1996).

1 Upwelling intensification

In 1990, Andrew Bakun proposed that increasing greenhouse gas concentrations, such as CO_2 would force intensification of upwelling-favorable winds in EBUS's (see Fig. I.1). The mechanism works as follows:

In normal conditions, a thermal low pressure cell is developed at the continental mass and a high pressure zone at the adjacent ocean. This is primarily due to the increased heating on land during the day and cooling at night when compared to the adjacent ocean. However, in a global-warming scenario, the accumulation of anthropogenic greenhouse gases would lead to an inhibition of the night-time radiative cooling, resulting in an enhancement of the daytime heating. This would induce to an intensification of the continental thermal lows adjacent to the upwelling regions. The consequences of this intensification would be (i) an increased cross-shore atmospheric pressure gradient, (ii) the subsequent intensification of the alongshore geostrophic wind that drives an offshore Ekman transport at the surface layer and, (iii) the general acceleration of the coastal upwelling circulation. Bakun's hypothesis tends to be a Spring-Summer phenomenon in the subtropics, while in Peru it becomes a year-round phenomenon due to its proximity to the Equator (Bakun e Weeks, 2008).

2 CO_2-carbonate system

At the present time, CO_2 is recognized as the most important greenhouse gas, which absorbs infrared energy radiated back from the Earth surface resulting in an increase in the temperature of the troposphere. The continued burning of fossil fuels will continue to increase the CO_2 in the atmosphere at a nearly similar rate, thus, this anthropogenic CO_2 will tend to increase its flux across the air-sea interface rendering that the oceans play a major role in its storage globally. The oceans stores about 60 times as much carbon as the atmosphere (Tanhua et al., 2013) and they are thought to take up about 40% of the CO_2 produced anthropogenically, i.e. from the burning

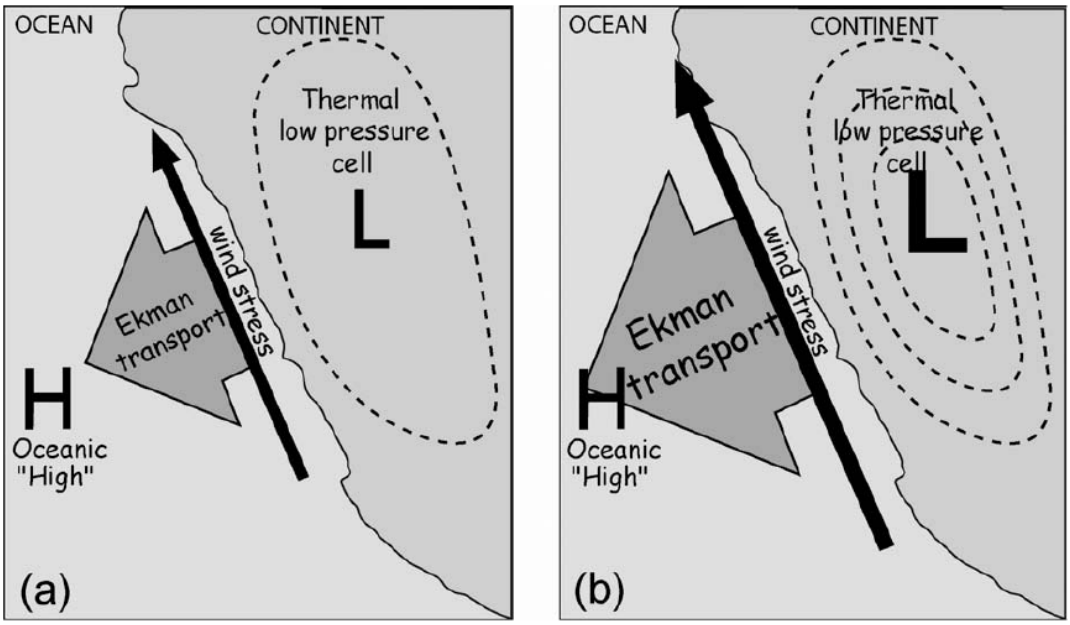

Figure I.1: Diagram of upwelling intensification mechanism: (a) a "thermal" low-pressure cell builds up over the coastal landmass due to heating of the continental surface relative to the more slowly heating ocean, exerting equatorward geostrophic wind stress on the sea surface that, in turn, drives offshore-directed Ekman transport of ocean surface water and corresponding upwelling of deeper waters required to replace the surface waters transported offshore; (b) buildup of greenhouse gases in the atmosphere inhibits nighttime cooling of the heated coastlands, increasing average intensity of the coastal low-pressure cell and associated upwelling-favorable wind, which in terms drives quadratic (or greater) increases in offshore surface transport and resulting upwelling. Adapted from Bakun e Weeks (2008)

of fossil fuels (Millero, 2007). The absorption of CO_2 by seawater and subsequent equilibrium reactions within this medium give rise to a complex chemical system, here referred to as the seawater CO_2-carbonate system (see Fig.I.2).

In the ocean, carbon dioxide exists in three different inorganic forms: as free carbon dioxide, $CO_2(aq)$ = aqueous carbon dioxide, as bicarbonate, HCO_3^-, and as carbonate ion, CO_3^{2-} A fourth form is H_2CO_3 (true carbonic acid), however its concentration is

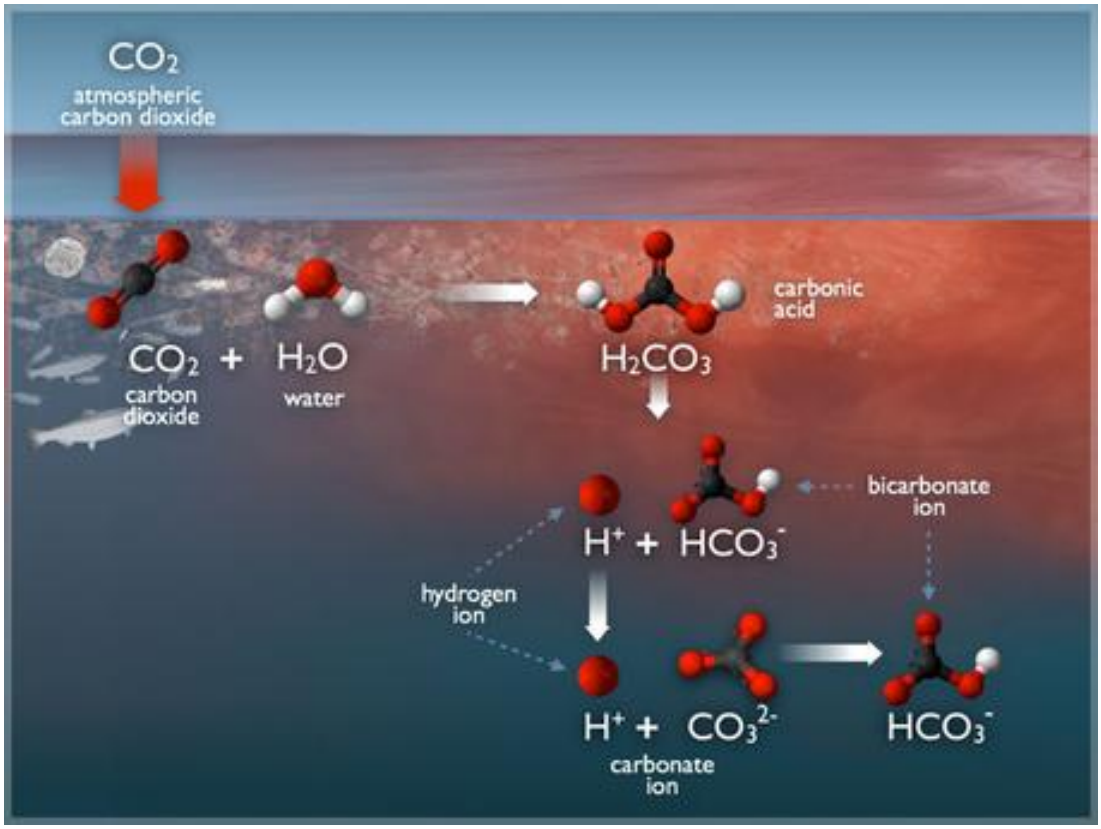

Figure I.2: Diagram of the simplified thermodynamics of the CO_2-carbonate system. Adapted from https://www.pmel.noaa.gov/

smaller than the aqueous form. These both forms are chemically not separable, and is usually denoted by CO_2^* or just CO_2 (dissolved CO_2). As a weak acid, H_2CO_3 can dissociate in two steps that lead to the formation of two ionic species previously mentioned, bicarbonate and carbonate, which are connected through chemical equilibria. Bicarbonate is by far the dominant species (90%), followed by carbonate (10%) and finally CO_2^* (<1%). Total CO_2, hereinafter DIC, reflects the sum of the concentrations of CO_2^*, HCO_3^- and CO_3^{2-}, while total alkalinity is defined as the concentration of all the bases than can accept hydrogen ions (H^+), and is largely a function of salinity, at the surface, since HCO_3^- and CO_3^{2-} are major components of seawater.

The hydrogen ion concentration is typically described in terms of pH= -$\log_{10}[H^+]$. The seawater CO_2-carbonate system is also highly influenced by the formation and dissolution of $CaCO_3$ (mostly in the form of calcite or aragonite) minerals used by marine animals and plants. The saturation (Ω) state of seawater with respect to $CaCO_3$ is proportional to the concentration of carbonate ions, as a consequence, the added anthropogenic CO_2 to the oceans, which in turn leads to a decrease in pH, decreases the saturation levels ($\Omega<1$) favoring the dissolution of solid calcium carbonate. Organisms that make shells (pteropods, foraminifera, cocolithphores) will have difficulty precipitating $CaCO_3$ and coastal corals may have difficulty growing and may eventually dissolve. There is an effective partial pressure of carbon dioxide, pCO_2 (μatm) in seawater: the partial pressure that the gas would have in the overlying atmosphere if an equilibrium is reached with the concentration of dissolved carbon dioxide, $[CO_2^*]$, in surface water. The ratio between $[CO_2^*]$ and the effective partial pressure, pCO_2, is described by the solubility, K_0 (mol kg^{-1} atm^{-1}), which reflects the relative efficiency with which molecules pass into and out of the water (Williams e Follows, 2011), and varies with environmental factors, including temperature and salinity (Weiss, 1974).The CO_2 exchange between the ocean and the atmosphere basically occurs within the mixed layer depth, which has, approximately, the same amount of carbon than the atmosphere, however, the net transfer occurs at the air-sea interface.

Chapter II

Hypothesis

The global warming-induced increase in the coastal portion of the Trade Winds should lead to an intensified upwelling circulation, larger nutrient supply within the euphotic zone and, consequently, enhanced primary production, which would probably be proportional to the magnitude of the wind intensification. This enhancement of primary production rates would likely reduce the rate of build-up of CO_2 in the atmosphere, probably leading the highly productive zone of the NHCS to a smoothed trend towards a CO_2 sink nature due to larger carbon assimilation.

In regard to the parameters that control seawater pCO_2, temperature and DIC are expected to be the most important drivers, particularly within the nearshore band, where high rates of DIC-rich and colder waters are upwelled yearlong stimulating the biological production. Thus, either physical (circulation) and biogeochemical (biological activity) processes may be the most important mechanisms behind the spatiotemporal variability of seawater pCO_2 and associated CO_2 fluxes. Furthermore, it is hypothesized that the cold phase of ENSO, La Niña, largely contributes to the atmospheric CO_2 accumulation.

Chapter III

Objectives

To explain the permanently observed CO_2 source nature of the most productive region of the NHCS and assess the role played by ENSO on modulating the oceanic carbon emittance. Moreover, the impact of the accumulation of atmospheric CO_2 on primary production rates is investigated.

Specific

- Quantify the magnitude of the strengthening of the upwelling-favorable winds during a decade (1999-2009) using a recent satellite-derived product.
- Analyze the changes in each production term, i.e. the growth rate and the nutrient limitation factor, of modeled primary production to evaluate the biological response to the upwelling intensification.
- Reproduce the observed climatological seawater pCO_2.
- Assess the relative importance between the drivers (DIC, temperature, alkalinity and freshwater) and mechanisms (air-sea CO_2 exchange, CO_2 solubility,

biological production, and circulation) behind the spatio-temporal variability of pCO_2.

- By means a combined statistical-modeled-observed approach, reconstruct the interannual air-sea CO_2 fluxes in order to assess the influence of ENSO.
- Calculate the oceanic emission/absorption rates of CO_2 and estimate how much carbon is released/retained in a climatological sense and during an average ENSO episode.

Chapter IV

Methodology

1 Domain of study

The domain of simulation spans the region between 70°W-100°W and from 4°N to 26°S encompassing the whole of the NHCS and the adjacent Eastern South Pacific (ESP), as seen in Fig. IV.1

1.1 Subdomain of analysis of the wind intensification

For the analysis of the wind intensification a 200 km-wide nearshore band along a nearly straight Peruvian coastline (orientation slope of about 120 degrees) from 6°S to 15°S, was selected. The latitudinal distributions spans from 5°S to 17°S over the 300 km-wide nearshore band (nearshore domain).

1.2 Subdomain of the sensitivity analyses of $p\mathrm{CO}_2$

For the sensitivity analyses of $p\mathrm{CO}_2$ and associated CO_2 fluxes, other two subdomains were considered i) the NHCS region as a whole, ranging from 0°-20°S and from 70°W-

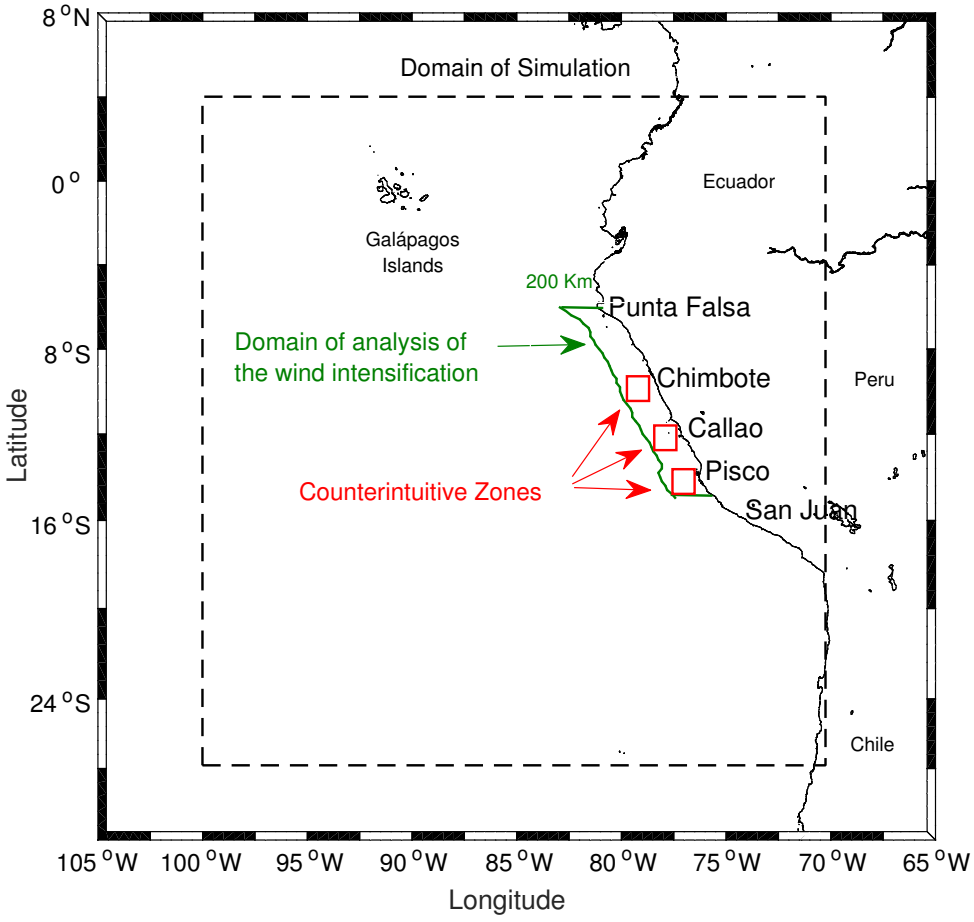

Figure IV.1: Domain of simulation (black dashed line). The domain of analysis related with the wind intensification is shown as a green area within the first 200 km nearshore. Red squares depict the counterintuitive zones.

90°W (regional domain), and ii) the highly productive upwelling region within the 300 km nearshore band and from 5°S-17°S (nearshore domain). The limits of the regional domain were chosen following 3 criteria, namely, (i) to be away from the model boundaries, (ii) to span the most productive region of the Peruvian biogeochemical province (Pennington et al., 2006) and (iii) to minimize uncertainties in the sensitivity analysis by choosing a large scale domain.

1.3 Subdomain of the inferred interannual CO_2 fluxes

The subdomain of analysis used for the inferred interannual CO_2 variability spans the region between 70-92°W and from 2°N to 22°S. In this case, the upwelling region (coastal + equatorial) is defined as the 50 km nearshore strip, from 17°S to 5°S, encompassing the adjacent ETP domain along an equatorial band of ∼300 km wide.

2 Hydrodynamical and biogeochemical model

The Hydrodynamical model is the Regional Oceanic Modeling System (ROMS-AGRIF). ROMS is a split-explicit, free surface oceanic model that solves the primitive equations, based on the Boussinesq approximation and hydrostatic vertical momentum balance. ROMS is vertically discretized in sigma coordinates or terrain-following curvilinear coordinates. The reader is referred to Shchepetkin e McWilliams (2005, 2009) for a more complete description of the physical model. In this study, we used the Pelagic Interaction Scheme for Carbon and Ecosystem Studies (PISCES V.1) biogeochemical model (see Fig. IV.2). PISCES simulates the marine biological productivity, carbon and main nutrients cycling such as nitrate, phosphate, silicate and iron. The reader is referred to Aumont et al. (2003); Aumont e Bopp (2006) for more detailed information about the model. The carbonate chemistry of PISCES follows the protocols of the Ocean Carbon-Cycle Model Intercomparison Project (OCMIP) (more information at `http://ocmip5.ipsl.jussieu.fr/OCMIP/`). The parametrization of the biogeochemical model follows Echevin et al. (2014a) (see also Fig. 1 in the appendix).

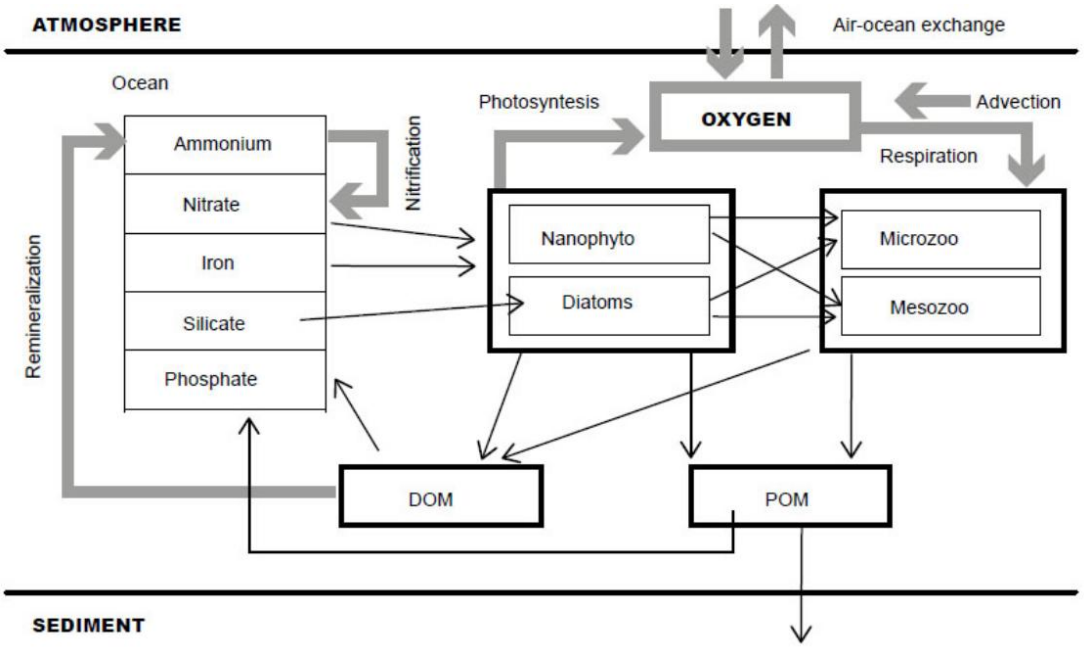

Figure IV.2: PISCES model architecture, omitting the carbonate system. Gray arrows indicate the processes that influence the concentration of oxygen. Adapted from Espinoza-Morriberon et al. (2016).

3 Spatial resolution and bathymetry

The horizontal resolution is $1/12^\circ$ (~ 9 km) with 30 vertical sigma levels refined toward the surface, i.e. the upper 300 m contain 18 sigma levels. The topography is derived from the General Bathymetric Chart of the Oceans (GEBCO_2014 Grid, version 20150318, (`www.gebco.net`), which has a grid spacing of 30 arc sec (Weatherall et al., 2015). It was smoothed in order to reduce pressure gradient computation errors (Marchesiello et al., 2003).

4 Boundary conditions

4.1 Physical forcings

ROMS was forced at the boundaries with a monthly climatology constructed for the period 1999-2009 from an eddy-permitting global ocean reanalysis, namely the Centro Euro-Mediterrano sui Cambiamenti Climatici (CMCC) Global Ocean Reanalysis System (C-GLORS V.4) (Storto et al., 2015). At the surface, ROMS is forced with net shortwave radiation extracted from the Japanese Ocean Flux Data Sets with Use of Remote Sensing Observations (j-OFURO V.3) (Kubota et al., 2002) (obtained from http://dtsv.scc.u-tokai.ac.jp/j-ofuro/) as a monthly climatology at $1/4^{\circ}$ resolution computed from 2002-2007. A monthly climatology of the net heat fluxes, computed from 1999 to 2009, was extracted from the European Centre for Medium-Range Weather Forecasts (ECMWF) Ocean Analysis System ORA-S3 (Balmaseda et al., 2008). In order to better reproduce the sea surface temperature (SST) seasonal cycle we adjusted the maximum and minimum values of ECMWF fluxes to that of Modern Era Retrospective-Analysis for Research and Applications (MERRA2) (Bosilovich et al., 2015) during the cold phase of the climatological year. In addition, we used a more modern and higher resolution satellite-derived products to compute the dQdSST nudging term (i.e. the kinematic surface net heat sensitivity to the sea surface temperature), where the air temperature, specific humidity, and wind speed forcings were extracted from the j-OFURO database. The evaporation and precipitation monthly climatology rates come from the Woods Hole Oceanographic Institute's objectively analyzed air-sea heat fluxes (WHOI OAFlux V.3) available at http://oaflux.whoi.edu, and from the Tropical Rainfall Measuring Mission (TRMM_TMI V.3) available at http://www.remss.com/missions/tmi at

1° and 1/4° horizontal resolution, respectively, both computed from 1998 to 2006. The monthly wind stress climatology comes from the NASA's Quik Scatterometer (QuickSCAT) (Liu et al., 1998; Risien e Chelton, 2008) for the period 1999-2009.

4.2 Biogeochemical forcings

Nutrients (nitrate, phosphate, silicate) and oxygen were extracted from the World Ocean Atlas (WOA 2013 V.2) (Garcia et al., 2014) for the upper ocean and from a global model output (NEMO-PISCES) for the ocean interior (Aumont et al., 2003). Dissolved organic carbon and iron come from the latter. The surface forcing for PISCES includes atmospheric iron dust input following Tegen e Fung (1995). Alk and DIC were obtained from the Global Ocean Data Analysis Project (GLODAP v2.2016b) (Olsen et al., 2016; Lauvset et al., 2016).

5 Numerical experiments and computation

5.1 Strengthening of the upwelling-favorable winds

In order to mimic Bakun's hypothesis by comparing the climatological wind forcing with a future scenario of strengthened winds that would be induced by global warming, we estimate the magnitude of the strengthening of the upwelling-favorable Trade Winds in the NHCS during a decade (1999-2009). To this end, we used the Cross Calibrated Multi Platform (CCMP V.2) (Wentz et al., 2015), from 1999 to 2009 (same period for the boundary conditions and QuickSCAT climatologies). CCMP combines the remote sensing data with in-situ measurements to produce a consistent gap-free, long-term ocean surface wind product. Least-squares fitted linear trend will

be applied to the filtered monthly wind data (moving average seasonal low pass filter). The analysis was performed over a 200 km-wide nearshore band along a nearly straight Peruvian coastline (orientation slope of about 120 degrees) from 6°S to 15°S.

5.2 Production terms

Primary Production (PP) is limited by the amount of Photosynthetically Active Radiation (PAR), nutrient concentration, temperature, chlorophyll-to-carbon ratio and phytoplankton biomass in the following manner:

$$\mathrm{PP} = \mathrm{Phytoplankton} \times \left[\mu_{\mathrm{eppley}} \left(1 - e^{-\frac{\alpha \, (\frac{Chl}{C}) \, \mathrm{PAR}}{\mu_{\mathrm{eppley}} \, \mathrm{NL}}} \right) \right] \times \mathrm{NL} \qquad \text{(IV.1)}$$

The first factor that affects the variability of PP is the Nutrient Limitation (NL) term ($0 \leq$NL≤ 1), which is a non-dimensional factor parameterized using the Michaelis-Menten relation. The lower NL, the more limited by nutrients phytoplankton growth is. In PISCES, phytoplankton is modeled by two compartments using the size of the cells as a criterion. The main difference between them is the dependence on silicate by diatoms. Thus, NL is the minimum among all the limitation terms computed for all nutrients. The second factor is the specific Growth Rate (GR) (in day^{-1}), which is a term that gives the combined influence of the physics on phytoplankton growth (the term in brackets in Eq.1). μ_{eppley} is the temperature-dependent maximum growth rate (in day^{-1}). The term in parenthesis is a nondimensional factor which gives the combined influence of light (PAR) as well as the chlorophyll-to-carbon ratio, where α is the initial slope of the Phytoplankton-Irradiance curve. Pennington et al. (2006) defined the boundaries of the Peruvian biogeochemical province as a coastal zone whose width is, approximately, of 250 km ranging from 4°S to 15°S.

We estimated the annual mean phytoplankton abundance between the simulated diatoms and nanophytoplankton concentrations within these latitudes over the 200 km-wide nearshore area (extent of the productive zone). The large phytoplankton cells, i.e. diatoms, represent almost 70% of the total phytoplankton community in our simulations. This group is known to be dominant nearshore in Peruvian waters (Iriarte e González, 2004). This finding serves to weight the vertically-averaged variables involved in the analyses (e.g., the limitations terms), related with both diatoms and nanophytoplankton. This is done in order to represent both phytoplankton types as an averaged response of the phytoplankton community in the coastal area.

The analyses (latitudinal distributions) were performed over the 300 km-wide nearshore band from 5°S to 17°S. This latitudinal range was chosen following three criteria, namely, (i) to be away from the model boundaries, (ii) to focus on the most productive region of the Peruvian biogeochemical province and (ii) to consider only the latitudinal band in which the temporal quantitative analysis of the strengthening of the winds was performed (section 5.1). The annual mean PP was vertically integrated within the euphotic zone (ZEU), which is defined as the downward light penetration depth of 1% of the surface value of PAR. PP is the total sum of the production associated to nanophytoplankton and diatoms. The NL and GR factors were both averaged in relation to their weights of phytoplankton abundance and vertically averaged within the ZEU.

5.3 Eddy-fluxes of Nutrients

In order to quantify the eddy-driven leaking of the coastal inventory of nutrients, we performed a Reynold's decomposition of the horizontal advection term, where the

flux is decomposed into a mean and a time-varying (eddy) induced flux, following the methodology of Gruber et al. (2011). The eddy-induced horizontal flux is $\overline{u' \cdot \mathrm{TIN}'}$, where TIN′ is the time-varying Total Inorganic Nitrogen (in mmol N m^{-3}) and u' is the time-varying cross-shore component of the velocity (in m s^{-1}). Both anomalies were calculated relative to the annual mean. Only TIN (the sum of nitrate and ammonium) was considered in this analysis because the nitrogen pool undergoes nitrogen fixation and denitrification. In contrast, phosphate is nitrogen-dependent, i.e. constrained by a constant Redfield ratio. Since we are interested in quantifying the horizontal eddy advection of positive anomalies of TIN, we discarded the analysis of the negative ones. This procedure allows to associate positive values of horizontal eddy fluxes with an onshore advection (positive u') of positive anomalies of TIN, and negative values with an offshore advection (negative u') of positive anomalies of TIN. In other words, we do not include the effect of an onshore flow of negative anomalies of TIN which would result in a negative horizontal eddy flux. A more detailed inspection shows that this effect is much smaller than the offshore advection of positive TIN anomalies and its removal does not change our conclusions.

5.4 Eddy kinetic energy

The Eddy Kinetic Energy (EKE), which is a measurement of the mesoscale eddy activity, was derived from surface geostrophic currents computed from sea level anomalies from AVISO (1999-2009) (http://www.aviso.altimetry.fr/duacs/). The satellite-derived EKE was horizontally averaged within the 300 km-wide nearshore band.

5.5 Residence Time

We computed the theoretical Residence Time (hereafter RT) as the product of the layer depth scale and the habitat width, divided by the offshore volume transport. Here, the layer depth scale is given by the latitude-dependant surface Ekman layer depth (δ_{Ekman}) using a coastal domain-averaged eddy viscosity (parameterized as function of the wind speed). The habitat width is determined by the first baroclinic Rossby radius of deformation (λ_{Rossby}) extracted from Chelton et al. (1998), and the offshore volume transport is estimated by the wind-driven cross-shore Ekman transport (M_{cs}). Hence, RT is the time required to entirely replace the volume of the upwelled water which travels a distance of one Rossby radius of deformation offshore.

$$RT = \frac{\lambda_{\text{Rossby}} \times \delta_{\text{Ekman}}}{M_{cs}} \tag{IV.2}$$

where

$$\delta_{\text{Ekman}} = \left(\frac{2\times 0.0013\times(w^2)}{|f|}\right)^{0.5}; w = \text{wind speed}$$

$$M_{cs} = \frac{[\tau_x \cos\theta + \tau_y \sin\theta]}{\rho f};\ \theta \approx 60°; \rho = 1024.5\,\text{kg m}^{-3}$$

5.6 Lagrangian experiment

The Lagrangian experiment (module 'FLOATS' from ROMS-AGRIF) consisted in the deployment of 4 clusters of floats at four fixed locations along the Peruvian coast within the domain of analysis. Each cluster is composed of nine drifters (equally arranged around each latitudinal location) and were released at 55 m depth (average

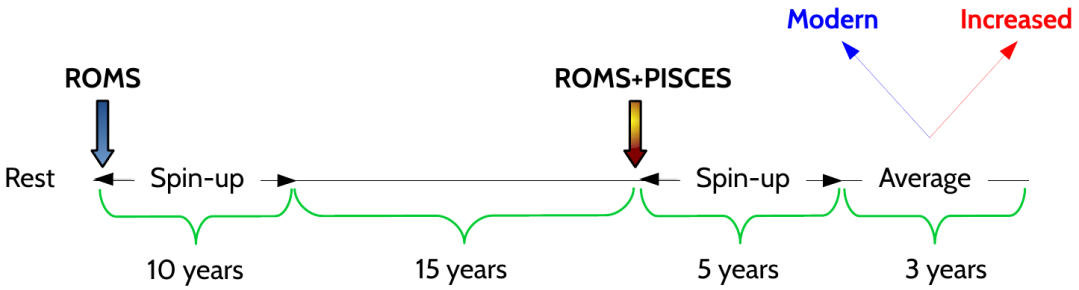

Figure IV.3: Timeline of the model setup of the HR simulation.

depth of the coastal upwelling) within the productive coastal area during August (stronger winds during austral Winter). They were all released simultaneously at the beginning of the month and their position was recorded at 12-hour intervals.

5.7 Model setup of the high-resolution simulation

As shown in Fig. IV.3, a climatological simulation was run for 25 years starting from rest only with the hydrodynamical model. Statistical equilibrium is reached after 10 years of model run (not shown). We kept the physical state of the end of year 25 to use it as the initial conditions in which PISCES was coupled, starting with the biogeochemical climatological conditions of January. ROMS/PISCES was run for eight years in total, of which after a spin-up of five years the biogeochemical tracers reach a nearly repeating annual cycle. We refer to "modern winds"experiment as the model solution which is an average of the last 3 years of simulation (from years 6 to 8). This is done in order to remove the model internal interannual variability. We also refer this solution as the high resolution (HR) control simulation. In contrast, we refer to "increased winds"experiment as the model solution which is an average of the last 3 years of simulation, but this time ROMS/PISCES was run with a perturbed wind product during those 8 years of simulation.

5.8 Simulated air-sea CO_2 fluxes

The CO_2 flux ($\mathrm{F}_{\mathrm{CO}_2}$) across these two mediums depends on the CO_2 transfer (k_w) velocity that measures the combined effect of various physical processes, including molecular diffusion, turbulent mixing, surface waves, bubbles and spray on the exchange across the air-sea interface (Jähne e Haußecker, 1998). k_w is proportional to the square of the wind speed. $\mathrm{F}_{\mathrm{CO}_2}$ is also dependent on the concentration of dissolved carbon in the surface ocean related to the atmosphere, i.e. on CO_2 solubility and the difference in pCO_2 between the air and sea, as follows:

$$\mathrm{F}_{\mathrm{CO}_2} = K_0 \cdot k_w \cdot (p\mathrm{CO}_2^{\mathrm{sea}} - p\mathrm{CO}_2^{\mathrm{air}}) \tag{IV.3}$$

where the atmospheric pCO_2, or $p\mathrm{CO}_2^{\mathrm{air}}$, is fixed at a modern value of 397 μatm (referenced to year 2015), estimated from the GLOBALVIEW-CO2 (2013) data product. $p\mathrm{CO}_2^{\mathrm{air}}$ is considered stationary because it is uniform over the NHCS and oscillates seasonally with an amplitude of, approximately, 2 μatm around the mean value. K_0 is the CO_2 solubility constant, computed using the formulation of Weiss (1974), which depends on temperature and salinity. k_w is the CO_2 transfer (piston) velocity following the formulation of Wanninkhof (1992). $p\mathrm{CO}_2^{\mathrm{sea}}$ is the partial pressure of the surface ocean CO_2. The convention is that positive values of $\mathrm{F}_{\mathrm{CO}_2}$ denote an outgassing of CO_2, i.e. from the ocean to the atmosphere, while negative values indicate an uptake by the surface ocean, i.e. from the atmosphere to the ocean. Since K_0 and k_w are positive quantities, the sign of $\mathrm{F}_{\mathrm{CO}_2}$ will be determined by the difference between the partial pressure of CO_2 in seawater and air ($p\mathrm{CO}_2^{\mathrm{sea}} - p\mathrm{CO}_2^{\mathrm{air}}$). As a consequence, in this work regions where $p\mathrm{CO}_2^{\mathrm{sea}} > 397$ μatm will act as a source, and regions where $p\mathrm{CO}_2^{\mathrm{sea}} < 397$ μatm will be a sink of atmospheric CO_2. Hereinafter we use seawater

pCO_2 when referring to pCO_2^{sea}.

5.9 Sensitivity of pCO_2 to drivers

Seawater pCO_2 is function of the concentration of DIC, Alk, T, and salinity, neglecting the very small contribution from variations in nutrients (Sarmiento e Gruber, 2006). In order to quantify the role of these drivers in causing pCO_2 variations, we decompose seawater pCO_2 into four components by using a first-order Taylor expansion (higher-order terms are neglected), following the approach of Lovenduski et al. (2007); Doney et al. (2009); Turi et al. (2014) and Arruda et al. (2015), using a modified decomposition, as follows:

$$\begin{aligned}\Delta pCO_2 \approx \frac{\partial pCO_2}{\partial DIC^s} \cdot \Delta DIC^s + \frac{\partial pCO_2}{\partial Alk^s} \cdot \Delta Alk^s \\ + \frac{\partial pCO_2}{\partial T} \cdot \Delta T + \frac{\partial pCO_2}{\partial FW} \cdot \Delta FW\end{aligned} \tag{IV.4}$$

where DIC^s and Alk^s are the salinity-normalized concentrations of DIC and Alk. This is done in order to remove variations due to the addition or removal of freshwater by precipitation and evaporation. ΔX's are the anomalies, with X representing DIC, Alk and T. These anomalies are either spatial or temporal, relative to a domain or an annual mean, respectively. The partial derivatives $\frac{\partial pCO_2}{\partial X}$ were determined by adding a small perturbation to each driver and recalculating pCO_2 using routines of an offline carbonate chemistry tool based on the OCMIP protocols (CO2SYS program (Van Heuven et al., 2011)). These perturbations are the 0.1% of the domain mean value of DIC, Alk and T. The freshwater (FW) contribution was estimated as a linear combination between changes in DIC and Alk with changes in salinity (see Appendix

A in Lovenduski et al. (2007)).

Table IV.1: Sensitivity experiments used to determine the contributions of air–sea CO_2 flux, biological production, CO_2 solubility and circulation to total pCO_2 from the LR control simulation. Based on Turi et al. (2014)

Simulation	Properties
CTRL	LR control simulation
S1	No air-sea CO_2 flux
S2	No air-sea CO_2 flux, no biology
S3	No air-sea CO_2 flux, no biology, constant CO_2 solubility

Table IV.2: Calculations between the sensitivity experiments used to determine the individual contribution of each mechanism to total pCO_2 from the LR control simulation. Based on Turi et al. (2014)

Calculation	Implication
CTRL-S1	Contribution of air-sea CO_2 flux to total pCO_2
S1-S2	Contribution of biology to total pCO_2
S2-S3	Contribution of CO_2 solubility to total pCO_2
S3	Pure circulation: pCO_2 if only circulation existed

5.10 Sensitivity of pCO_2 to mechanisms

In order to identify the main physical and biogeochemical mechanisms responsible for the spatiotemporal variability of seawater pCO_2, a series of additional sensitivity experiments were performed (see Tables IV.1 and IV.2). For consistency, we consider the same four mechanisms from Turi et al. (2014) and Arruda et al. (2015) that affect pCO_2 variability: i) air-sea CO_2 flux, which is due to the gas exchange at the air-sea interface; ii) CO_2 solubility, which is mainly driven by temperature variations due to the seasonal cycle of warming and cooling; iii) biology, which includes the net effect of the formation of organic matter and $CaCO_3$ and their remineralization and dissolution; and iv) circulation, which is attributed to the physical transport and

mixing of DIC and Alk from the boundaries into the interior of the domain and then to the surface, thus impacting pCO_2.

The methodology consists in progressively excluding each mechanism (see Eq. IV.5), as follows:

$$\underbrace{pCO_2^{\text{Control}}}_{\text{CTRL}} = \underbrace{pCO_2^{\text{Gas ex.}}}_{\text{CTRL-S1}} + \underbrace{pCO_2^{\text{Biology}}}_{\text{S1-S2}} + \underbrace{pCO_2^{\text{Solubility}}}_{\text{S2-S3}} + \underbrace{pCO_2^{\text{Circulation}}}_{\text{S3}} \tag{IV.5}$$

1) We first set the gas transfer velocity in the model to zero, thereby inhibiting any CO_2 exchange at the surface. We referred to this first sensitivity experiment simulation as S1. The difference in pCO_2 between the control simulation and S1,(pCO_2^{ctrl}-pCO_2^{S1}), is thus the impact of the air-sea CO_2 fluxes on seawater pCO_2.

2) In the second experiment (S2) we started from S1, but additionally set the net shortwave radiation as zero and, consequently, the PAR is zero. By doing so, we eliminate phytoplankton growth and, consequently, biological production of organic carbon in our solution. This radiative forcing is used exclusively for the biology and it does not affect the net heat fluxes computation. The difference in pCO_2 between S1 and S2, (pCO_2^{S1} - pCO_2^{S2}), is the contribution of biology on seawater pCO_2.

3) In the third experiment (S3) the impact of the solubility was eliminated by keeping a constant domain-averaged temperature and salinity value. The difference in pCO_2 between S2 and S3 (pCO_2^{S2} - pCO_2^{S3}) represents the impact of the variable CO_2 solubility to total seawater pCO_2, i.e. the impact of SST and salinity on pCO_2.

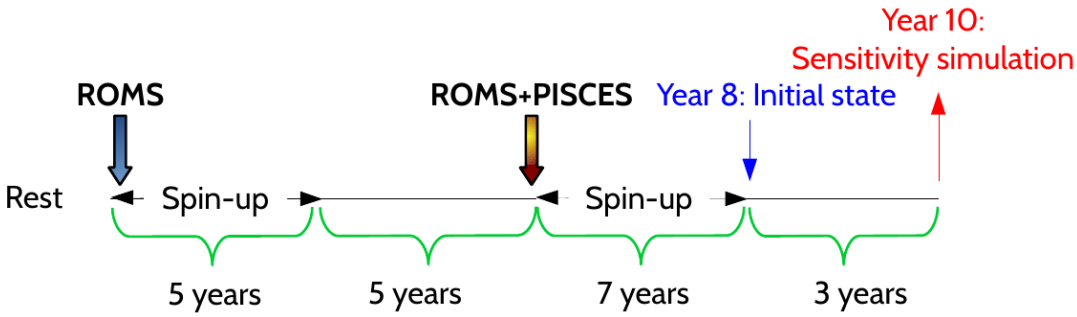

Figure IV.4: Timeline of the model setup of the LR simulation.

4) Finally, since in S3 the contribution of gas exchange, biology, and CO_2 solubility were eliminated, the only mechanism impacting the pCO_2 is the circulation, which will transport and mix DIC and Alk in the entire domain. Thus, S3 itself represents a solution where pCO_2 is affected only by the circulation.

5.11 Model setup of the low-resolution simulation

Due to computer limitations, we performed a coarser control simulation at $1/6^{\circ}$. As shown in Fig. IV.4, in this case ROMS started from rest and was ran for 15 years. Simulations were restart from here for 10 more years coupled with PISCES. We spun-up the model for 7 years and set the last year (tenth year) as the low resolution (LR) control simulation. All the sensitivity simulations began from the same physical-biogeochemical state (year 8). For consistency, the analyses were made for the tenth year of each sensitivity experiment.

6 Interannual CO_2 efflux variability

6.1 Coupled physical-biogeochemical hindcast

The outputs from the Mercator-Ocean (Toulouse, FR) GLORYS2V4 global ocean reanalysis (Garric et al., 2017) (monthly-means at $1/4^\circ$ horizontal resolution covering the 1993-2015 period) are used. GLORYS2V4 is forced by ERA-Interim atmospheric variables (produced at ECMWF) (Dee et al., 2011) with data assimilation of temperature and salinity profiles as well as sea level anomalies, sea ice concentration, sea surface temperature, and mixed layer depth. The simulation was forced with temperature and salinity based on EN4 (Good et al., 2013) replacing the Levitus Climatology. For a more detailed description of the ocean model, the data assimilation method, the assimilated observations, and the validation, the reader is referred to http://marine.copernicus.eu/documents/QUID/CMEMS-GLO-QUID-001-025.pdf (last accessed 10 February 2019). The biogeochemical model is PISCES v2 (Aumont et al., 2015). The experiment is a biogeochemical hindcast for the global ocean that provides 3D biogeochemical fields for the period 1993-2017 at $1/4^\circ$ horizontal resolution, and the physical forcings come from GLORYS2V4 (non-assimilated). Monthly atmospheric pCO_2 (global value) was prescribed at the air-sea interface. The simulation starts at rest (cold start) in December 1991 and is initialized with World Ocean Atlas 2013 for nitrate, phosphate, oxygen and silicate (Garcia et al., 2013, 2014). Similarly, it is initialized with GLODAPv2 climatology for Dissolved Inorganic Carbon (DIC) and Alkalinity (Key et al., 2015), and with model fields from a climatological run for dissolved iron and dissolved organic carbon. The first two years of simulations are considered as a spin-up phase. A comprehensive assessment of the quality of the global biogeochemical hindcast simulation may be found at http://cmems-resources.cls.

fr/documents/QUID/CMEMS-GLO-QUID-001-029.pdf (last accessed 10 February 2019).

6.2 Inferred CO_2-carbonate system variables

The CArbonate system and Nutrients concentration from hYdrological properties and Oxygen using a Neural-network (CANYON-B) (Bittig et al., 2018) was implemented, which is a re-develop approach of Sauzède et al. (2017). CANYON-B is a Bayesian neural network mapping that accurately reproduces GLODAPv2 bottle data and the biogeochemical relations contained therein. It thus provides mappings from one set of inputs variables (temperature, salinity, oxygen, pressure, location, and time) to another set of variables such as the four CO_2-carbonate system variables, which are alkalinity (Alk), dissolved inorganic carbon (DIC), pH, and pCO_2^{sw}. For a more detailed description of the method and a robust assessment of the validation, the reader is referred to (Bittig et al., 2018). CANYON-B is forced, for any grid point at the surface throughout the entire period of analysis, with sea surface temperature, sea surface salinity and sea surface oxygen concentrations from the model outputs of the coupled physical-biogeochemical hindcast.

6.3 Inferred air-sea CO_2 fluxes

Similar than Section 5.8. However, here we used the revisited formulation of Wanninkhof (2014), which is appropriated for regional estimates of CO_2 when using the Cross Calibrated Multi Platform (CCMP) V.2 (Wentz et al., 2015) wind product (monthly-means at $1/4^\circ$ horizontal resolution). 18-year monthly maps of atmospheric pCO_2 (pCO_2^{air}) were constructed with an artificial increase rate starting from

a global average atmospheric value of 365 μatm, corresponding to January 1998 (www.esrl.noaa.gov/gmd/ccgg/trends/). The increase rate of pCO_2^{air} was taken from the inferred pCO_2^{sw} linear trend for any grid point. This trend was calculated using Least Squares and ranges from -1 to +3 μatm year^{-1} (not shown), in agreement with Takahashi et al. (2003), who estimated a trend of 1.5 μatm year^{-1} along the Equatorial Pacific. From the experience, if a monthly-varying pCO_2^{air}, but fixed in space, is imposed, a moderate drift is obtained when calculating ΔpCO_2, or (pCO_2^{sw} - pCO_2^{air}). Thus, the procedure to construct pCO_2^{air} was applied mainly for two reasons: i) to avoid an abrupt negative slope in the trend of ΔpCO_2 due to the ocean's long-term response to the accumulation of anthropogenic CO_2 in the atmosphere, which may be interpreted as an increasing ocean carbon sink; ii) to maintain the regional spatiotemporal intrinsec variability since pCO_2^{sw} trends generally track pCO_2^{air} trends. This is supported by the fact that pCO_2^{sw} in the equatorial region has been increasing at a rate similar to the atmospheric CO_2 increase (Feely et al., 2006) because there is a chemical tendency to equilibrium between the atmosphere and ocean (Fay e McKinley, 2013).

6.4 Sensitivity of air-sea CO_2 flux anomalies

To diagnose the individual contributions of the forcing factors governing interannual physical-biogeochemical variability of $\mathrm{F_{CO_2}}$, a Reynold's decomposition (e.g. $\Delta pCO_2 = \overline{\Delta pCO_2} + \Delta pCO_2'$) was perfomed following the same methodology of Doney et al. (2009). Two forcing factors are considered, i.e. ($K_0 k_w$) and (ΔpCO_2) and the corresponding linear decomposition terms of the air-sea CO_2 flux anomalies are:

$$\begin{aligned} \mathrm{F'_{CO_2}} \approx\ & (K_0 k_w)' \times \overline{\Delta p\mathrm{CO_2}} \\ & + \overline{(K_0 k_w)} \times \Delta p\mathrm{CO_2}' \\ & + \left[(K_0 k_w)' \times \Delta p\mathrm{CO_2}' - \overline{(K_0 k_w)' \times \Delta p\mathrm{CO_2}'}\right] \end{aligned} \tag{IV.6}$$

The anomalies ($'$) are either spatial or temporal, relative to a domain or a monthly mean (overline bar), respectively. The first term in the right-hand side of Equation 2 reflects the contribution to the variability of the air-sea CO_2 flux from gas transfer and solubility anomalies. However, $(K_0 k_w)'$ basically reflects variations in wind speed. This is because the temperature dependence of both K_0 and k_w approximately cancel each other out (increased SST will reduce the solubility of CO_2 favoring the outgassing, but increased temperatures will decrease the transfer velocity and so reduce the fluxes). Hereinafter, this term is referred to as the gas transfer velocity-driven flux variability for short. The second term reflects the variability induced by $\Delta p\mathrm{CO_2}$ anomalies. $\Delta p\mathrm{CO_2'}$ is primarily driven by changes in $p\mathrm{CO_2^{sw}}$ in response to the variability of its drivers, i.e. SST, SSS, DIC, and Alk. The third cross-term reflects the contribution of CO_2 and gas transfer/solubility anomalies, corrected for its mean value.

6.5 ENSO criteria

The Coastal El Niño Index (ICEN) (Takahashi et al., 2014) is used, which is a 3-month running mean of sea surface temperature anomalies for the El Niño 1+2 region available at http://www.met.igp.gob.pe/variabclim/indices.html. Nine ENSO episodes were found, disregarding the events that last less than 3 months. The months while the ICEN index is larger than +1.7 and smaller than -1.4 are considered

in order to better represent El Niño and La Niña events, respectively. By doing so, only strong/extraordinary El Niño and strong La Niña events are taking into consideration for the composites. The monthly anomalies, for any variable, were constructed by removing the monthly mean climatology computed for the entire period of analysis (i.e. mean January, mean February, etc.) at each grid point. This work considers the average El Niño episode as the temporal mean of the monthly composite of the warm phase of ENSO. Similarly, the average La Niña episode is the temporal mean of the monthly composite of the cold phase of ENSO, for any variable. El Niño episode typically last 9-12 months, which rarely persist more than a year at a time. La Niña event could even last longer than El Niño. This is in part because the normal conditions, or "ENSO neutral conditions", in the NHCS resemble more with La Niña conditions than El Niño ones. Throughout the analysis period, the average El Niño episode lasts 10 months and the average La Niña episode lasts 14 months. Consequently, it is reasonable to consider an average ENSO phase duration of, approximately, 12 months.

Chapter V

Model skill assessment

This chapter is mainly intended for the comparison of the outputs of the simulations against available observations. This part focus in the sea surface temperature on seasonal time scales, surface chlorophyll-a and primary production on an annual mean basis. The circulation pattern and the net transport of the main currents in the NHCS is also evaluated. It is also showed the comparison between modeled and observed nitrate and oxygen vertical sections within the coastal domain in order to validate the tridimensional structure of the biogeochemical tracers on an annual mean basis. The databases used, as well as all the previous works in which we support our results, are referenced along this chapter.

1 Sea surface temperature

Fig. V.1 shows the comparison between the modeled SST with the satellite-derived SST from the Moderate-resolution Imaging Spectro radiometer (MODIS) at 4 km horizontal resolution (http://modis.gsfc.nasa.gov/) monthly averaged from January 2002 to December 2015. In general, simulated SST is colder than observations

at the nearshore band during all seasons. This cold bias could be attributed mainly to two factors, the excessive coastal upwelling by the hydrodynamical model and the too strong winds at the shore. The same large scale SST pattern is observed, with slight differences in magnitude along the equatorial band, where the equatorial upwelling is very well captured by the model. There is a patch of warm waters of 20°C during Spring and Summer around 20°S which is well reproduced. In all seasons we can notice the equatoward extended tongue that highlights the upwelling front due to the cold upwelled waters. A Taylor diagram shows the seasonal statistical comparison between the observed (MODIS is laid on x-axis at the normalized standard deviation of 1) and simulated SST. The correlation ranges between 0.8-0.9 with a maximum during Winter. The centered root-mean-square (RMS) difference between simulated and observed patterns is proportional to the distance to the point on the x-axis identified as **MODIS**. Simulated seasonal SST lays inside the centered normalized RMS error of 1, as evidenced by a red semicircle.

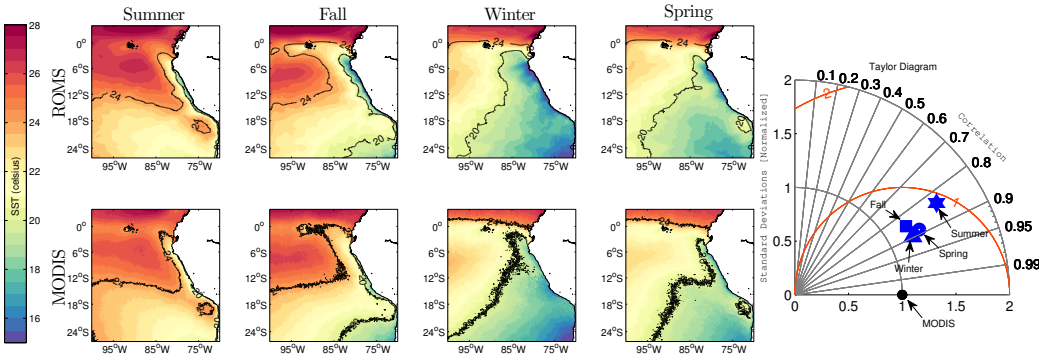

Figure V.1: Seasonal mean sea surface temperature [°C] from ROMS (upper row) and MODIS (bottom row). Black lines denote the isotherms of 20°C and 24°C. A Taylor diagram is also provided, in which the star is for Summer, square for Fall, triangle for Winter and circle for Spring.

2 Chlorophyll-a, surface velocities and primary production

The annual mean simulated surface chlorophyll−a concentration is compared with MODIS satellite observations (see Fig. V.2-a,b). This figure has been trimmed at 85°W to avoid the oligotrophic ocean and focus on the coastal region. High concentrations are located within the highly productive nearshore band (black isoline: >2 mg Chla m^{-3}), which is narrower in the simulations from 10°S to 15°S. However, the spatial pattern is very well captured by the model, exhibiting a similar latitudinal distribution with a strong seaward gradual decrease. Furthermore, MODIS appears to exhibit an overestimation of the surface chlorophyll during its first years, i.e. from 2002 to 2007, when compared with in-situ or satellite-derived observations from SeaWiFS (Dante Espinoza, personal communication, April, 2017). The annual mean surface velocity fields computed from ARGO from 2001-2015 (http://www.argo.ucsd.edu, http://argo.jcommops.org) have been superimposed as black arrows. A typical equatorward surface circulation pattern for an EBUS is obtained. The South Equatorial Current (SEC) is well represented at lower latitudes with westward velocities of 0.25 to 0.45 m s^{-1}. The Peruvian Coastal Current (PCC) with its oceanic branch are also observed, flowing westward in the central domain.

The satellite-derived primary production (PP), estimated using the Carbon-based Production Model (CbPM) (Westberry et al., 2008) (updated method) for MODIS (9km), was used (http://www.science.oregonstate.edu/ocean.productivity/). This method is the most suited due to its different approach to estimate productivity by retrievals particulate scattering coefficients to estimate phytoplankton carbon

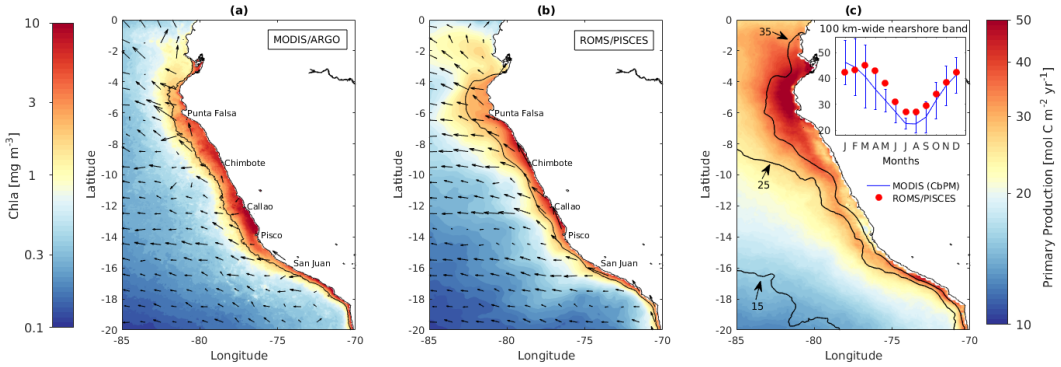

Figure V.2: (a) Annual mean sea surface chlorophyll-a concentration [mg m^{-3}] from MODIS. Arrows superimposed are the observed annual mean surface velocities extracted from ARGO. (b) Simulated annual mean sea surface chlorophyll-a concentration. The superimposed arrows denote the annual mean simulated velocities. Black continuous line depicts the highly productive coastal zone, defined as 2 mg Chla m^{-3} isoline. (c) Annual mean satellite-derived Primary Production (PP) [mol C m^{-2} yr^{-1}] from MODIS (CbPM Method). Black lines are contours of simulated PP (10, 25 and 35 mol C m^{-2} yr^{-1}). The inset shows the monthly climatology time series between both observed (blue line) and simulated (red circles) PP rates with their respective error bars.

concentration, thus replacing chlorophyll as a metric of biomass (Behrenfeld et al., 2005). PP is a function of Chlorophyll-to-carbon ratio, PAR and temperature. The monthly climatology was computed from 2003 to 2015. For comparison, we computed the annual mean primary production rates (vertically integrated within the euphotic zone), as shown in Fig. V.2-c. Simulated PP is shown as black contours of 15, 25 and 35 mol C m^{-2} yr^{-1}. There is a good agreement between simulated and satellite derived PP rates. The inset shows the domain-averaged monthly climatological time series computed within the 100-km wide nearshore band, in which the simulated PP is shown as red circles. The blue curve is for the observed PP with their respective error bars (twice the normalized standard deviation). Differences may be due to the high sensitivity of the calculation of PP rates to the variability of limiting growth

factors, such as temperature, light and nutrient availability (Behrenfeld e Falkowski, 1997). The annual mean PP, averaged between 6°S and 16°S over the 100-km wide nearshore band, was estimated by 42 mol C m^{-2} yr^{-1}. Over the same spatio-temporal domain, Messié et al. (2009) estimated the PP rates in to be about 47 mol C m^{-2} yr^{-1}, while the satellite-derived PP is about 33 mol C m^{-2} yr^{-1}. In addition, (Albert et al., 2010) found 37 mol C m^{-2} yr^{-1} using the same physical-biogeochemical model, although with slight different parameterization.

3 Circulation and transport

In order to validate the circulation pattern, we verify the hydrodynamical vertical structure. Fig. V.3-a shows the averaged cross-shore section of the annual mean alongshore velocity (cm s^{-1}) around Callao (12.1°S $\pm$0.2 degree). The coastal circulation is dominated by the PCC and by the Peru-Chile Countercurrent (PCUC). The inset in panel-a of Fig. V.3 shows the 6 transects chosen to perform the average with 8 stations each one. The virtual stations are separated by about 15 km along the transect. The velocity fields were rotated 121.5 degrees for Callao, thus, positive alongshore velocities are strictly equatorward and the negative ones are poleward. The PCUC flows poleward over the slope at 150 m depth dominating the first 100 km from the coast at the subsurface with a mean speed of, approximately, 10 cm s^{-1} in its core. The PCC acts as a equatoward coastal current jet with a maximum speed of, approximately, 20 cm s^{-1} nearshore, extending from the surface down to 50 m depth. The PCUC was found at 10°S (15°S) beneath 100 m (130 m) depth with speeds ranging between 6 to 7 cm s^{-1}. These values are consistent with observations (Brink et al., 1983; Huyer et al., 1991) and previous modelling works, such as Penven (2005); Colas

et al. (2008); Albert et al. (2010); Montes et al. (2010, 2011); Echevin et al. (2011); Mogollón e Calil (2017). The 3 most important eastward zonal currents entering in the domain are sucessfully reproduced. Fig. V.3-b shows a meridional vertical section, averaged between 86°W-87°W, of the annual mean of zonal currents (as a color map) and oxygen (as contours). It is noticiable the Equatorial Undercurrent (EUC), the Primary Southern Subsurface Countercurrents (pSSCC), and the Secondary Southern Subsurface Countercurrents (sSSCC) (or Tsuchiya jets). The EUC extends from 40 to 250 m depth and is located between $\pm$1.5°S with mean speed of, approximately, 20-25 cm s^{-1}. The pSSCC and sSSCC flow with velocities of about 10 and 5 cm s^{-1} around 3.5°S and 7°S, respectively.

Our results show oxygen-rich waters in the core of the pSSCC and the EUC. It is also noticeable the latitudinal distribution of the Oxygen Minimum Zone (OMZ) upper edge (defined as oxygen concentrations below 25 mmol m^{-3}), with a steep northward deepening. These eastward currents were identified by Montes et al. (2014) as important contributors to the oxygen balance in the domain, with the sSSCC bringing low oxygen concentrations, and the pSSCC, elevated ones, although not as high as EUC-associated waters. Fig. V.3-c shows the transport of three of the most important currents in the NHCS, such as the EUC, the PCC and the PCUC. The computation follows Echevin et al. (2011), which is: the PCC transport was computed by integrating the equatoward flow (averaged from 8°S to 13°S) within 150 km from the coast and from the surface to 100 m depth.The PCUC transport was computed by integrating the poleward flow (averaged from 8°S to 13°S) greater than 1 cm s^{-1} in the 20-300 m depth range, within the 0-200 km coastal band. The EUC transport was computed through a meridional averaged section between 86°W

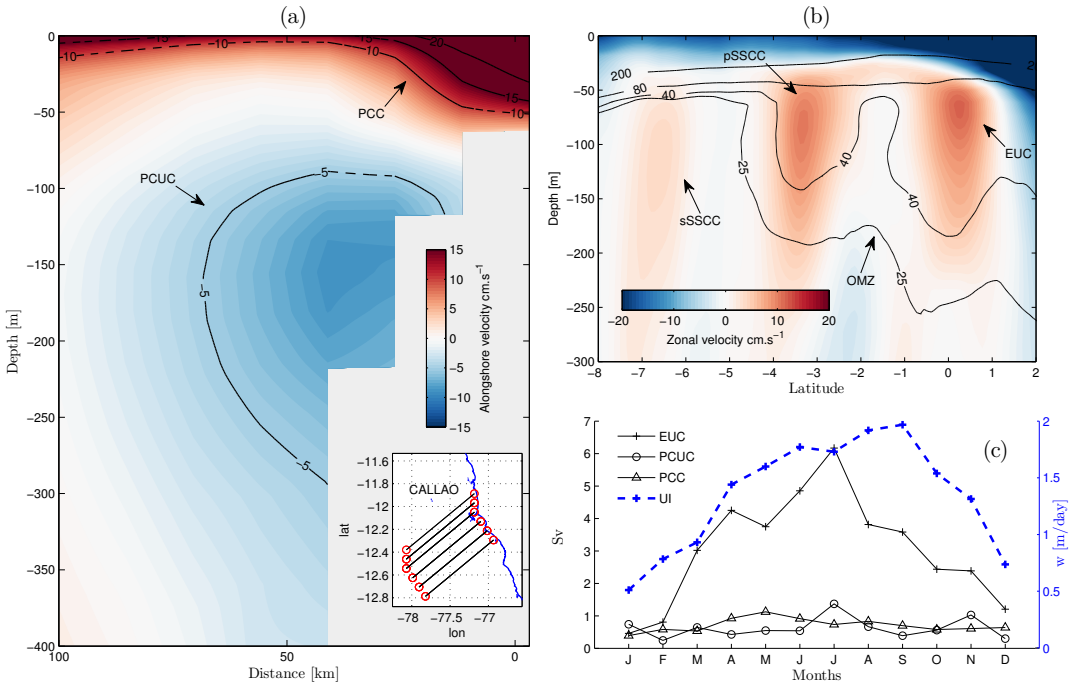

Figure V.3: (a) Cross-shore section of the annual mean alongshore velocity [cm s^{-1}] at Callao (12.1°S ±0.2 degree). (b) Meridional section of the annual mean zonal velocity [cm s^{-1}] averaged between 86°W-87°W. The contours are isolines of oxygen. (c) Monthly climatology of the transport [Sv] of the EUC, PCC and PCUC. The Upwelling Index: UI [m day^{-1}] is also shown.

and 87°W, between 2°N and 2°S in latitude and 300 m depth. A coastal upwelling Index (UI) was also computed by averaging vertical velocities at 50 m depth within a 100 km wide coastal band between 6°S and 15°S. This index acts as a proxy for the vertical transport. Overall, the mean PCC, PCUC and EUC transport is 0.7, 0.6 and 3 Sv, respectively. The PCC transport exhibits two maximum during Fall and Winter, which are highly correlated with UI (0.65). This is because the PCC is driven by the upwelling-favorable winds. Similarly, the EUC is also highly correlated with UI (0.85). Similar findings were obtained by Echevin et al. (2011) (Figs.4,5). Hence, our simulations are in good agreement with the observed circulation and with the mean

tridimensional dynamical structure of the NHCS.

4 Nitrate and oxygen

In order to evaluate the modeled biogeochemical tracers, two time-depth diagrams of the climatological oxygen and nitrate fields are shown in Fig. V.4. The observed tracers were extracted from the WOA 2013 database (Garcia et al., 2014). The observed Mixed Layer Depth (MLD) was extracted from a global climatology computed from profiles obtained from the National Oceanographic Data Center (NODC) and from the World Ocean Circulation Experiment (WOCE) database, gridded at a coarse resolution of 2×2 degree (Montégut et al., 2004). The optimal temperature criterion is found to be 0.2 °C absolute difference from the surface. The optimal one in density is 0.03 kg m^{-3} difference from the surface. The observed ZEU was extracted from a satellite-derived product using MODIS at 9 km resolution (Lee et al., 2007). This MODIS-derived monthly climatology was constructed from 2002 to 2016. All the quantities involved in these time-depth diagrams were averaged within the 100-300 km wide near-offshore band and from 5°S to 17°S. We choose this 200-km thickness to avoid some biases with regards to the coastline when interpolated to the model grid, as a result of using coarser observation databases.

A more detailed inspection of the climatological observed values of oxygen and nitrate fields at subsurface levels, reveals the paucity of the measurements, evidenced with large values of standard deviation (>10 mmol N m^{-3}), particularly during the last months of the year. This explains the supposed overestimation of nitrate below the MLD. The comparison on a monthly climatological basis though, reveals that

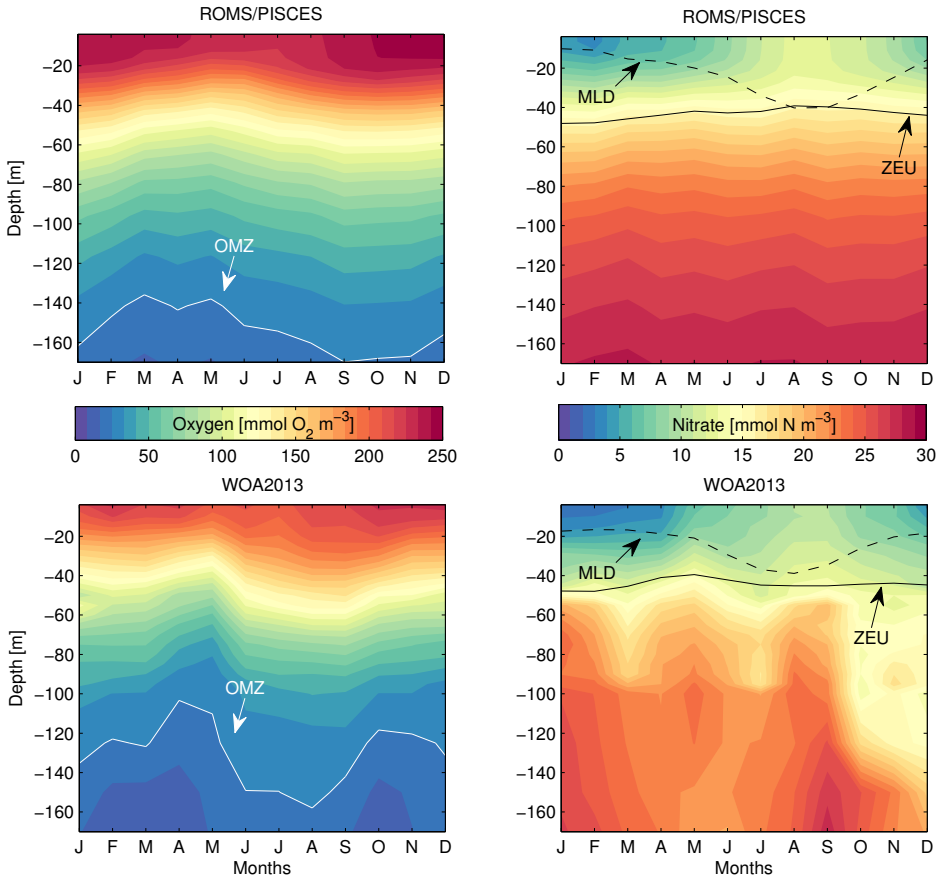

Figure V.4: Time-depth diagram of the climatological oxygen and nitrate fields (both in mmol m^{-3}). The observed tracers were extracted from the WOA 2013 database. White lines in the panels at the left column denote the Oxygen Minimum Zone (OMZ = 25 mmol O_2 m^{-3}). Black dashed line at the right column denotes the Mixed Layer Depth (MLD) and the continuous line, the depth of the euphotic zone (ZEU).

the nitrate and oxygen are well reproduced. The same is true for the climatological monthly time series of MLD and ZEU. The simulated MLD is 3.7 m shallower during the first half of the year and about 2 m deeper during the second half of the year, when compared with observations. The annual mean simulated ZEU is 43 m, while the observed is 44 m. High nitrate concentrations are reproduced below the

MLD, with minimum values at the surface. However, during Winter and early Spring, enhanced upwelling leads to elevated nutrients concentrations at the surface layer. The model reproduces the annual cycle of oxygen, with a relatively well oxygenated mixed layer. However, the modeled oxygen overestimated surface concentrations in about 5%. Another bias is found in subsurface levels, e.g. below 120 m depth, where the simulated OMZ is about 14% deeper than the observed one (150 m). Since these slight discrepances may be considering as details, we are convinced that our simulations are robusted enough in order to proceed with the sensitivity study.

5 DIC, Alk and SST from LR simulation

Fig. V.5 shows the comparison between simulated (low resolution control simulation) and observed annual mean dissolved inorganic carbon, total alkalinity, and sea surface temperature. DIC and Alk were extracted from the Global Ocean Data Analysis Project (GLODAP v2.2016b). SST was extracted from the Moderate-resolution Imaging Spectro radiometer (MODIS) and was monthly averaged from January 2002 to December 2015 at a 4 km horizontal resolution (http://modis.gsfc.nasa.gov/). Observations are shown as contours, and the simulated field, as a color map. However, a few contours are shown in each panel in order to not pollute the figures considering a similar annual mean spatial distribution. As shown, the nearshore latitudinal transition from south to north and from high to low concentrations of both DIC and Alk is very well reproduced. High levels of DIC are found in the coastal band, in agreement with the GLODAP database. However, the model seems to overestimate DIC in, approximately, 20 μmol C l^{-1}. This bias could be attributed to the fact that large areas of the ocean were undersampled and underrepresented in GLODAP, especially

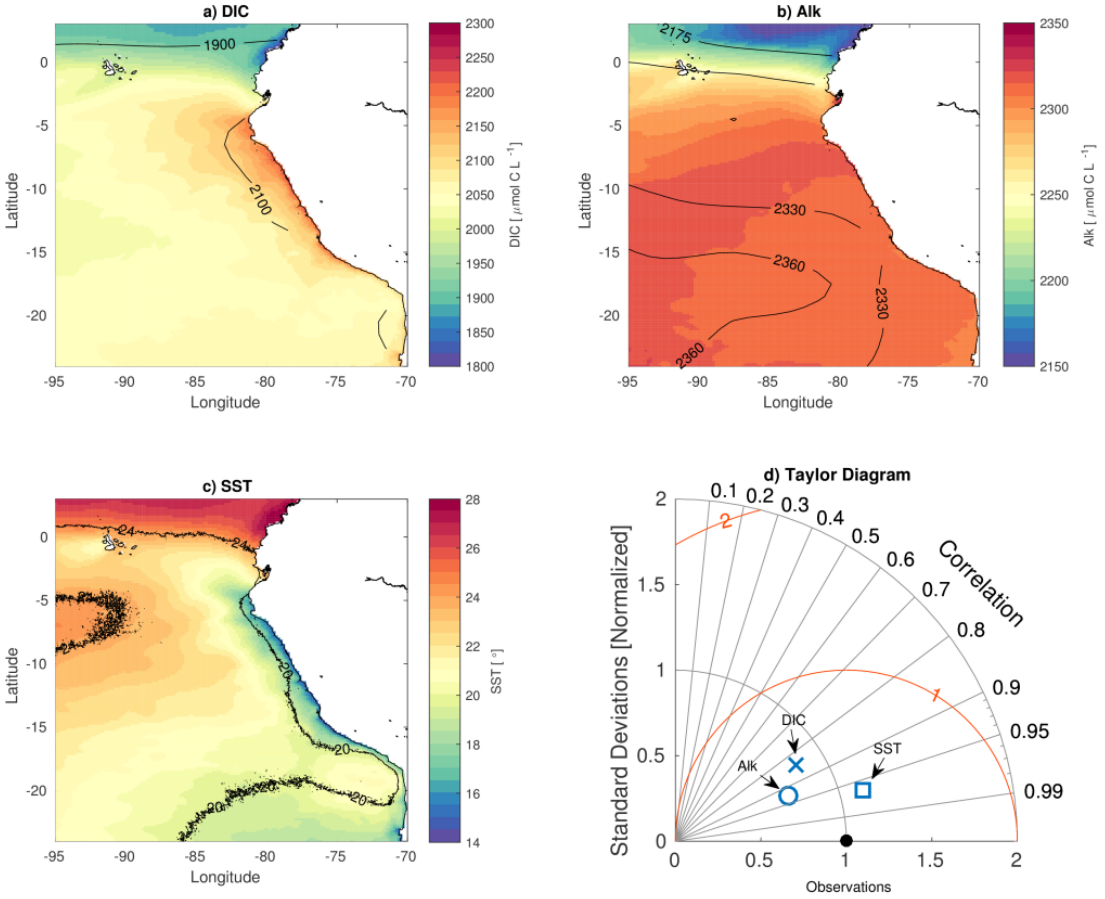

Figure V.5: Annual mean comparison between simulated and observed sea surface a) dissolved inorganic carbon [μmol C l^{-1}]; b) alkalinity [μmol C l^{-1}], and c) temperature [°C]. Observations are denoted as contours, and the respective simulated field, as a color map. d) The Taylor diagram provides a statistical comparison of the annual means.

in the Humboldt CS where a very limited number of observations is available. In addition, larger mapping errors (>30 μmol C l^{-1}) associated to the GLODAP database could explain the underestimation of surface DIC (17 μmol C l^{-1}) within the southern portion of the coastal domain, and the underestimation of surface alkalinity (23 μmol C l^{-1}) within the oceanic part of the domain. The Taylor diagram shows the statistical comparison of Alk and DIC (circle and cross, respectively), both with high positive

correlations around 0.9. On the other hand, we can notice the equatoward extended tongue that highlights the upwelling front in panel-c. Simulated SST is lower than the observations at the nearshore band (-2°C). Overall, the large scale pattern is capture by the simulation in an annual scale. The square in the Taylor diagram represents the SST.

6 Seawater pCO_2

6.1 Gridded in-situ databases

In order to evaluate the model skill in reproducing seawater pCO_2 we used a set of quantitative metrics comparing the model output with observational data. The statistical metrics are the correlation coefficient (r), the root mean squared error (RMSE), the reliability index (RI), the average error or bias (AE), the average absolute error (AAE), the modeling efficiency (MEF), the cost function (CF), and the percentage of bias (PB). The correlation coefficient measures the tendency of the simulated and observed values to vary together. Ideally, this value will be close to one. RMSE, AE, and AAE are all measures of the size of the discrepancies between modeled and observed values. Together these three statistics provide an indication of the model prediction accuracy. Values near zero indicate a close match. RI quantifies the average factor by which modeled values differ from observations. A good model prediction yields RI values close to one. MEF measures how well a model predicts a variable relative to the average of the observations. A value near one indicates a close match between observations and model predictions. For a more detailed explanation of these parameters, the reader is referred to Stow et al. (2009). CF is a measure of the "good-

ness of fit" of the model and data, and PB is the performance indicator (Dabrowski et al., 2014). If MEF is greater than 0.65, the prediction is excellent, for values in the range 0.5–0.65 the prediction is considered very good, for the range between 0.2–0.5 the prediction is good, and for values smaller than 0.2 the prediction is poor/bad. Similarly, PB evaluates the model as follows: <10 = excellent, 10–20 = very good, 20–40 = good, >40 = poor/bad (Maréchal, 2004). If CF <1 = excellent/very good, 1–2 = good, 2–3 = reasonable and >3 = poor/bad (Moll e Radach, 2003). The statistics were applied to the annual average of seawater pCO_2 within the limits of the domain of simulation due to the sparseness of available observations. In addition, the spatial standard deviation of the observations can be inferred dividing AAE by CF.

The databases used for the comparison are the Surface Ocean CO_2 Atlas database, SOCAT V.6 (Bakker et al., 2016) and the carbon dioxide research group of the Lamont-Doherty Earth Observatory (LDEO) of Columbia University (Takahashi et al., 2018). For consistency, we converted all the observed fugacity of CO_2 (fCO_2) from SOCAT (from 1970 to 2016) to pCO_2 using the CO2SYS program (Van Heuven et al., 2011) (fugacity is about 0.3 to 0.4 $\%$ lower than pCO_2 due to the non-ideality of the CO_2 gas (Weiss, 1974)). Since our climatological simulation is representative of a modern oceanic state, observed data were normalized to the year 2015 assuming an anual global mean seawater pCO_2 increase rate of 1.5 μatm yr^{-1} (Takahashi et al., 2009). The LDEO database consists of underway observations obtained from 9 cruises in 1998, 2000, 2002, 2004, 2005, 2009, 2012 and 2013 (between May and October). To facilitate the comparison with the model, we binned LDEO observations into $1/12^\circ \times 1/12^\circ$ grid boxes and normalized them to the year 2015. We then extracted the

simulated pCO_2 values (from May to October) and performed the comparison only using the grid boxes containing observations.

Fig. V.6-a,b,c,d shows the comparison between the seasonal mean pCO_2 from SOCAT and the simulated pCO_2. The model reproduces very well the observed climatological seasonal mean pCO_2 (see Table. V.1). The simulation captures the southeast-northwestward progression of high pCO_2 along the coastal and equatorial upwelling regions throughout the year. The paucity of measurements does not allow a more robust statistical comparison, particularly during Summer and Fall. For instance, only one cruise during March 2002 measured pCO_2 along the coastal zone between 11°S-5°S and that transect alone is the climatological value for Summer. Fig. V.6-e shows a comparison between our model simulation and observations from LDEO. The model captures both the latitudinal gradient of pCO_2 and the regional differences during the cold phase of the year. Statistical metrics are summarized in Table. V.1. MEF values show our results as good, while CF and PB values show that our results are excellent when compared to both SOCAT and LDEO. RI and r indicate that our simulated pCO_2 has the right amplitude and is highly correlated with the observations, respectively. The statistical indicators, RMSE, AE and AAE, showed a good agreement between modeled and observed values. Furthermore, AE shows that the pCO_2 is underestimated by almost 4 μatm, and is overestimated by only 1.2 μatm when compared to SOCAT and LDEO, respectively. These are very small values when compared to a mean pCO_2 of 418 and 432 μatm for the SOCAT and LDEO databases, respectively.

Figure V.6: Seasonal comparison of surface seawater pCO_2 [μatm] between ROMS/PISCES simulation (upper row) and SOCAT V.6 database (bottom row) for a) Summer (JFM), b) Fall (AMJ), c) Winter (JAS) and d) Spring (OND). e) pCO_2 comparison, averaged from May to October, between ROMS/PISCES simulation (upper row) and LDEO database (bottom row)

Table V.1: Statistical metrics of modeled pCO_2 which are: the correlation coefficient (r), the root mean squared error (RMSE), the reliability index (RI), the average error or bias (AE), the average absolute error (AAE), the modeling efficiency (MEF), the cost function (CF), and the percentage of bias (PB), where n is the number of valid points and ΔS is the spatial resolution. All the statistics were applied for the domain of simulation, but Laruelle*, for the nearshore domain.

Model Vs	ΔS	n	r	RI	RMSE	AE	AAE	MEF	PB	CF
SOCAT	1°	540	0.70	1.03	32.2	-4.1	23.8	0.44	1.0	0.55
LDEO	1/12°	3249	0.67	1.04	48.5	1.2	32.4	0.27	0.3	0.57
Rödenbeck	4°×5°	40	0.72	1.03	26.7	9.6	19.5	0.23	2.4	0.63
Landschützer	1°	657	0.80	1.02	22.4	5.4	18.0	0.52	1.3	0.55
Laruelle*	1/4°	545	0.06	1.26	255	236	236	-391	68	18.3

6.2 SOCAT-based products

The Surface Ocean pCO_2 Mapping Intercomparison (SOCOM) (http://www.bgc-jena.mpg.de/SOCOM/) is an initiative that provides several data-based mapping methods that use different versions of the SOCAT database. We compared our results with the Jena CarboScope (oc_v1.6) which provides estimates of global seawater pCO_2 from an observationally-driven ocean mixed-layer scheme derived from SOCAT V.6 (update of Rödenbeck et al. (2014)). A monthly climatology was constructed from 1999 through 2009 from this product (same period as the boundary conditions and the wind stress climatological forcings used in this study). Due to the coarse horizontal resolution of this SOCAT-based product (4° × 5°) the comparison was performed from a large scale perspective. Simulated pCO_2 is well correlated ($r = 0.72$), with high pCO_2 values along the equatorial and nearshore band (not shown). The statistical metrics are shown in Table. V.1, labeled as "Rödenbeck", which rate our results as good/excellent.

We also performed a comparison with another SOCAT-based product in which

a 30-year observationly-based pCO_2 field was created using a 2-step neural network technique, namely the Self-Organizing Map feed-forward neural network (SOM-FFN) method (Landschützer et al., 2015a,b). This gridded sea surface pCO_2 product may be found at http://cdiac.ess-dive.lbl.gov/ftp/oceans/SPCO2_1982_2011_ETH_SOM_FFN. For consistency, a monthly climatology was constructed from 1999 through 2009 in order to perform an annual mean comparison. Our results are in excellent agreement with this SOCAT-based pCO_2 product (see Table. V.1, labeled as "Landschützer"). Spatial differences were found probably due to the coarse horizontal resolution of 1° when compared to our simulations at $1/12^\circ$ resolution. This smoothed reconstructed SOCAT-based pCO_2 is overestimated by our simulations in, approximately, 5.4 μatm with small differences (positive bias) located between 2°S and 10°S (not shown). Despite these small biases all metrics are rated as very good/excellent.

Laruelle et al. (2017) used a modified version of the SOM-FFN method to interpolate seawater pCO_2 data along the global continental margins with an unprecedented spatial resolution of 0.25° at a monthly temporal scale. They successfully reproduce the spatial patterns of pCO_2 across all ocean basins and their seasonality, except for some coastal upwelling regions, such as the shelves of California, Morocco and Peru. The annual mean RMSE between this SOCAT-based product and our simulated pCO_2 is 255 μatm, with maximum errors located within the 100 km-wide coastal strip (not shown). The statistical metrics evaluated the model as poor/bad (see Table. V.1). This weaker performance of the SOM-FFN method in highly productive coastal areas is due to the high-frequency variability and complex physical-biogeochemical dynamics (Laruelle et al., 2017). This is particularly true for the most productive area of the NHCS (nearshore domain) where the interpolated values do not capture the

spatiotemporal variability of seawater pCO_2.

6.3 Comparison with previous observational studies

Our simulation captures an intense offshore gradient of pCO_2 ranging between 500-1000 μatm, in agreement with historical data (Simpson e Zirino, 1980; Copin-Montégut e Raimbault, 1994). This general cross shelf trend of pCO_2 has been observed during comprenhensive sea surface surveys of pCO_2 in the NHCS conducted from 2004 to 2006 (Friederich et al., 2008), which found that the average pCO_2 is above atmospheric values (378 μatm at that time) at all latitudes. The lowest pCO_2 values (150 μatm) and the highest ones (1500 μatm) were found over the shelf near the coast. Our results are consistent with these observations, with lowest and highest values of 235 and 1370 μatm, respectively. Friederich et al. (2008) showed that the most notable characteristic is that pCO_2 decreases with distance from shore for the first 100 km and then stabilizes but remains well above atmospheric values and does not tend towards equilibrium with the atmosphere over the outer 300 km. Thus, our modeled results (see Fig. V.6) are consistent with the observed spatial pattern of pCO_2. They also showed that the air-sea CO_2 fluxes between 4°S-20°S and from 0-350 km from the shore (with most measurements made within the 200 km nearshore band and between 5°S-16°S), exceed 5 mol C m^{-2} yr^{-1} on an annual basis. They estimated 10 mol C m^{-2} yr^{-1} during periods of strong upwelling and 2.5 mol C m^{-2} yr^{-1} during periods of weak upwelling. As the period of strong upwelling/low productivity occurs during Winter and the period of weak upwelling/high productivity occurs during Summer, we can consequently compare our results with their observations within the nearshore domain. Our simulated air-sea CO_2 fluxes, over similar spatial

criteria, are 9.2 and 2.2 mol C m^{-2} yr^{-1} during Winter and Summer, respectively, while the annual mean is 5.6 mol C m^{-2} yr^{-1}, which is very close to the observed air-sea CO_2 fluxes. Although most cruises occurred during Winter-Spring, Friederich et al. (2008) estimated an annual mean flux of carbon of 5.7 mol C m^{-2} yr^{-1}, which represents an integrated flux of 0.055 Pg C yr^{-1} when applied to an area encompassed by 2000 km of coastline and 400 km from the shore. For comparison, we estimated an annual mean flux of 4.15 $\pm$ 2.21 mol C m^{-2} yr^{-1}, representing an integrated evasion flux of 0.041 $\pm$ 0.022 Pg C yr^{-1} under similar spatial criteria, which are 400 km from the shore but from 2 to 20°S (approximately 2000 km of coastline). Estimates for the regional and nearshore domain in this study are shown in Table. V.2. In summary, our results are in excellent agreement with the observed seawater pCO_2 and associated air-sea CO_2 fluxes, which are consistently positive in the region, i.e. from the ocean to the atmosphere. Therefore, our simulation is robust enough for proceeding to the analysis of the mechanisms and drivers affecting pCO_2 variability, in a climatological sense, in the NHCS.

Table V.2: Air-sea CO_2 flux in [mol C m^{-2} yr^{-1}] and associated integrated carbon flux in [Pg C yr^{-1}] for the regional and nearshore domain. A comparison between observed values (denoted as Friederich) and modeled results (denoted as Model) is also included. The minimum (min), maximum (max), mean and temporal standard deviation (std) values are shown.

This study	**Spatial coverage**	**Air-sea CO_2 Flux [mol C m^{-2} yr^{-1}]**				**Integrated Carbon Flux [Pg C yr^{-1}]**			
		min	**mean**	**max**	**std**	**min**	**mean**	**max**	**std**
Regional domain	from 0 to 20°S and from 70°W to 90°W	1.07	1.91	2.90	0.71	0.040	0.070	0.110	0.030
Nearshore domain	from 5°S to 17°S and 300 km from the shore	1.45	5.60	9.50	2.94	0.007	0.028	0.048	0.015
		Comparison							
Friederich	2000 km of coastline and	-	5.70	-	-	-	0.055	-	-
Model	400 km from the shore	-	4.15	-	2.21	-	0.041	-	0.022

7 Hindcast outputs and associated inferred pCO_2

Two of the most anomalous months in the period of analysis (1998-2015) were chosen in order to illustrate the comparison between modeled and observed SST and chlorophyll-a (Chla) during the largest ENSO peaks. These months are January-1998 and November-2007, for El Niño (ICEN=+3.4) and La Niña (ICEN=-1.92), respectively. Satellite-derived observed SST was extracted from the Advance Very High Resolution Radiometer (AVHRR) Pathfinder (Casey et al., 2010) and from the Moderate-resolution Imaging Spectroradiometer (MODIS) (http://modis.gsfc.nasa.gov/), for Jan-1998 and Nov-2007, respectively, both at $1/12^{\circ}$ horizontal resolution. Chla was obtained from the European Space Agency Ocean Colour Climate Change Initiative (ESA OC-CCI Version 3.1) (http://www.esa-oceancolour-cci.org/), which is a long-term multi-sensor satellite ocean-colour data at $1/12^{\circ}$ horizontal resolution. Fig.V.7 and Fig.V.8 demonstrate that the large scale spatial pattern and main features during both ENSO peaks are very well captured by the model, despite that the model horizontal resolution is three times coarser than observations. During El Niño Jan-1998, anomalous warm waters are found in almost the entire domain. In contrast, during La Niña Nov-2007, the equatorial and coastal upwelling fronts are reproduced, evidenced by cold waters along the Equator and the Peruvian coast. The spatial distribution of Chla during both ENSO peaks is consistent. Low Chla concentrations are found at the nearshore strip during El Niño Jan-1998. The highly productive band ($\sim$2 mg m^{-3}) extended over a wider offshore area during La Niña Nov-2007, and the oligotrophic oceanic region at the southern domain remains with low Chla concentrations but an order of magnitude larger than during El Niño Jan-1998 peak.

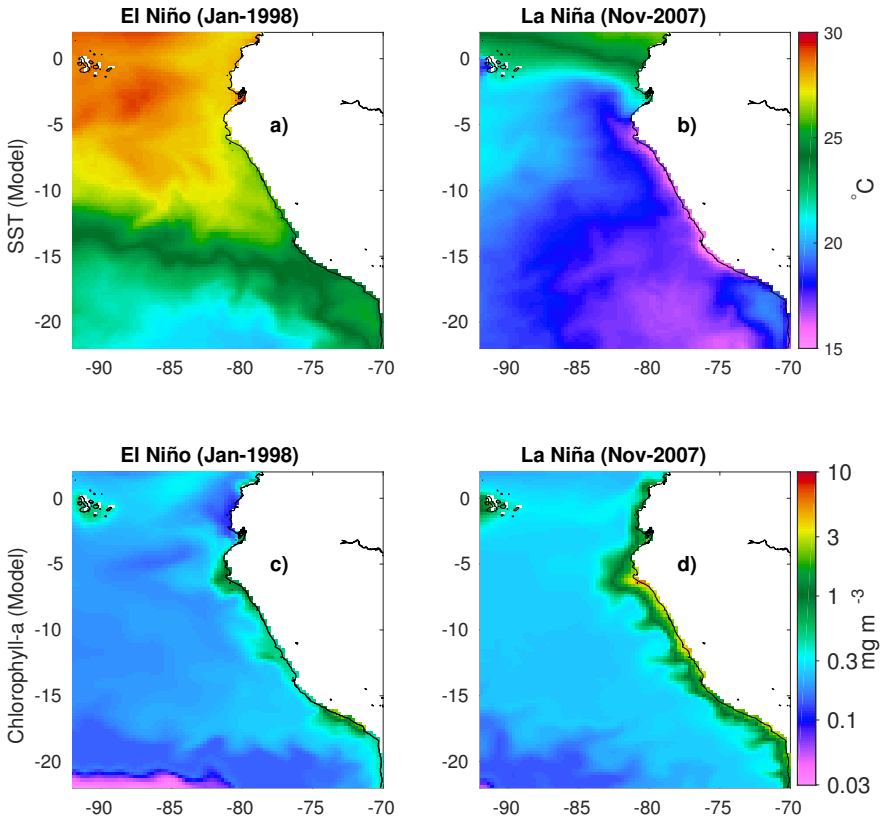

Figure V.7: Upper row: modeled SST of a) January-1998 and b) November-2007, for El Niño (ICEN=+3.4) and La Niña (ICEN=-1.9) peak, respectively. Similarly, the bottom row is for modeled chlorophyll in panels c and d.

In order to have an insight into the performance of the methodology in reproducing the carbonate system, Fig.V.9 shows the comparison between inferred and observed pCO_2^{sw}. Only the second half of the period of analysis, from 2007 to 2015, is shown because observations (almost a quarter of the total valid points: 120) have been sparse and spatially isolated from 1998 to 2006. The database used is the Surface Ocean CO_2 Atlas database, SOCAT V.6 (Bakker et al., 2016). For consistency, the observed fugacity of CO_2 from SOCAT was converted to pCO_2 using the CO2SYS program (Van Heuven et al., 2011), and only the grid boxes containing observations were considered in order to perform the spatial means. Inferred pCO_2^{sw}

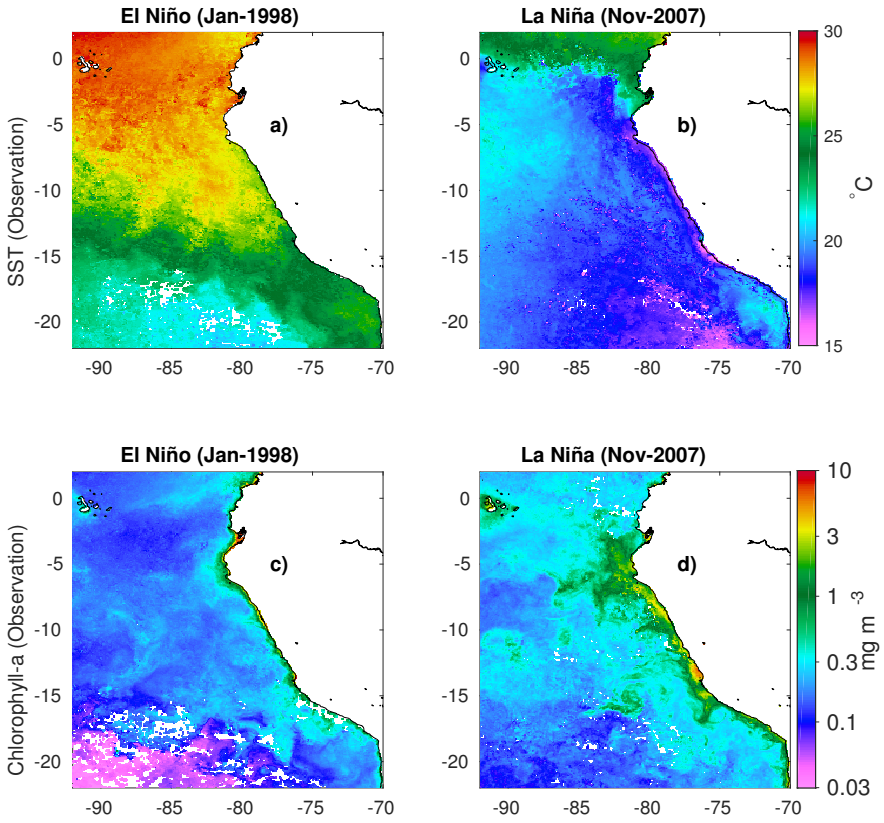

Figure V.8: Upper row: observed SST of a) January-1998 and b) November-2007, for El Niño (ICEN=+3.4) and La Niña (ICEN=-1.9) peak, respectively. Similarly, the bottom row is for observed chlorophyll in panels c and d.

oscillates at the right amplitude (reliability index = 1.01 and root mean square error = 12 μatm), and is highly correlated with observations ($r = 0.76$). It captures the southeast–northwestward progression of high pCO_2^{sw} along the coastal and equatorial upwelling regions (bias = +6 μatm), as shown in the inset of Fig.V.9. An EOF analysis was performed (not shown) within the upwelling region for the inferred pCO_2^{sw} which has been previously detrended, the mean removed, and the seasonal cycle removed. The first mode of variability (EOF1) of the pCO_2^{sw} anomaly represents 77% of the total variance, and its respective principal component is correlated with ICEN ($r = 0.6$). A periodicity of 3.5 and 2.5 years was detected in the signal of the pCO_2^{sw}

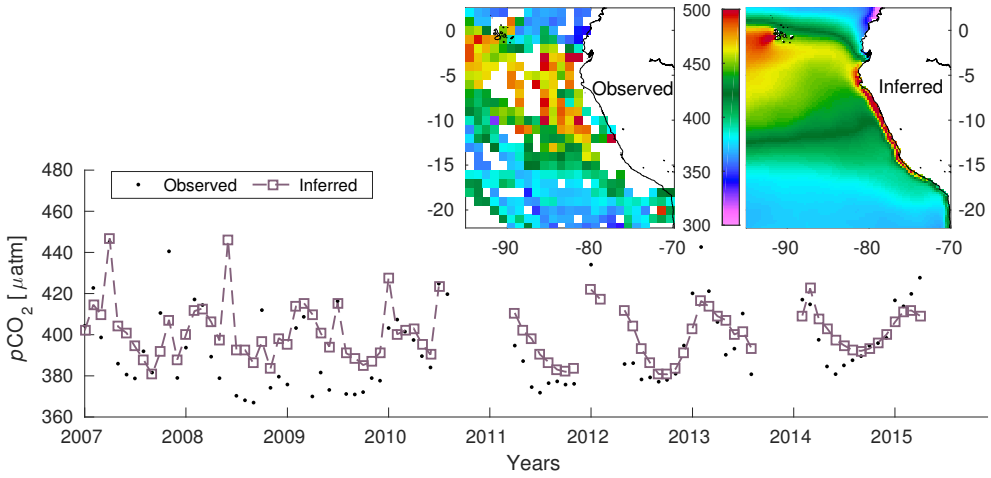

Figure V.9: Time series of observed and inferred pCO_2^{sw} throughout the second half of the analysis period. These values are the spatial average into the whole domain of analysis considering only the grid pixels containing observations. The insets show the annual mean spatial map of both observed and inferred pCO_2^{sw} in μatm.

variability, which is unequivocally related to the ENSO's signal. Overall, a high degree of reliability about the methodology here applied was obtained and the interannual response related to the oceanic carbon cycle was succesfully captured. Therefore, the mechanisms linking ENSO and the variability of the CO_2 efflux could be assessed.

Chapter VI

Global Warming-induced wind patterns on primary production

1 Wind intensification

Fig. VI.1 shows a time series of the monthly zonal and meridional wind stress components from CCMP V2. Blue crosses are original raw monthly data, the black continuous line denotes the filtered data (moving average seasonal low pass filter). The red line is least-squares fitted linear trend, and the green line is the long-term mean of each series (see also Section 5.1). The slope for each fitted line is -6.13×10^{-5} and 1.20×10^{-4} N m^{-2} month^{-1}, for the zonal and meridional components, respectively (significance level $p < 0.00001$). The negative sign of the zonal slope means that the zonal component of the wind is strengthening westward, while the positive sign of the meridional slope means that this component is strengthening northward. During almost a decade the zonal and meridional component were enhanced (with respect to their long-term mean) by, approximately, 38.5% and 33.5% respectively.

Narayan et al. (2010) found a slope of 0.4×10^{-4} N m^{-2} month^{-1} for the meridional wind component using COADS (four times coarser than CCMP horizontal resolution) from 1960 to 2000. This value is a third of the slope estimated in our period of analysis. The scale of the coastal intensification (tens of kilometers) could partially explain this difference (Bakun et al., 2010). On the other hand, Bakun (1990) found a slope of 4.5×10^{-3} N m^{-2} month^{-1} from a 30-year linear trend (from mid 50s to mid 80s) of the alongshore wind stress estimated between 4.5°S and 14.5°S within the coastal area. This value is larger than the one used in this paper, basically because we calculated the trend from the meridional rather than the alongshore component of the wind stress, from 6°S to 15°S and over a wider area (200 km). The difference could also be explained by the different period chosen for the analysis. Furthermore, uncertainty may arise from an artificial long-term increasing trend on the winds due to temporal trends in ship sizes and associated anemometer heights, trends in relative frequencies of measured winds and nonhomogeneities in recording and archiving practices (Bakun et al., 2010). Within our spatio-temporal domain of analysis, we found that the magnitude of the averaged meridional component of the wind stress is actually more than twice ($\sim$2.3 times) the zonal one, which is reflected in a total wind intensification of 34.2$\%$ during a decade. Since there exists low confidence in common trends in upwelling-favorable winds among EBUS's (Narayan et al., 2010; Stocker, 2014), we may not discard the role of multi-decadal climate variability in the observed trends. Thus, these findings, related with the wind intensification percentages, should not be viewed as predictions, but rather as reference values in order to perform a sensitivity study. In order to reproduce the increase of upwelling-favorable winds in the NHCS, the zonal and meridional wind stress components were increased by 40$\%$ and 35$\%$, respectively.

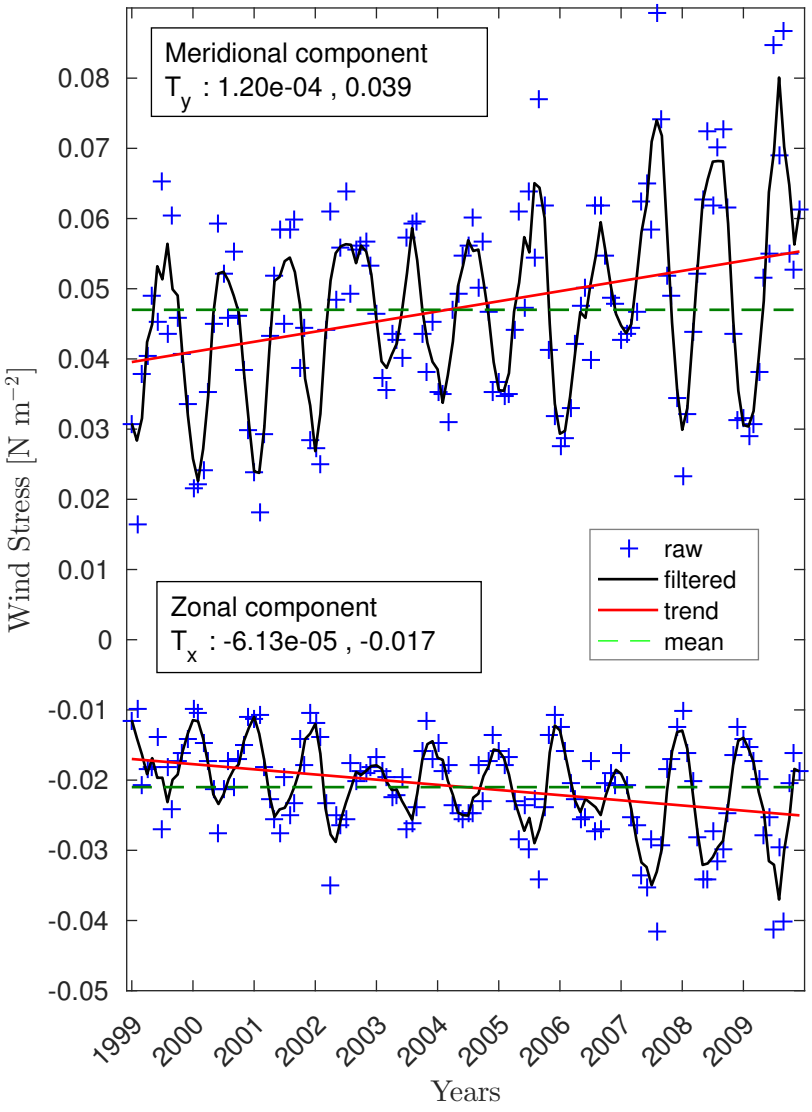

Figure VI.1: Time-series of the monthly zonal and meridional wind stress components from CCMP V.2 [N m^{-2}]. The slope and the intercept of the fitted lines are shown in the insets.

2 Effect of the induced wind trend on biological production

Fig. VI.2 shows the annual mean latitudinal distribution of PP and the limitation factors (NL and GR). Blue lines are the results associated to the modern winds experiment while the red lines are the results for the increased winds experiment. The percentage variations between both experiments are shown on the right panel. On average, intensified winds induce more nutrient supply and an increase in PP. This effect, however, is not uniform in the coastal upwelling zone. An equatorward trend of PP intensification of, approximately, 2 $\%$ per latitudinal degree, is found starting from Chimbote. The maximum relative PP increase of, approximately, 15$\%$ occurs at southern Callao and southern San Juan. In general, PP is increased by, approximately, only 5 mol C m^{-2} yr^{-1}. While PP increases in the whole domain in response to increased winds, two important regions experience a decrease in PP, which is evidenced by a negative relative percentage variation of around -3$\%$, as seen in Fig. VI.2-b. Note that another minimum occurs at southern Chimbote, where the relative percentage variation is zero. We investigate in detail the response of these counterintuitive zones in order to understand their resilience to increased upwelling-favorable winds and assess their overall importance in the behavior of this important EBUS to climate change.

As seen in Fig. VI.2-c,d, NL increases, on average, 10$\%$ within the domain (as NL increases, it yields a lower nutrient limitation status). The maximum relative increase of around 20$\%$ occurs in the northernmost area and between Pisco-Callao. Note that the regions that exhibit a counterintuitive response have the lowest NL values, meaning that phytoplankton growth is more limited by the availability of nutrients in

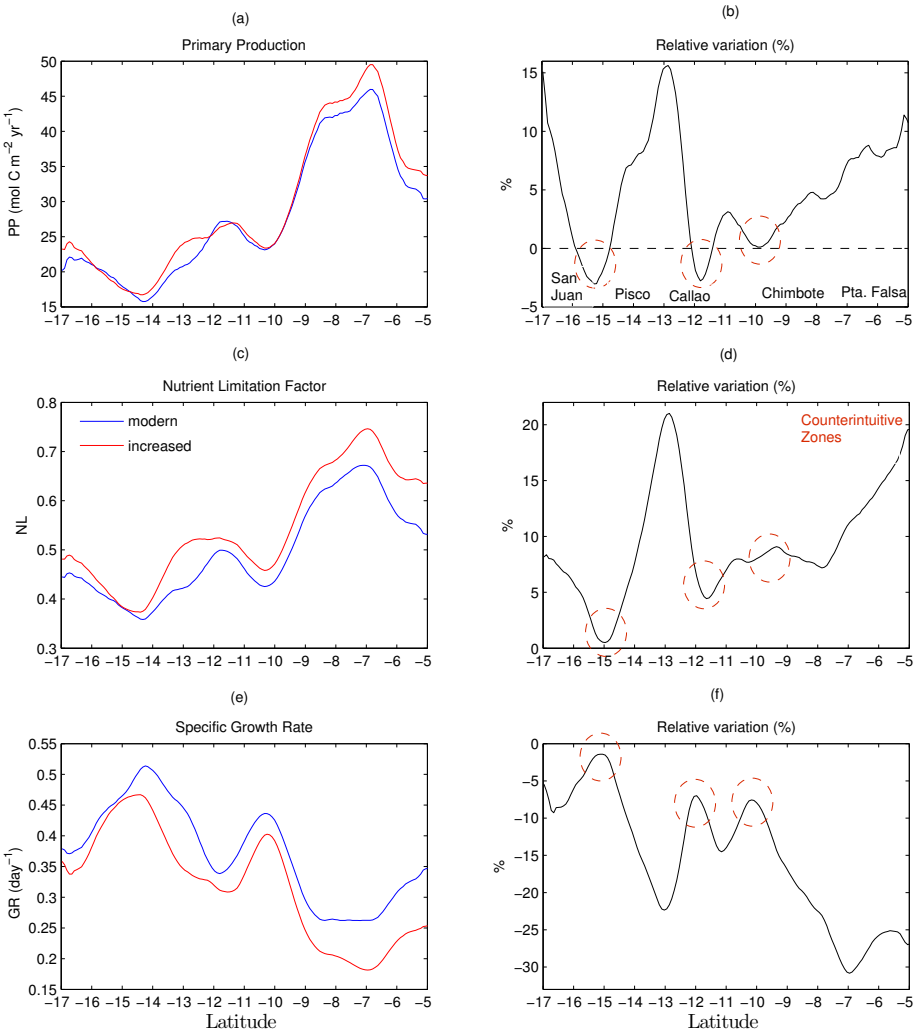

Figure VI.2: (a) Annual mean latitudinal distribution of vertically integrated (within ZEU) primary production. (c) Annual mean latitudinal distribution of vertically averaged (within ZEU) nutrient limitation term (e) Annual mean latitudinal distribution of vertically averaged (within ZEU) specific growth rate. Panels b,d and f, are the percentage relative variation of PP, NL and GR between modern (blue line) and increased (red line) winds experiments, respectively. All the quantitites were averaged within the first 300 km nearshore band. Red dashed circles depict the counterintuitive zones.

these areas than the rest of the domain. However, since these regions are important upwelling centers along the Peruvian coast, the lower NL values may result from an increased eddy-driven export of nutrients rather than a lack of nutrients. We explore this possibility in the next section.

Under increased winds GR decreases, on average, 15% (see Fig. VI.2-e). The maximum GR is found within the counterintuitive zones, but since we demostrated that these key regions exhibit relative strong NL status, GR is ultimately controlled by temperature ($\lim_{\mathrm{NL}\to 0} \mathrm{GR} \approx f(T)$). The dependence of the Eppley relation (Eq.1) on temperature explains the negative variation in GR. Enhanced upwelling supplies colder waters to the surface. Modeled temperature (averaged over the ZEU) decreases 5% (about 0.85°C) under the increased winds scenario. The correlation coefficient between temperature and PP for the modern winds experiment is -0.73, while for increased winds it is -0.83. The simulated GR beyond our latitudinal limits of analysis showed larger rates near the Equator and southern San Juan (not shown). This is due to an interplay between warmer waters and well lit areas, rather than the temperature-dependent shift that occurs along the Peruvian coast under the increased winds scenario.

3 Eddy-driven effects on primary production

If we assume that nutrient availability and nutrient use efficiency (i.e. NL and GR) are equally important in controlling PP, we obtain a 5% deficit (since GR decreases 15% and NL increases 10%) that may be attributed to other physical factors under the increased winds scenario. These factors negatively influence PP in the NHCS. This

is because the strengthening of the winds may also induce other non-linear effects on primary production, arising as by-products of the induced trend. In order to assess this influence and understand the latitudinal variability of PP (see Fig. S2 of the supporting information), we focus in two mechanisms. The first is the eddy-induced horizontal advection of nutrients and the second is the local effect of wind mixing, as it induces a turbulent habitat and deepens the mixed layer impacting PP.

3.1 Off-shore leaking of nutrients

Our model results show that PP is higher in the northern coastal domain. This is supported by satellite observations (see Fig. V.2), which shows a decrease in production rates from, approximately, 9°S to 14°S. This latitudinal band coincides with regions of high Eddy Kinetic Energy (EKE), which is a measurement of the mesoscale eddy activity. Fig. VI.3-a shows the annual mean latitudinal distribution of EKE (red line).

A region with moderate EKE (10 cm^2 s^{-2}) is found at the southernmost region between San Juan and Pisco (∼16°S). A peak of EKE is found in the central NHCS between Callao (12.1°S) and Chimbote (9.4°S) with a mean EKE of, approximately, 20 cm^2 s^{-2}. The difference in the level of mesoscale activity in these two key regions may induce different responses in PP. This hypothesis was initially proposed by Gruber et al. (2011), who suggested that eddies suppress production in highly productive EBUS's. The mechanism consists in a leaking of the coastal nutrient inventory by horizontal advection of nutrients into the oligotrophic ocean, eventually leading to a reduction of biological production in the coastal zone. Mogollón e Calil (2017) demonstrated that the cold ENSO phase, La Niña, induces an increase in EKE in the

southern NHCS, which leads to substantial offshore nitrogen advection (in the form of nitrate) at a rate of 0.5 kg N $m^{-2}day^{-1}$ at the surface.

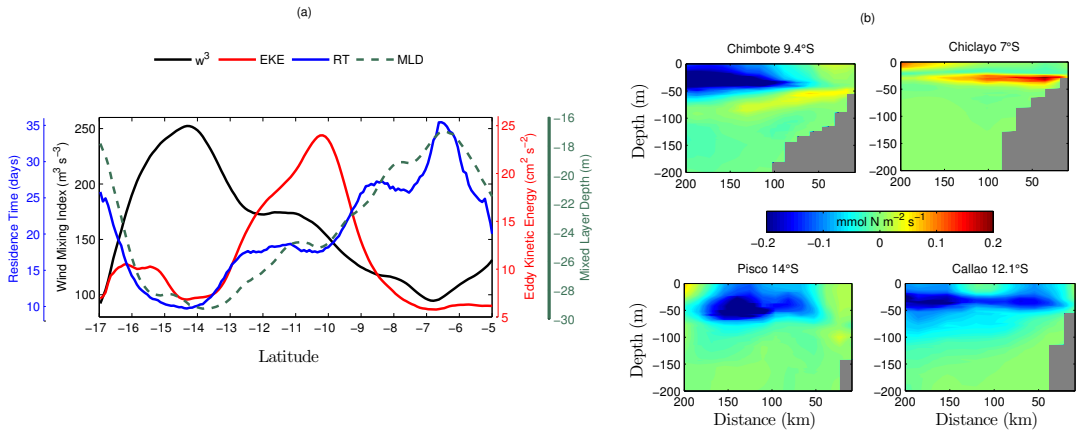

Figure VI.3: (a) Annual mean latitudinal distribution of residence time (blue line), wind mixing index (black line), eddy kinetic energy (red line) and mixed layer depth (green dashed line). (b) Cross-shore vertical sections of the horizontal eddy-induces fluxes of total inorganic nitrogen (TIN) [mmol N m^{-2} s^{-1}] at four different locations, as indicated, for the increased winds experiment. Positive (negative) values mean onshore (offshore) TIN fluxes.

In order to quantify the efficiency of this mechanism, Fig. VI.3-b shows vertical cross sections of the horizontal eddy fluxes of TIN (in mmol N $m^{-2}s^{-1}$) at 7°S, 9.4°S, 12.1°S and 14°S. These locations were chosen in order to illustrate the latitudinal differences among important upwelling centers. Positive eddy fluxes are found over the shelf at Chiclayo (7°S) and Chimbote (9.4°S). However, negative horizontal eddy fluxes are found from 70 km from the coast in the upper 50 m for Chimbote. This demonstrates that an offshore export of nitrogen (in the form of nitrate + ammonium) is occurring, removing inorganic nutrients at a rate of -0.35 mmol N $m^{-2}s^{-1}$. Callao and Pisco exhibit a similar pattern with export rates of -0.20 and -0.25 mmol N

$m^{-2}s^{-1}$ respectively. We can now relate the level of mesoscale activity (red line in Fig. VI.3-a) with the four panels in Fig. VI.3-b. The lowest EKE values are found in the northern domain, where positive eddy-induced fluxes of TIN are found. The largest EKE peak occurs between Chimbote and Callao at the central domain of analysis, where high rates of negative eddy-induced flux of TIN are found. In spite of Pisco having low EKE values, when compared to the whole domain, it exhibits a nutrient-leaking pattern similar to Chimbote or Callao. This response could be associated with other eddy-driven factors, such as the change in orientation of the Peruvian coastline, bathymetric features or wind-mixing energy production. The latter is assessed in the next section.

3.2 Mixing and residence times

The more equatorial location of the NHCS yields stronger Ekman transport for similar wind speeds when compared to other EBUSs. For example, Bakun e Weeks (2008) found that the wind speed in the California CS (Cape Mendocino) needs to be twice the value observed along the Peruvian coast (Chimbote) in order to produce a similar rate of upwelling. However, winds also induce turbulent mixing, which is roughly proportional to the third power of the wind speed. Large wind-induced turbulence is disadvantageous for primary production as it tends to deepen the mixed layer and dilute phytoplankton in the water column.

In order to assess the importance of the wind mixing on PP, we follow the methodology of Bakun e Weeks (2008), who defined the wind mixing index as the cube of the wind speed (w^3). In Fig. VI.3-a, the black line denotes the annual mean

latitudinal distribution of the wind mixing index. The southern domain has larger values of w^3 than the northern domain, with two relative maxima. The largest w^3 is located between San Juan (15.7°S) and Pisco (14°S). This was expected due to the proximity of the eastern part with the South Pacific subtropical anticyclonic gyre. The other peak is located north of Callao. Note that the latitudinal distribution of the mixed layer depth is negatively correlated with the wind mixing. In the southern domain, the mixed layer is almost twice deeper than in the northern domain, allowing a deeper penetration of wind-driven turbulence. Thus, the counterintuitive zones are disadvantageous for primary producers along the southern and central Peruvian coast. Furthermore, under modern winds, the correlation between PP and the wind mixing index is -0.86, which suggests that PP is strongly modulated by changes in the wind forcing. Note that the counterintuitive zones, where we found the largest levels of wind-driven mixing when compared to the rest of the domain, exhibit lower primary production rates. The key to understand the inverse relationship between wind-driven mixing and PP, relies on the efficiency of nutrient recycling and the effective retainment within the productive upper layers. The lack of exposure to intense turbulent mixing would be beneficial to primary producers in the NHCS. To have an insight on these two mechanisms, which were initially proposed by Bakun e Weeks (2008), we estimated the theoretical residence time along the Peruvian coast. Longer residence times are usually associated with lower turbulent activity, hence, we may use the residence time as a proxy of these two mechanisms at work. Fig. VI.3-a shows the annual mean latitudinal distribution of RT in days (blue line). RT and w^3 are inversely correlated (-0.9). The larger the wind mixing, the shorter the residence times. This explains the higher PP rates in the northern portion of the domain, as opposed to lower values in the central or southern domain, where the counterintuitive zones are located.

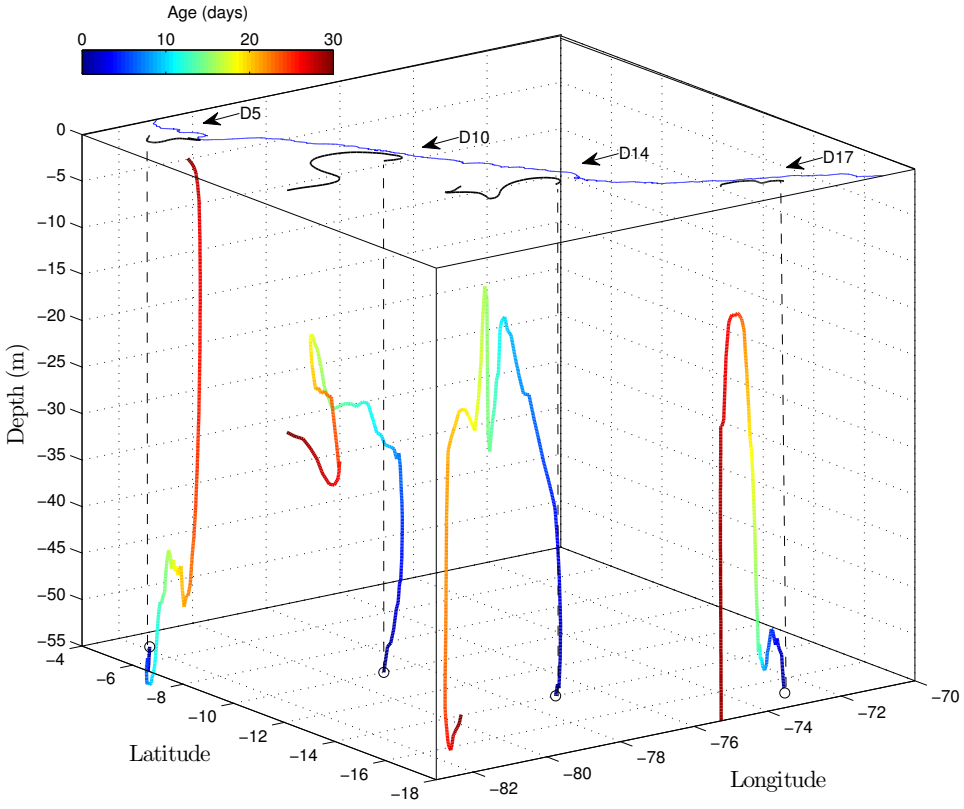

Figure VI.4: Averaged Lagrangian trajectories of the four clusters of drifters deployed at 5°S (D5), 10°S (D10), 14°S (D14) and 17°S (D17) during the climatological August (30 days). Colors denote the age in days. The black contours at the surface are the 2D projection of the trajectories.

A Lagrangian experiment helps illustrate how the mechanism works (see Fig. VI.4). The residence times of the modeled drifters agree remarkably well with the theoretical one, although the latter represents the annual mean. Results show that the central portion of the NHCS is more affected by meso and submesoscale structures, such as filaments, that effectively advect coastal waters into the open ocean, which is

evidenced by the scattered pattern in the central NHCS. Although characterizing the dynamics of the upwelling filaments is beyond the scope of this work, the impact of these features on the overall biogeochemistry of this EBUS deserves further attention and should be addressed in a future study. Furthermore, as the largest w^3 index is found at 14°S, the cluster released at this latitude exhibits a different vertical pattern, in which a substantial amount of offshore downwelling occurs, as evidenced by a sharply deepening of the trajectory in the southern drifters during the end of the month. This is in agreement with Gruber et al. (2011), who suggested that eddy-induced subduction and offshore transport remove inorganic and organic nutrients from the nearshore and potentially enrich the offshore region. Accordingly, there exists a latitudinal trend in which the eddy-induced subduction effect weakens equatoward. As a consequence, the northern domain is less impacted by this mechanism when compared to the southern domain. This helps to explain the latitudinal variability of PP (see Fig. V.2). The width of the shelf, which may be another factor that impacts particle residence times and, hence, biological production, remains unexplored. However, based on our results, we speculate that a wider continental shelf would lead to longer residence times, thus favoring primary production.

4 Temporal Variability

The temporal variability for all variables previously discussed is summarized in Fig. VI.5, where results are shown as monthly-averaged time series for the modern winds experiment. We decided not to show the time series for the increased winds experiment because both solutions exhibit almost the same temporal pattern with some slight differences in the amplitude (PP and production terms). However, we detailed

these important differences as follows: Under the increased winds scenario, PP increases from Winter to Summer. During Fall and early Winter (AMJJ) no significant differences are observed (only a decay in productivity between 1 to 2% under increased winds). During Summertime (JFM), PP increases almost 13% (from 31 to 35 mol C m^{-2} yr^{-1}) under increased winds. A yearlong increase of, approximately, 10% of the NL factor is obtained in both scenarios. Similarly, the GR is about 15% lower under increased winds than in the modern winds experiment throughout the year.

Wind mixing is larger and residence times are shorter during Fall and Winter. The EKE is maximum in March, July and November. Our results suggest that in the NHCS there exists a coupling between the eddy-driven export and wind mixing during late Fall and early Winter, i.e. June and July, as evidenced in the bottom panel of Fig.VI.5 (black and red lines). In contrast, during the rest of the year, they are both negatively correlated. This could partially explain the so-called "Peruvian paradox" (Pennington et al., 2006; Echevin et al., 2008a), which consists in an offset between the stronger upwelling period (austral Winter) with the lower rates of primary production. This opposite relationship is clear when we compare the time-series of PP and w^3 (dark green and black line, respectively). During Winter the NL status decreases (higher NL values) due to larger nutrient concentrations in the euphotic zone. However, the enhanced coastal upwelling also leads to a decrease in the nutrient use efficiency partially due to a cooler environment (lower GR rates). Thus, the combined opposite effect of these two production terms partially control the seasonal cycle of PP in the NHCS. In addition, the euphotic layer fluctuates around 40$\pm$3 m depth, with a maximum depth during Summer and a minimum one during late-Winter/early-Spring (not shown). As a consequence, no significantly temporal variability is related to the

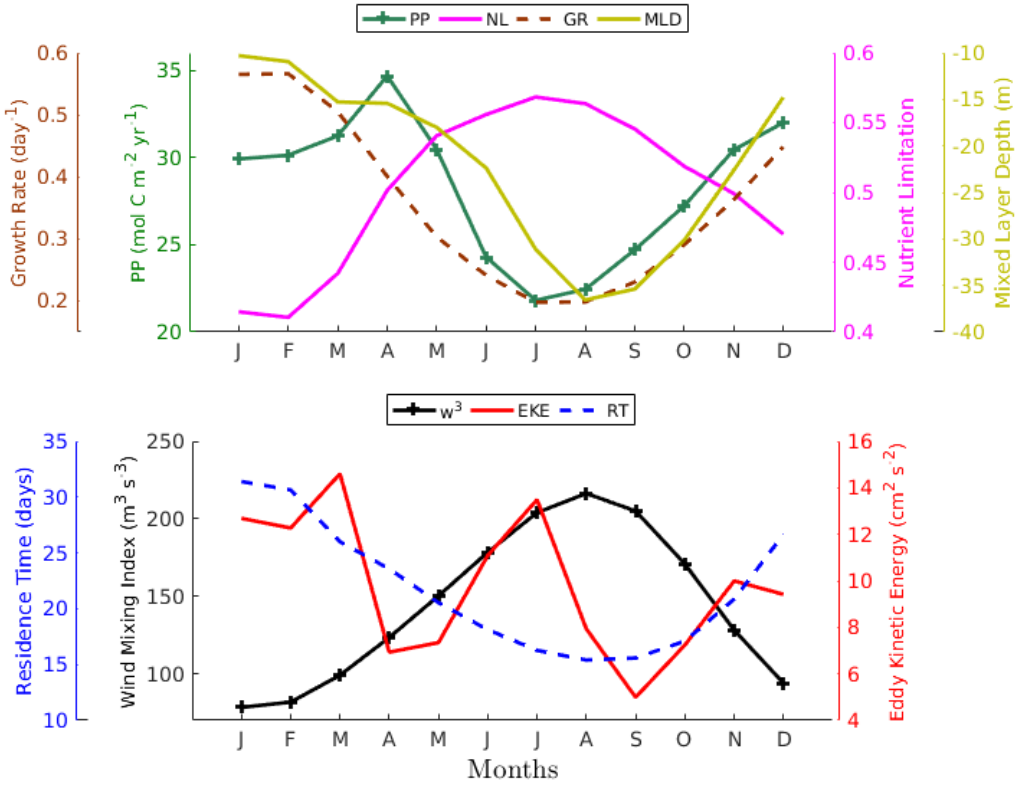

Figure VI.5: Monthly time series of primary production, growth rate, nutrient limitation and mixed layer depth for the modern winds experiment (upper panel). The residence time, wind mixing index and eddy kinetic energy are displayed at the bottom panel. The residence time was averaged within the first 100 km nearshore band. The rest of the quantities were averaged within the first 300 km nearshore band and between 5°S to 17°S.

well lit zone. However, the seasonal cycle of PAR (not shown) follows GR, with a maximum value of 260 W m^{-2} during Summer and a minimum value of 125 W m^{-2} during Winter.

Our results are in agreement with Echevin et al. (2008a), who demonstrated that the surface chlorophyll concentration is highest in austral Summer and decreases during austral Winter, in phase opposition with the coastal upwelling intensity. They demonstrated that the seasonal cycle of surface chlorophyll is mainly controlled by the mixed layer depth, which deepens during Winter and dilute the surface chlorophyll concentration by entraining waters from below the mixed layer. In fact, our simulated mixed layer gets, on average, 18% deeper along the year under the increased winds scenario (not shown). Thus, we suggest that the global warming-induced strengthening of the upwelling-favorable winds will ultimately lead to a deepening of the mixed layer with strong impact on biogeochemical processes, such as entrainment/recycling rates of nutrients. This deepening would mitigate the effects of the acceleration of the upwelling circulation by preventing abrupt changes in production rates, thus yielding a more resilient biological response in the NHCS. The absence of the counteractive mechanisms would probably result in a proportional increase in primary production to the wind perturbation, as found in other EBUS's. One possible explanation for the resilience of the NHCS is that the deepening of the mixed layer buffers an increase in primary production under increased winds.

5 Bakun's hypothesis

In order to have an insight of the trends of atmospheric CO_2 and evaluate Bakun's hypothesis along the NHCS, we used NOAA's CarbonTracker (CT2016) (Peters et al., 2007), which is a global model of atmospheric carbon dioxide designed to keep track of the CO_2 uptake and release at the Earth's surface since 2000 at 1 degree resolution. Fig. VI.6-a shows a thermal low pressure zone developed over the continent and a high pressure zone at the adjacent ocean. In agreement with Bakun's hypothesis, a warming trend and a weakening of the surface pressure are obtained. The air temperature increased 0.45°C associated with a slight decay on air surface pressure over the decade of analysis. The fluctuations in air surface temperature highly covary with El Niño/La Niño episodes, as expected (Indice Costero El Niño (ICEN), an ENSO index computed exclusively for the Niño 1+2 region, i.e, coast of South America, was used (Takahashi K., 2014). A time-series only for the oceanic portion of the domain of analysis did not show a clear trend, probably due to its relatively coarse resolution resulting in an inadequated representation of land-sea pressure gradients. This could be attributed to the fact that the wind trends might be more sensitive to the poleward migration of the oceanic high pressure cell rather than changes in the continental thermal low-pressure system (Rykaczewski et al., 2015). With basis on these findings, we suggest that the net strengthening of the upwelling favorable winds along the Peruvian coast is a consequence of surface warming over land in combination with a poleward expansion of the oceanic high pressure cell (García-Reyes et al., 2013), which partially tends to decrease its magnitude.

Fig. VI.6-b shows the components of atmospheric pCO_2 (sea+land and excluding

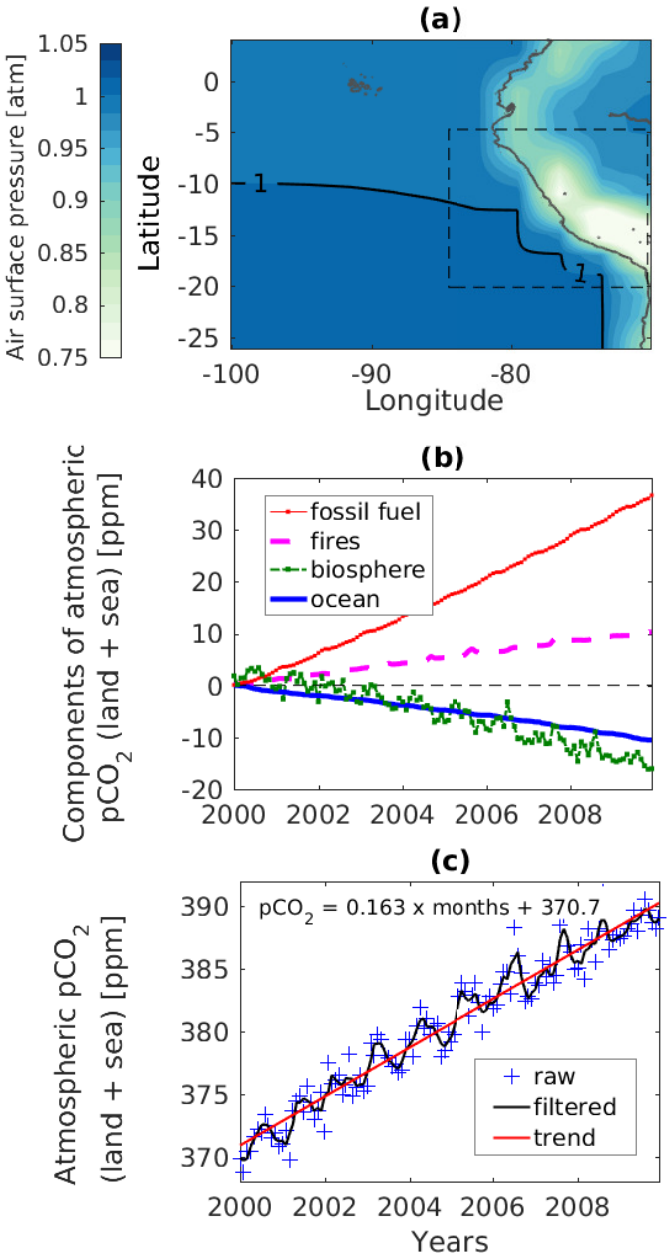

Figure VI.6: (a) Annual mean air surface pressure [atm]. The black dashed square represents the domain of analysis in which all the calculations were performed (from 5°S to 17°S). (b) Time series of the components of atmospheric pCO_2 excluding the yearly background. (c) Time series of total atmospheric pCO_2. The equation shows the linear fit.

the yearly background). These components are the fossil fuel (red line), wildfires (magenta dashed line), land-biosphere (as green) and the air-sea exchange (continuous blue line). The air-sea exchange of CO_2, (photosynthesis and respiration by the terrestrial biosphere) represents an important sink in the budget of atmospheric CO_2. Since the middle of the decade of analysis, the biosphere contribution becomes greater than the oceanic one. The release of CO_2 to the atmosphere by fires is smaller than the contribution of fossil fuels. According to Bakun's hypothesis, anthropogenic emissions are the main source of atmospheric CO_2, which is occurring along the Peruvian coast. Moreover, the averaged contributions along the decade for fossil fuels and fires are 17.2 and 5.3 ppm, respectively. Meanwhile, the contributions of the biosphere and the ocean are, approximately, -5.6 and -5 ppm, respectively. These estimates exclude the initial CO_2 concentrations in the atmosphere.

In general, atmospheric pCO_2 is more uniform over the ocean (not shown), with a smoothed increase towards the Equator and a steep gradient shoreward. Our domain is suited to perform this sensitivity study because we capture large horizontal gradients of surface atmospheric temperature, pressure and pCO_2. Fig. VI.6-c shows the time-series of the total pCO_2 (sum of all the CO_2 components with the yearly background). A positive trend is obtained because the source terms are larger than the sink terms, as previously discussed. Using Least Squares, a slope of 0.163 ppm per month is found which translates to an increase of, approximately, 2 μatm per year of pCO_2 in the atmosphere at the coastal Peruvian upwelling region mainly due to anthropogenic emissions.

6 Biological response

Previous studies in other EBUS's found that regions with low initial nutrient limitation status (high NL values) tend to be more resilient to wind changes, while regions with high initial nutrient limitation (low NL values), increase their nutrient limitation status and hence PP substantially (Lachkar e Gruber, 2013). However, this general behavior does not explain the biological response in the NHCS. We found that regions with low initial NL values (such as the counterintuitive zones) do not significantly increase their limitation status under an increased winds scenario. Moreover, the northern domain, which is characterized by higher NL or weak limitation status, substantially increased its limitation status under increased winds scenario. As a consequence, our findings suggest that the counterintuitive zones are the most resilient (in terms of the biological response) to the global warming-induced upwelling intensification trend.

Overall, as the highest GR are found in the southern and central portion of the domain, it appears that the nutrients are being more efficiently used in these regions (particularly within the counterintuitive zones) than over the northern domain. Despite their relatively lower rates of primary production, it agrees with Bakun et al. (2015). They suggest that the increased intensity of the upwelling-favorable winds could lead to less phytoplankton production within the primary upwelling zone due to deeper wind-driven mixing and increased light limitation. However, this moderate primary production (which would in turn sustain zooplankton and upper trophic level communities) does not necessarily lead to smaller fish production, according to Bakun e Weeks (2008), who emphasizes the notion that in the ocean, "food heaven" generally coincides with "predation hell", because fish production usually

depends more on recruitment success than on food availability. Furthermore, Salvatteci et al. (2018) suggest that a long-term increase in coastal upwelling due to the warming climate, at least up to the start of the 21st century, is favourable for fisheries productivity in the HCS. Our results show a moderate increase in primary production and suggest that its spatiotemporal variability is a result of a delicate interplay between nutrient availability and nutrient use efficiency. This is reflected in the opposite relationship between NL and GR which tend to balance each other out.

Previous studies have suggested that PP will decrease with the increased stratification associated with future surface warming, given the inverse relationship between ocean temperatures and ecosystem productivity in observations (Sarmiento et al., 2004; Behrenfeld et al., 2006). For instance, Brochier et al. (2013) found that the expected surface global warming will increase stratification, with strong impacts in the circulation and mesoscale activity in the Humboldt CS. Both physical changes would in turn negatively affect PP due to the impact on nutrients and oxygen contents and due to the strong reduction of the offshore extent of the productive area. The latter appears that is not fully compensated by the increase in retention rates on the continental shelf. As a consequence, they predict a future reduction in small pelagic fish recruitment in the Humboldt CS. In sharp contrast, Rykaczewski e Dunne (2010) obtained a counterintuitive increased nutrient supply (attributed to nitrate enrichment of deep source waters) which results from long-term warming and stratification in the North Pacific California Current Ecosystem, demonstrating that local responses to changing climate can differ significantly from the general global response. In our work, which consisted in a single factor tuning methodology (modern and increased winds scenarios), the surface warming effect (and associated increased water-column

stratification) is neglected because we kept the same heat fluxes in both control and perturbed simulation. The combined effect of wind intensification and stratification in the Humboldt CS remains open to debate, and we speculate that the overall biological response may depend on the specific characteristics of each ecosystem. Our study focus specifically on the effects of the increase of upwelling-favorable winds that may be induced by global warming. Other modeling studies are necessary to address not only the isolated impacts of winds or heat fluxes on PP but also on how the inherently coupled ocean-atmosphere system and its associated feedbacks will impact ocean biogeochemistry.

Chapter VII

Mechanisms and drivers of pCO_2 and associated CO_2 fluxes

1 Spatiotemporal variability of air-sea CO_2 fluxes

The annual mean pattern of air-sea CO_2 fluxes is shown in Fig. VII.1-a. The annual means of two terms involved in their computation (see Eq. 3), namely the CO_2 transfer velocity (k_w) and the CO_2 solubility (K_0) are also shown in Fig. VII.1-b,c. The dependence of k_w on the wind makes the two fields relatively similar, with larger values close to the anticylonic subtropical gyre and lower ones along the Peruvian coast (i.e. wind drop-off zone). In addition, k_w exhibits a contrasting coastal latitudinal gradient. For instance, around Chiclayo (7°S) a minimum of 7.6 cm hr^{-1} is obtained, while at the southern domain around Pisco (14°S), a maximum of 12.8 cm hr^{-1} is found. This results in a relatively large CO_2 exchange efficiency in the southern coastal region. Given the inverse relationship between temperature and K_0, larger values are found in the upwelling coastal region and lower values of K_0, at the northern part of the

domain near the equatorial band, which is characterized by warmer surface waters (Fig. VII.1-c). The source-sink threshold, i.e. the zero-crossing line depicted in Fig. VII.1-a as a solid black line, has been reported to occur between 21°S and 27°S (Torres et al., 1999, 2003). Our simulations show that this source-sink threshold is located along the Chilean coastal domain (not shown). In the northern boundary of the regional domain the crossing limit reaches the Equatorian coast, which agrees with observed pCO_2 measurements shown in Fig. V.6. The NHCS as a whole is commonly thought to be a wide CO_2 outgassing region, however, it seems to be surrounded by two crossover regions, one around the geographical border between Peru and Ecuador ($\sim$3°S), and another one around the Tropic of Capricorn at the south ($\sim$26°S) (not shown). Hence, regional differences are important when estimating the carbon budget.

Fig. VII.1-d shows time series of all terms involved in the air-sea CO_2 flux computation, showing that they follow the upwelling intensity throughout the year, with a minimum during Summer and a maximum during Winter. Seawater pCO_2 and associated air-sea CO_2 fluxes are highly correlated both temporally and spatially. During Winter, when the winds are significatively enhanced, seawater pCO_2 increases which, in turn, induce an increase in the air-sea CO_2 flux, leading to a stronger source nature of the region. The regional domain has a similar temporal variability as the nearshore domain with different amplitudes (not shown). The amplitude of the air-sea CO_2 fluxes, pCO_2, and K_0 are, on average, 3.7 mol C m^{-2} yr^{-1}, 130 μatm, and 0.0025 mol Kg^{-1} atm^{-1} smaller than the corresponding average amplitude of the nearshore domain. However, k_w is, on average, 2.4 cm hr^{-1} faster than in the regional domain.

For comparison, Takahashi et al. (2009) estimated a large CO_2 source along the

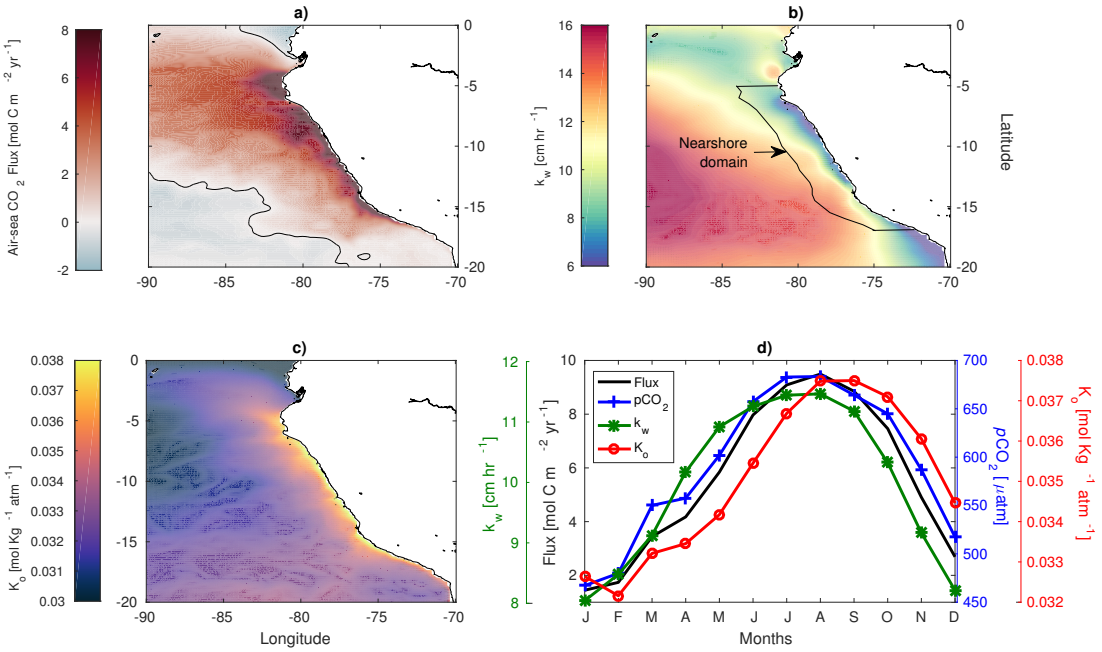

Figure VII.1: a) Annual mean air-sea CO_2 flux. The solid black line denotes the zero value, i.e, the contour where seawater pCO_2 equals the atmospheric value (397 μatm). b) Annual mean gas transfer velocity (k_w). The 300-km wide coastal band, or nearshore domain, is depicted. c) Annual mean CO_2 solubility (K_0). d) Monthly times series of air-sea CO_2 fluxes, seawater pCO_2, k_w, and K_0 for the nearshore domain.

equatorial Pacific, from 14°N to 14°S over an area of 86.7 $\times$ 10^6 Km^2, to be $+0.48$ Pg C yr^{-1}. In this study, the outgassing flux of carbon was estimated to be $+0.07$ Pg C yr^{-1} over an area of 5 $\times$ 10^6 Km^2 (regional domain), which represents less than 6% of the entire area of the equatorial Pacific. However, this relatively small area contributes to, approximately, 15% the total outgassing flux of carbon of the equatorial Pacific, rendering the NHCS a key region for the global atmospheric carbon budget.

The sensitivity model simulations allow the separation of the individual contributions of each mechanism to the total air-sea CO_2 fluxes. As seen in Fig. VII.2-a, the source nature of the nearshore domain results primarily from circulation. However,

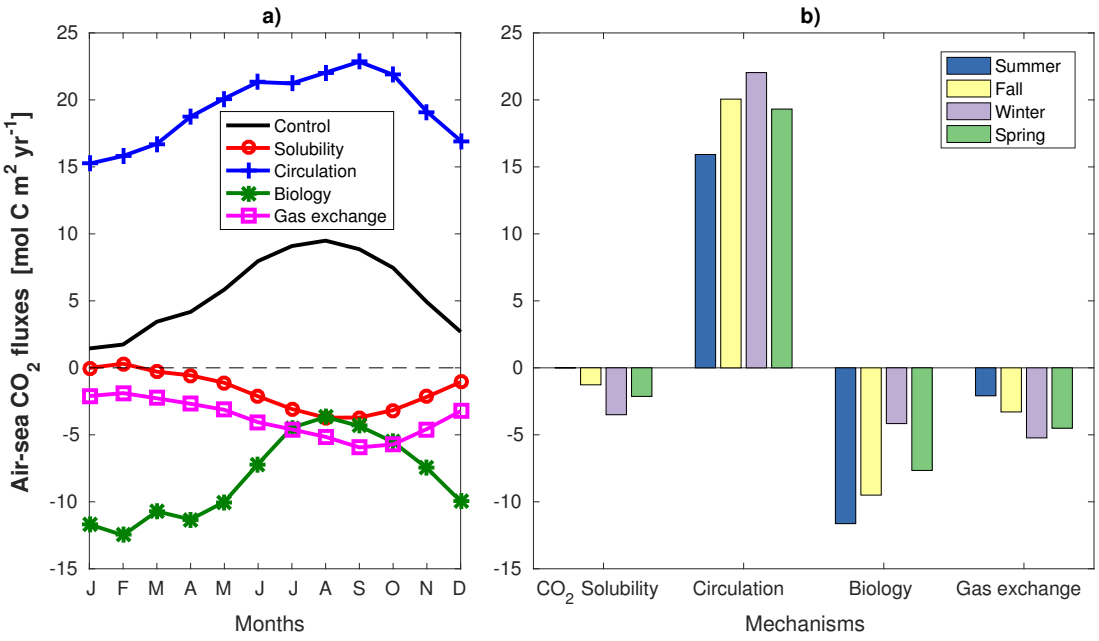

Figure VII.2: a) Monthly times series of the contribution of each mechanism to total air-sea CO_2 fluxes for the nearshore domain. The dashed black line denotes the zero value. b) Seasonal mean contributions for each mechanism are shown as colored bars (Summer (JFM), Fall (AMJ), Winter (JAS) and Spring (OND)).

the seasonal variability of the mechanisms modulate the strength of the outgassing. During Summer, biological productivity and gas exchange nearly cancel the effect of circulation, rendering the region a weak CO_2 source. In the wintertime, the stronger source nature of CO_2 is a result of a more intricate balance between the mechanisms. The increase in the winds leads to a decrease of biological productivity and an increase of gas exchange. At the same time, low SST increases the effect of solubility. However, these mechanisms are not able to keep up with the increase of circulation in the wintertime. On average, circulation contributes with a CO_2 outgassing of, approximately, 19 mol C m^{-2} yr^{-1}, while the other mechanisms contribute with an uptake of 13 mol C m^{-2} yr^{-1}. The seasonal mean contributions of each mechanism are shown as colored bars in Fig. VII.2-b. A more robust assessment on the drivers

and mechanisms behind this source nature is performed in next sections but focusing on seawater pCO_2 variations rather than on CO_2 fluxes. This is because the sign of the air-sea CO_2 fluxes are solely influenced by seawater pCO_2 changes.

2 Spatial variability of annual mean pCO_2

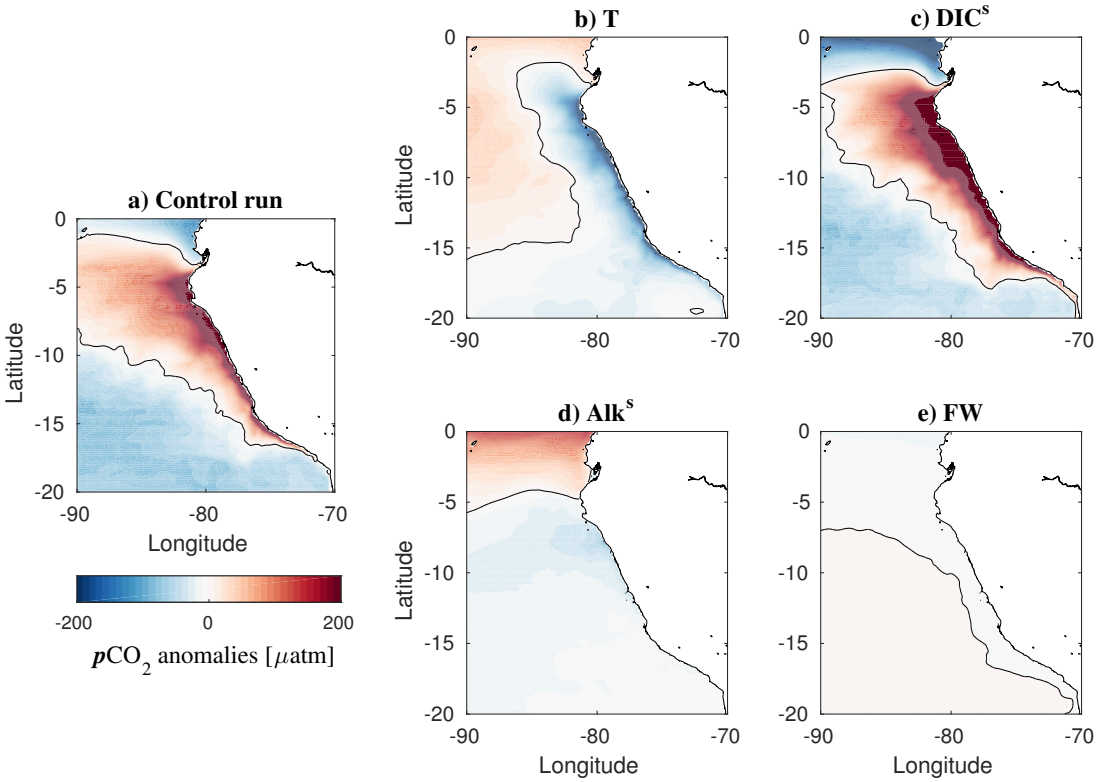

Figure VII.3: Spatial pCO_2 anomalies. (a) Total pCO_2 from the control run computed as the difference between the annual mean map and the domain mean ($\overline{pCO_2} = 461$ μatm). Panels b, c, d and e show the contributions of the four drivers (temperature (T), DIC^s, Alk^s and freshwater (FW), respectively) to the total pCO_2 anomalies.

Fig. VII.3-a shows the spatial anomalies of the annual mean pCO_2 (relative to the domain average value of $\overline{pCO_2} = 461$ μatm) for the control run. This spatial pattern is, approximately, a reconstruction between all the individual contributions of each

driver ($\Delta pCO_2^{ctrl} \simeq \sum_i^{drivers} \Delta pCO_2$), i.e, the sum of Fig. VII.3-b,c,d,e results in Fig. VII.3-a, neglecting the residuals. As the anomalies were computed based on a 20°×20° domain, it actually provides a regional scale anomaly pattern with a tongue of positive anomalies projected northwestward from the coast. Negative anomalies characterize the oligotrophic oceanic area in the southern domain and along the equatorial band. This pattern (Fig. VII.3-a) is a result of strong spatial gradients in DIC^s and temperature (Fig. VII.3-b,c). The temperature-driven pCO_2 anomalies distinguish the cold and highly productive coastal upwelling band (with negative anomalies) and the adjacent oligotrophic ocean with relatively warmer waters (with positive anomalies). For comparison, Turi et al. (2014) found that the most important variables in controlling the spatial variability of pCO_2 in the California EBUS are DIC^s and temperature, in agreement with other global and regional studies (Lovenduski et al., 2007; Doney et al., 2009; Signorini et al., 2013; Ishii et al., 2014; Arruda et al., 2015).

The influence of Alk^s is minor when compared to DIC^s, particularly in the coastal area where it is an order of magnitude smaller (Fig. VII.3-d). Turi et al. (2014) found an important role of Alk^s in controlling pCO_2 in the Southern California Bight. Arruda et al. (2015) found a potentially large impact of Alk^s in the South Brazilian Shelf and in the southern ocean region as well. They suggested that the elevated Alk^s contribution could be associated to heterogeneous regions with several distinct surface water masses and frontal zones. In our case, Alk^s becomes important in the northern part of the domain (positive pCO_2 anomalies northward of $\sim 5°S$ in Fig. VII.3-d). Given the linear relationship between Alk and salinity, the decrease in surface Alk, up to 10% the domain mean, is attributed to the low salinities associated to different types of water masses, such as the tropical and equatorial surface waters in

the northern portion of the regional domain (Graco et al., 2007). Although we did not explicitly include river discharges in our simulations, the signal of associated low salinities (runoff influence) is represented in our solutions through the climatological surface and lateral forcings. The impact of FW may be neglected (Fig. VII.3-e). Note that, a negative pCO_2 anomaly does not translate into a sink nature of CO_2. This is because the domain-average pCO_2 ($\overline{pCO_2}$) is 64 μatm above pCO_2^{air}. Thus, neither Alk nor FW, have the potential by themselves to reduce seawater pCO_2 below atmospheric levels from a regional scale perspective. In the nearshore domain, DIC contributes with, approximately, +250 μatm to the total pCO_2 anomalies. Meanwhile, T, Alk and FW tend to cancel the DIC effect out, reducing the domain-average pCO_2 in, approximately, -97, -22 and -1.7 μatm, respectively. This suggests that the effect of larger DIC concentrations in increasing pCO_2 is up to three times larger than the effect of low SST in decreasing seawater pCO_2.

In order to assess the contribution of the mechanisms behind the spatial gradient of the annual mean pCO_2, we now look at the results of the sensitivity experiments, which are summarized in Fig. VII.4. Note that, instead of showing the spatial anomalies of pCO_2 due to the drivers as presented in Fig. VII.3, here we show the spatial net contribution of each mechanism to total pCO_2 ($pCO_2^{ctrl} = \sum_i^{mechanisms} pCO_2$), i.e. the sum of Fig. VII.4-b,c,d,e results in Fig. VII.4-a (residuals $\mathcal{O}(10^{-13})$). If pCO_2 was solely controlled by the circulation (physics), a pattern similar to Fig. VII.4-b would be observed. On average, seawater pCO_2 reaches values up to +874 μatm due to circulation alone, i.e. the physical transport and mixing of DIC and Alk. The contribution of biology (Fig. VII.4-c) is negative nearly everywhere and its average value is -337 μatm. This biologically-driven pCO_2 drawdown turns out to be higher

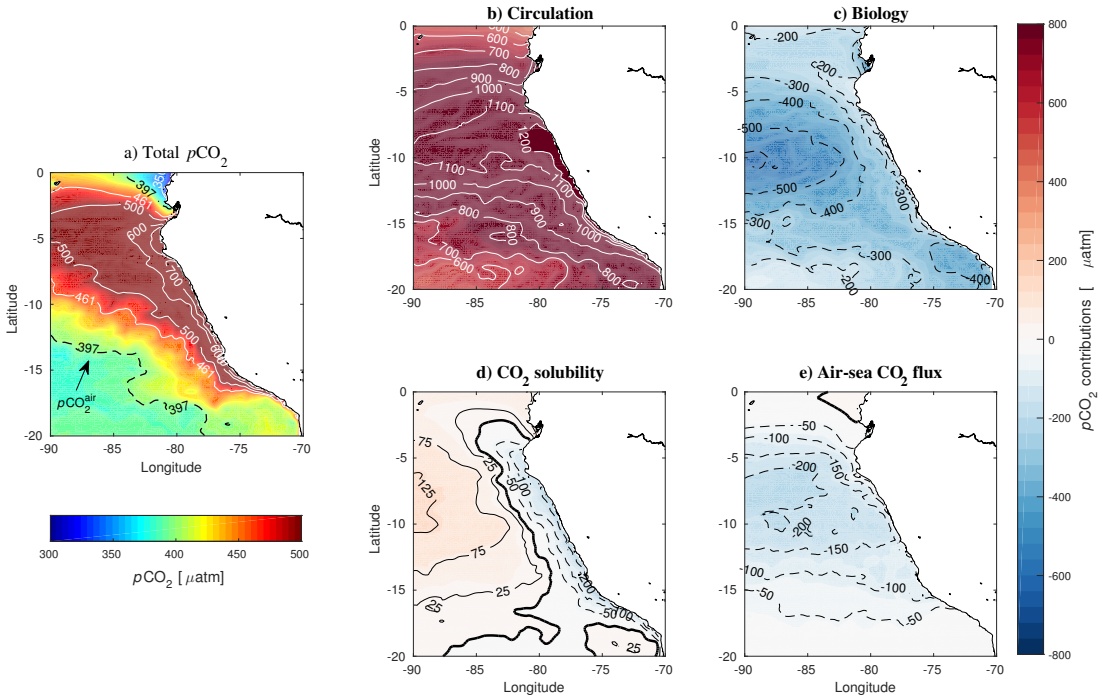

Figure VII.4: (a) Total annual mean pCO_2 for the low resolution control run. Individual contributions to the total pCO_2 for (b) ocean circulation; (c) biology; (d) CO_2 solubility and (e) air-sea CO_2 fluxes. Solid black line depicts the zero value.

further offshore and also within the coastal band south of 17°S. The spatial decoupling between the area of maximum upwelling and regions where the biological effect is maximum, as shown in Fig. VII.4-c may be attributed to i) the upward transport and mixing of DIC and nutrients that are biologically taken up and subsequently exported as organic matter (Sarmiento e Gruber, 2006), ii) incomplete utilization of upwelled macro nutrients (Friederich et al., 2008), because nitrate is not efficiently used due to iron limitation (Gruber et al., 2009), iii) high levels of mesoscale activity that export nutrients offshore (Gruber et al., 2011) where the full potential of biological drawdown of CO_2 is achieved (Lachkar e Gruber, 2011, 2013; Turi et al., 2014). As a consequence, the air-sea CO_2 fluxes are not spatially balanced in the NHCS because the nutrient limitation turn out to be high with a relatively low nutrient

use efficiency, particularly in some important upwelling centers along the Peruvian coast (Mogollón e Calil, 2018a). This low degree of biological compensation implies a sluggish biological pump in the upwelling region of the NHCS, which in turns explains the high pCO_2 values found in the 100 km-wide coastal strip and the associated strong CO_2 outgassing. In contrast, Turi et al. (2014) explains that the air-sea CO_2 fluxes in the California Current System are essentially balanced due to the highly efficient biological pump in the region, i.e. a net release of CO_2 in the nearshore band is largely compensated by a net biologically-driven uptake of CO_2 in the offshore region.

The contribution of the processes affecting CO_2 solubility (Fig. VII.4-d) closely resembles that of temperature (see Fig. VII.3-b). This is because of the stronger dependence of CO_2 solubility on SST than on salinity. The solubility-driven contribution accounts, on average, for $+19$ μatm. The contribution of the air-sea CO_2 flux is negative in the central part of the domain in the NHCS (see Fig. VII.4-e), evidencing a negative contribution of the gas exchange to total seawater pCO_2, i.e., total DIC loss through outgassing. On average, the air-sea CO_2 fluxes contribute to a decrease of seawater pCO_2 of, approximately, -95 μatm. Note that the spatial gradient of air-sea CO_2 flux resembles the annual mean pCO_2 pattern (Fig. VII.3-a), since it is directly tied to regions where the NHCS acts as a source or sink of atmospheric CO_2.

3 Temporal variability of domain mean pCO_2

Here we focus on the temporal variability of pCO_2 by investigating the drivers and mechanisms on monthly and seasonal time scales. To this end, we consider a domain-average of each driver or mechanism. The decomposition of the pCO_2 anomalies into

individual contributions for both drivers and mechanisms was applied once for the regional domain. The temporal variability for the regional domain and for a subset (nearshore domain) was analyzed separately. Additional estimates of the net contribution of each mechanism to the total pCO_2, instead of pCO_2 anomalies, is also presented for both domains and on seasonal time scales (see Table VII.1).

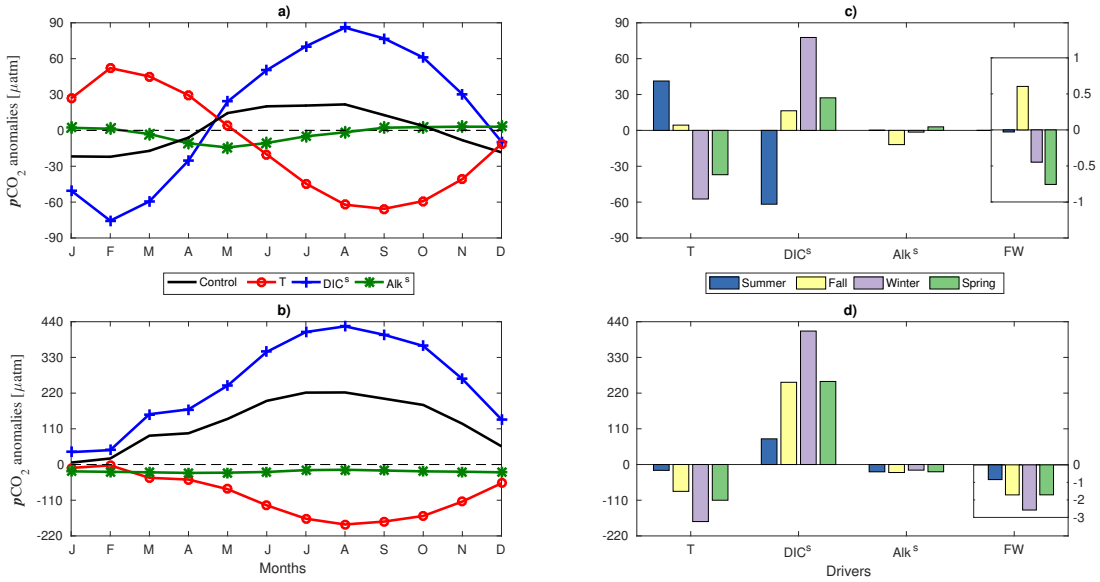

Figure VII.5: Monthly mean contributions of the four drivers (temperature (T), DIC^s, Alk^s and FW) to total pCO_2 anomalies for (a) the regional domain and for (b) the nearshore domain. Solid black line represents the pCO_2 anomaly from the control run, computed as the difference between the monthly time series and the annual mean value of the regional domain ($\overline{pCO_2} = 461$ μatm). The seasonal mean contributions for each driver are shown as colored bars (Summer (JFM), Fall (AMJ), Winter (JAS) and Spring (OND) for (c) the regional domain and for (d) the nearshore domain. In panels c,d the contribution of FW was adjusted for visualization purpose since its contribution is negligible.

Fig. VII.5-a,b shows the monthly mean contributions of the four drivers to the total pCO_2 anomalies for the regional and nearshore domain, respectively. The associated seasonal contribution is also presented as a bar diagram in Fig. VII.5-c,d. DIC^s and

T are the most important drivers in both domains, exhibiting larger amplitudes and they both tend to cancel each other out along the year. Specifically, for the regional domain, the pCO_2 variations driven by DIC^s tend to diminish and increase pCO_2 during the first and second half of the year, respectively. The temperature-driven variations follow the seasonal cycle of warming and cooling, exhibiting an opposite seasonality to DIC^s. This is more evident in the bar diagram where each driver is highlighted with its seasonal contribution (Fig. VII.5-c). In the nearshore domain (Fig. VII.5-b), the purely DIC-driven pCO_2 anomalies follow the seasonal cycle of the upwelling intensity. These DIC^s-driven pCO_2 variations are always large (+250 μatm, on average), particularly during Winter (+400 μatm). In contrast, persistently low SST during all seasons in the upwelling region induces a decrease in pCO_2 of, approximately, -96 μatm, with a maximum during Winter (-176 μatm) and a minimum during late Spring-Summer (-24 μatm). Overall, pCO_2 is more sensitive to changes in DIC than SST in a proportion varying from 2:1 to 4:1 depending on the season (Fig. VII.5-d). The seasonal cycle of the Alk^s-driven component has a minor influence on the simulated pCO_2 for both regions. Within the regional domain, Alk^s appears to be phase-lagged by about 2 months with DIC^s or T, exhibiting a minimum (negative anomalies) during Fall and a maximum (positive anomalies) during Spring. This phase shift occurs because alkalinity follows the seasonal cycle of salinity, which is also 2 months out of phase with SST on a regional scale. In contrast, in the nearshore domain, Alk^s-driven variations induce a yearlong decrease in pCO_2 of, approximately, -22 μatm. pCO_2 variations driven by FW may be neglected for both domains (not shown), as in the case of the spatial analysis.

In order to quantify the role of each mechanism in controlling the temporal pCO_2

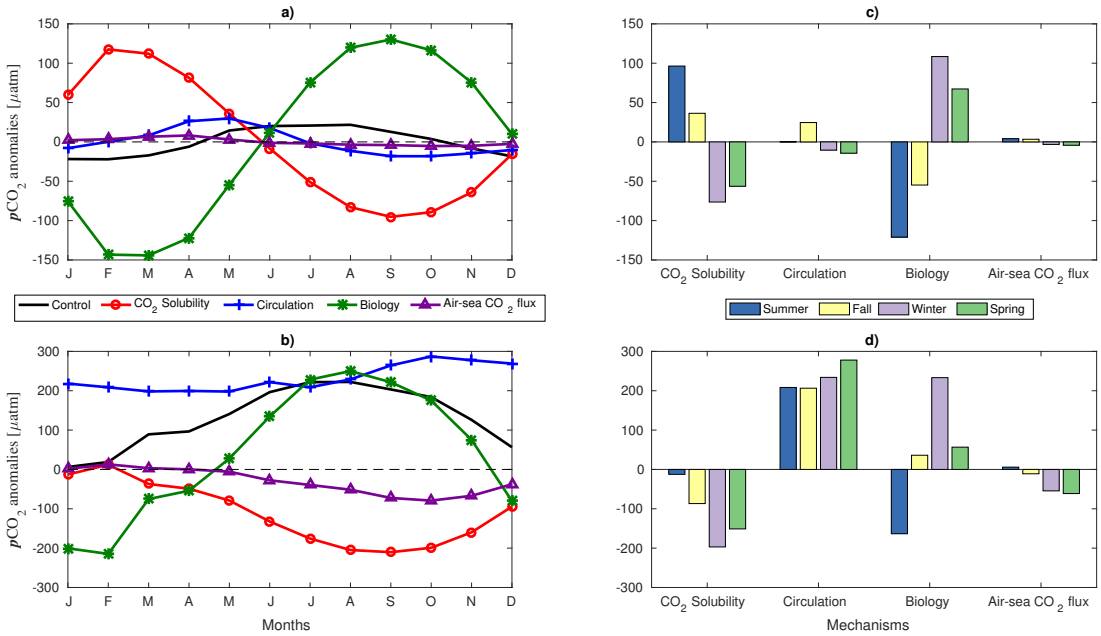

Figure VII.6: Monthly mean contributions of the four mechanisms (CO_2 solubility, circulation, biology and air-sea CO_2 flux) to total pCO_2 anomalies for (a) the regional domain and for (b) the nearshore domain. Solid black line represents the pCO_2 anomaly from the control run, computed as the difference between the monthly time series and the annual mean value of the regional domain ($\overline{pCO_2}$ = 461 μatm). For consistency, panels-a,b show the fluctuations of CO_2 solubility, circulation, biology and air-sea CO_2 flux around 19, 874, -337 and -95 μatm, respectively. The seasonal mean contributions for each mechanism are shown as colored bars (Summer (JFM), Fall (AMJ), Winter (JAS) and Spring (OND)) for (c) the regional domain and for (d) the nearshore domain.

variability, Fig. VII.6-a,b shows the temporal fluctuations around 19, 874, -337, -95 and 461 μatm for CO_2 solubility, circulation, biology, air-sea CO_2 flux and control pCO_2, respectively. By doing so, the sum of all individual contributions of the four mechanisms to the pCO_2 anomalies, i.e. the solid black lines (control), are the same as in Fig. VII.5 and Fig. VII.6. Biologically-driven pCO_2 variations follow the so-called "paradoxical cycle"of the surface chlorophyll (Pennington et al., 2006; Echevin et al., 2008b), which is inversely proportional to the intensity of the upwelling. Thus, despite the increased upwelling during Winter, the NHCS becomes less productive (Mogollón

e Calil, 2018a). In contrast, biological production is enhanced during Summer-Fall, leading to a stronger biological compensation for both domains. For the regional domain (Fig. VII.6-a,c), CO_2 solubility follows the seasonal annual cycle of warming and cooling as it is strongly influenced by changes in temperature. The seasonal variations in circulation contribute to a lesser degree to the seasonal pCO_2 variability while the contribution from the air-sea CO_2 fluxes is negligible. However, for the nearshore domain (see Fig. VII.6-b,d), circulation clearly dominates. The seasonal variations in CO_2 solubility due to persistently low SST play an important role on dampening the effect of circulation in all seasons. However, based on our simulations, this thermal solubility compensation accounts for, approximately, half of the circulation effect. This is consistent with the compensating effect between DIC^s and T, as observed in the analysis of the drivers. Seasonal variations in air-sea CO_2 fluxes act reducing the overall amplitude of the seasonal pCO_2 variability but with a smaller contribution than the other three mechanisms (Fig. VII.6-d). Finally, if we sum each individual net contribution from all the mechanisms acting on pCO_2 within the nearshore domain, the resulting seawater pCO_2 will be 100 to 280 μatm larger than atmospheric values depending on the season of the year. This positive difference (pCO_2^{sea} - $pCO_2^{\text{air}} > 0$) is the reason why the highly productive upwelling region of the NHCS is a source of atmospheric CO_2.

Table VII.1: Seasonal net contribution of each mechanism to the total pCO_2 in μatm. Values outside the parentheses are for the regional domain, while the ones in parentheses, for the nearshore domain. The negative sign means that a mechanism is contributing in a negative sense to seawater pCO_2, i.e., inducing a decrease. The last row, namely "Total", is the sum of the four mechanisms above (also referred to as Control).

Mechanism/Season	**Sumer**	**Fall**	**Winter**	**Spring**	**Annual mean**
Circulation	874 (1082)	898 (1080)	863 (1108)	859 (1152)	874 (1105)
CO_2 solubility	115 (6)	55 (-68)	-58 (-178)	-38 (-132)	19 (-93)
Biology	-458 (-500)	-391 (-301)	-228 (-104)	-269 (-280)	-337 (-296)
Air-sea CO_2 flux	-90 (-89)	-91 (-106)	-98 (-149)	-99 (-156)	-95 (-125)
Total	441 (499)	471 (605)	479 (677)	453 (584)	461 (591)

Chapter VIII

ENSO-driven CO_2 efflux variability

1 ENSO composites

Fig.VIII.1 shows the anomalies, respect to the climatological mean, of SST (panels a-c), wind velocity (panels d-f) and DIC (panels g-i) under an average El Niño and La Niña episode. Positive SST anomalies indicate warming and negative ones, a cooling (see Fig.VIII.1a-c). This is well known due to advection of warm waters from the Equatorial Current System toward the Peruvian coast during El Niño events. Less well known is the fact that upwelling-favorable wind off Peru increases rather than decreases during an average El Niño episode, as seen in Fig.VIII.1d-f. This is paradoxical due to the expected weakening of the large-scale Pacific Trade winds during the warm phase of ENSO (Oort e Yienger, 1996). One reasonable explanation is related to the Bakun's upwelling intensification hypothesis (Bakun, 1990), which stated that the increase in anthropogenic greenhouse gases, such as CO_2 or water vapor (ETP becomes moister during El Niño events), would lead to the increase of the land-sea thermal gradient along the Peruvian coast, thus, inducing a strengthening

of the upwelling-favorable local winds (Bakun e Weeks, 2008; Bakun et al., 2010). However, recent studies suggest that is not likely to occur in the NHCS. For instance, Belmadani et al. (2014) found that a 40% increase of the land-sea thermal gradient represents a 10% alongshore wind decay, also associated with a poleward displacement of the South Pacific Anticyclone, in a climate change context. Chamorro et al. (2018) found that the increase in humidity did not support the Bakun's strengthened land-sea thermal contrast. Instead, they suggest that the coastal wind intensification during El Niño 1997-1998 was mainly driven by the enhancement of the SST-driven alongshore pressure gradient. While the mechanisms behind the wind intensification are still open to debate, is clear that during an average El Niño episode the wind speed in the central domain of the NHCS increases more than 1 ms^{-1} with an upwelling-favorable direction (Fig.VIII.1e). This is in agreement with Fig.1 in Chamorro et al. (2018), which shows positive alongshore (equatorward) wind anomalies southern 5°S. In contrast, the wind anomalies during an average La Niña episode (Fig.VIII.1f) exhibit an opposite spatial pattern than during El Niño. Positive anomalies are found in the southern oceanic domain associated with the strengthening of the South Pacific subtropical Anticyclone gyre. However, a decrease in the wind speed with an upwelling-unfavorable direction is evidenced by negative anomalies in the central NHCS. This weakening of the wind is about half the strengthening during El Niño conditions in the coastal area.

On the other hand, Mogollón e Calil (2018b) demonstrated that DIC and SST, associated with the physical circulation and thermal CO_2 solubility mechanisms, are the most important drivers of pCO_2^{sw} in the NHCS. As a consequence, anomalies of DIC (Fig.VIII.1g-i) are highly related to changes in the solubility pump. This is in agreement with Archer et al. (1996), who found that biological changes are not responsible for changing pCO_2^{sw} values in the equatorial Pacific, therefore, pCO_2^{sw} changes could be

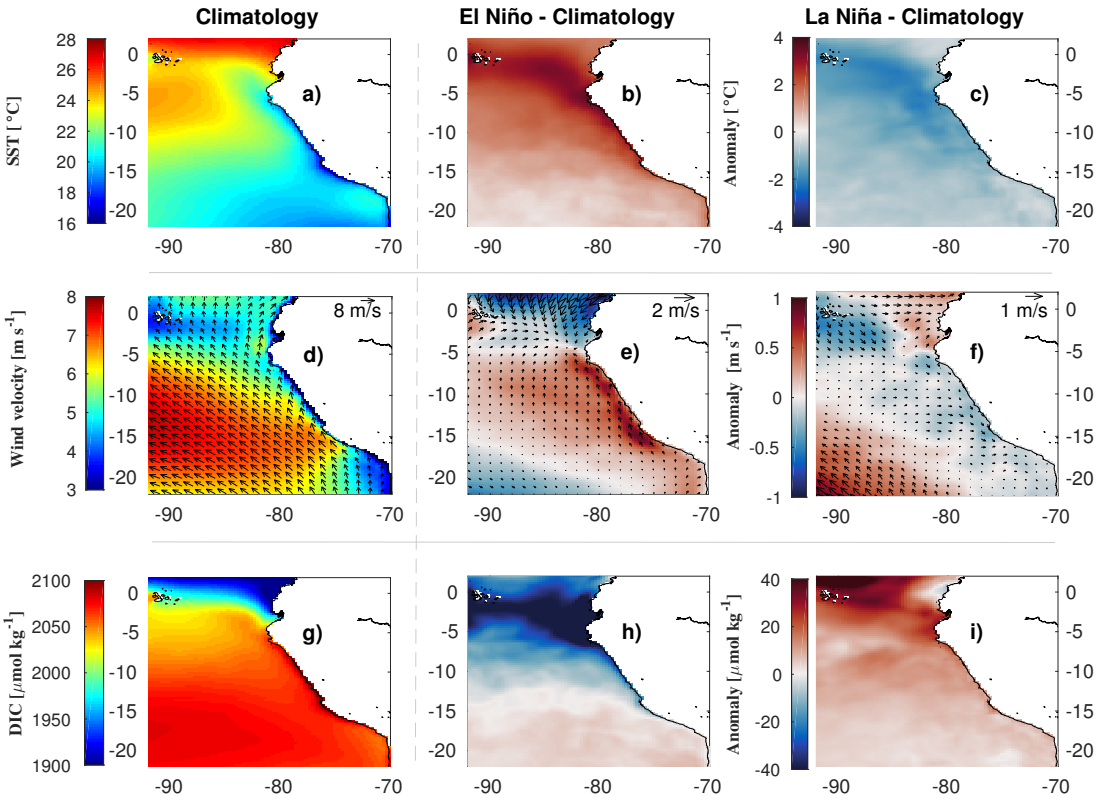

Figure VIII.1: a) Annual mean of simulated SST (climatology). b) SST anomaly during an average warm phase of ENSO (El Niño minus climatology). c) SST anomaly during an average cold phase of ENSO (La Niña minus climatology). Similarly, panels d-f and g-i are for wind velocity (CCMP V2 winds) and inferred surface DIC, respectively.

explained solely by changes in upwelled DIC, particulary during ENSO events. As the relationship between DIC and temperature is relatively linear (Sarmiento e Gruber, 2006), a warming would represent a decrease in surface DIC concentrations by reducing the solubility of CO_2. The decrease of DIC during El Niño may also be related to remotely-generated forcings, such as the Intraseasonal Equatorial Kelvin Waves and the subsequent poleward propagation of the downwelling-favorable coastal-trapped waves (CTW) which deepen the thermocline (Echevin et al., 2014b), rendering the upwelled water warm and and CO_2-depleted. A vertical displacement of the pycnocline and nutricline is also expected, modulating the vertical supply of nutrients and carbon

above the euphotic layer during the passage of the CTW. In contrast, during La Niña positive DIC anomalies are found in response to enhanced upwelling associated with an increase of CO_2 solubility. Despite the relatively slight decrease of the upwelling-favorable winds during La Niña, upwelled waters carried by the Equatorial Undercurrent and the Peru-chile Undercurrent are known to be nutrient-repleted and the position and intensity of these major upwelling sources waters are favorable when compared to El Niño conditions (Colas et al., 2008; Montes et al., 2010, 2011; Espinoza-Morriberón et al., 2017). Thus, large rates of vertical transport of inorganic carbon to the surface may explain positive DIC anomalies found under La Niña conditions. These considerations, while speculative, provide at least some degree of explanation for the ENSO-driven anomalies of surface DIC.

2 Forcing factors interannual variability

Following the methodology, results show that the large values of the root-mean-square (rms) of air-sea CO_2 flux anomalies are found in the upwelling region (depicted as a solid black line in Fig.VIII.2a) and in the central oceanic domain, i.e. the major regions of variability. Whereas that panels Fig.VIII.2b-d show the forcing factors driving the interannual variability of $\mathrm{F_{CO_2}}$. As seen, $\mathrm{F_{CO_2}}$ variability (Fig.VIII.2a) is dominated by $\Delta p\mathrm{CO_2}$-driven anomalies (Fig.VIII.2c), gas transfer velocity-driven anomalies (Fig.VIII.2b), and their cross-correlations (Fig.VIII.2d), in this order of importance. Gas transfer velocity-driven flux variability, $(K_0 k_w)' \times \overline{\Delta p\mathrm{CO_2}}$, results to be unusually high in the NHCS. This is due to the ENSO-induced large wind speed variability, together with a large $\Delta p\mathrm{CO_2}$ mean of, approximately, 60 μatm in the upwelling region (not shown). Furthermore, air-sea CO_2 flux is highly correlated to

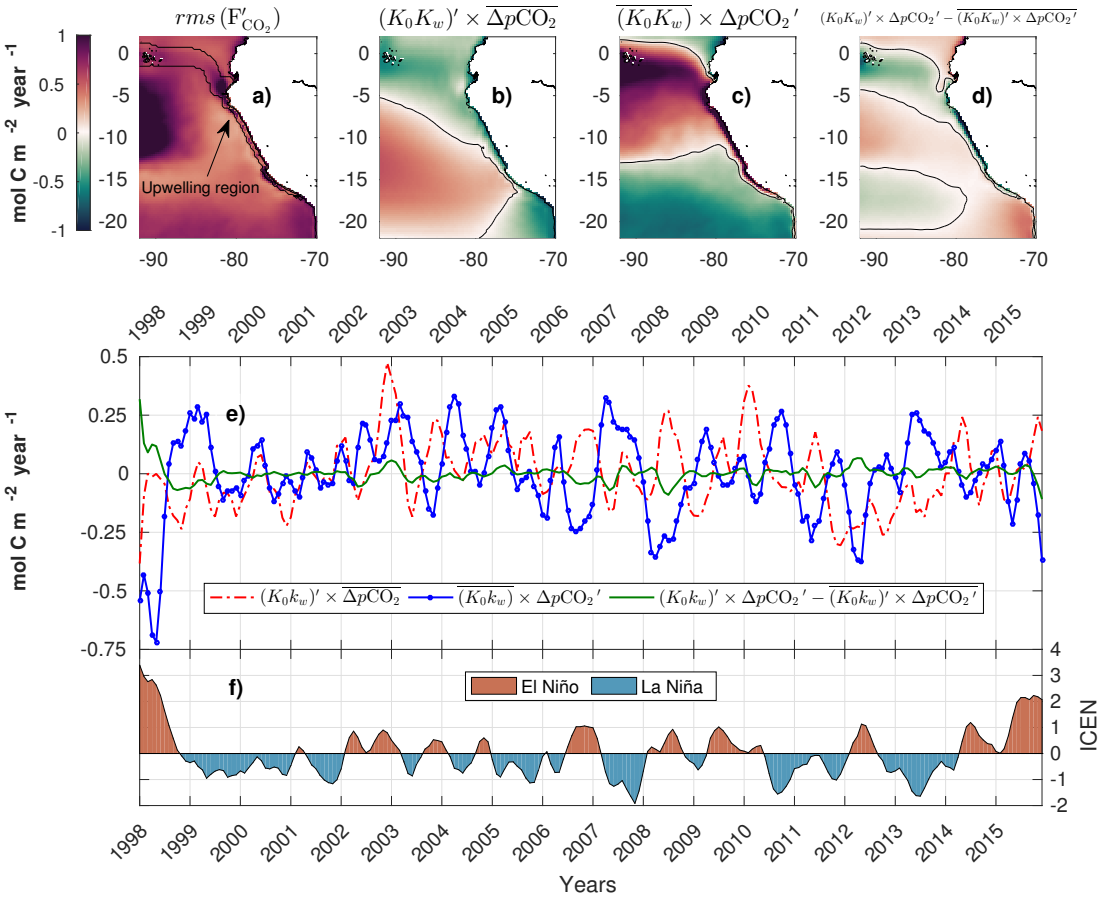

Figure VIII.2: Sensitivity of the forcing factors of air-sea CO_2 flux (F_{CO_2}) anomalies. a) root-mean-square of F_{CO_2} anomalies. Solid black line denotes the upwelling region. Contribution to the variability of F_{CO_2} from b) gas transfer anomalies, c) ΔpCO_2 anomalies, and from d) gas transfer and ΔpCO_2 anomalies cross-term. Solid black line in panels b-d depicts the zero value. e) Temporal variability of the forcing factors computed within the upwelling region. f) ENSO index: ICEN.

both gas transfer velocity and ΔpCO_2 in, approximately, 0.9 and 0.8, respectively. These findings are in agreement with a global study (Doney et al., 2009) which found that maxima rms values of F'_{CO_2} are found in the Tropical Pacific, where a noticeable contribution from gas transfer variability also occurs. Nevertheless, Jones et al. (2001) found that the sensitivity of the air–sea CO_2 flux to the gas transfer velocity is smaller than ΔpCO_2. Specifically, they found that under El Nino conditions, the majority of

the reduction in CO_2 outgassing is due to a reduction in the ΔpCO_2, with a smaller contribution from the gas transfer velocity. However, a comparable contribution from both forcing factors during El Niño conditions was found in this study, together with a strengthening of the winds rather than a weakening. This discrepancy arises because this study focuses on the upwelling region rather than from a large-scale domain perspective.

Fig.VIII.2e shows the detrended monthly time series (3-months moving average) of the forcing factors for the upwelling region. It is noticeable that the interannual variability of the air-sea CO_2 flux in this region is dominated by both the contribution of the gas transfer velocity and ΔpCO_2 anomalies. The former is related to an increase and a decrease of the wind speed ($\sim$1 ms^{-1}) during El Niño and La Niña events, respectively. The latter is mainly related to changes in pCO_2^{sw} because pCO_2^{air} varies little at the interannual timescale. ΔpCO_2 induces a negative contribution to the air-sea CO_2 fluxes during El Niño events which may be interpreted as a decrease of the CO_2 outgassing. This weaker CO_2 source behavior could be explained mainly due to the downwelling pattern that occurs during the warm phase of ENSO, leading to a substantial reduction of the carbon supply to the surface. A decrease of DIC and pCO_2^{sw} of, approximately, 36 μmol kg^{-1} and 18 μatm, respectively, was estimated for the upwelling region. Conversely, during La Niña ΔpCO_2-driven flux variability exhibits large positive amplitudes, which may be interpreted as an increase of the CO_2 outgassing. This response results from enhanced upwelling during La Niña which brings more DIC-rich waters to the surface, thus increasing pCO_2^{sw} and favoring the CO_2 degassing. An increase of DIC of, approximately, 26 μmol kg^{-1} during La Niña, with a concomitant pCO_2^{sw} increase of, approximately, 16 μatm, were estimated for

the upwelling region. The contribution from the cross-term is minor. However, it becomes more significant during El Niño peaks than La Niña ones.

The difference between the contribution to the interannual air-sea CO_2 anomalies from the gas transfer velocity and ΔpCO_2 anomalies, i.e. dash-dotted red line minus blue dotted line in Fig.VIII.2e, is correlated (0.62) with the ICEN (Fig.VIII.2f). Furthermore, this correlation may be higher ($\sim$ 0.7) when using other ENSO index, such as the Coastal Laboratories Thermal Index (LABCOS) (Quispe e Vásquez Espinoza, 2015). This high correlation permits identify some general aspects associated with ENSO events within the upwelling region: i) during an average El Niño episode, gas transfer anomalies tend to increase the air-sea CO_2 flux, while ΔpCO_2 anomalies tend to diminish it; ii) during an average La Niña episode, gas transfer anomalies tend to decrease the air-sea CO_2 flux, while ΔpCO_2 anomalies tend to increase it. These generalizations should be considered with caution because each El Niño and La Niña event has unique characteristics of timing and intensity and they are never exactly the same. For instance, during the strongest El Niño 1998, ΔpCO_2-driven anomalies are still in phase opposition to the gas transfer-driven anomalies, yet the latter contributes negatively to the CO_2 flux variability.

3 Integrated carbon flux

From inferred air-sea CO_2 fluxes, the spatially integrated evasion flux of carbon in Tg C year^{-1} was calculated. This computation was performed over the upwelling region, an area of 3.7×10^5 km^2. Under climatological conditions, the integrated carbon flux was calculated in, approximately, 5 Tg C year^{-1}. This value is within the same order

of magnitude based on previously observed and modeling studies (Friederich et al., 2008; Mogollón e Calil, 2018b). During an average El Niño and La Niña episode, the integrated carbon flux was estimated in, approximately, 4.5 and 6 Tg C year^{-1}, respectively. However, these fluxes may be larger depending on the temporal scale. For example, during the strongest La Niña-2007, more than 10 Tg C year^{-1} was obtained. To put in context, this value equals to a tenth of the coastal uptake of anthropogenic carbon globally (Bourgeois et al., 2016), therefore, the upwelling region of the NHCS is indeed a key region for the global atmospheric carbon budget. Considering a one-year period as the duration of an average ENSO episode, the upwelling region contributes to the evasion flux of carbon with 1 Tg C more during La Niña, when compared to neutral (climatological) conditions. In contrast, El Niño represents a period when the upwelling region contributes to a lesser degree to the outgassing, emitting to the atmosphere 0.5 Tg C less when compared to neutral conditions.

Chapter IX

Conclusions

It is found that regions with high initial nutrient limitation, or low initial NL values (such as the counterintuitive zones), do not significantly increase their limitation status under an increased winds scenario. Moreover, the northern domain, which is characterized by higher NL, substantially increased its limitation status under increased winds scenario. As a consequence, our findings suggest that the counterintuitive zones are the most resilient (in terms of the biological response) to the global warming-induced upwelling intensification. The highest GR are found in the southern and central portion of the domain suggesting that nutrients are being more efficiently used in these regions, particularly within the counterintuitive zones, than over the northern domain, thus, explaining the latitudinal variability of the primary production. Our results show a moderate increase in primary production and suggest that its spatiotemporal variability is a result of a delicate interplay between nutrient availability and nutrient use efficiency. This is reflected in the opposite relationship between NL and GR which tend to balance each other out. Our work consisted in a single factor tuning methodology (modern and increased winds scenarios), which focus specifically on the effects of the

increase of upwelling-favorable winds that may be induced by global warming. Other modeling studies are necessary to address not only the isolated impacts of winds or heat fluxes on PP but also on how the inherently coupled ocean-atmosphere system and its associated feedbacks will impact ocean biogeochemistry.

In regard to the CO_2-carbonate system, our results demonstrate the strong source nature of the region with an averaged flux of 1.91 $\pm$ 0.71 mol C m^{-2} yr^{-1}, which represents an integrated outgassing carbon flux of 0.07 Pg C yr^{-1} (almost 15% of the entire equatorial Pacific). This source behaviour is caused by the combination of the upwelling of DIC-rich waters and an inefficient biological pump in the Humboldt EBUS. We show that the low degree of biological compensation results from a spatial and temporal decoupling between the upward transport and mixing of DIC and the downward export of organic matter. As a consequence, the area where the full potential of the biological drawdown of CO_2 is achieved is found further offshore which explains the high pCO_2 values found in the 100 km-wide coastal strip. The temporal decoupling is related to the so-called "paradoxical cycle"of primary production, which is opposite to the seasonal cycle of the upwelling intensity. The contribution of gas exchange and the processes affecting CO_2 solubility play a minor role when compared to the ones associated with the biological pump (circulation and biology). The sensitivity analysis demonstrated that the most important drivers are DIC^s and temperature, which exhibit opposing effects in controlling pCO_2. In the nearshore domain, the effect of larger DIC concentrations, due to coastal upwelling, in increasing pCO_2 is up to three times larger than the effect of low SST in decreasing seawater pCO_2. Alk^s-driven pCO_2 variations could be neglected since their contribution is one order of magnitude smaller than that of DIC^s. Similarly, the impact of FW is negligible. We

found that the solubility-driven pCO_2 variations associated with the seasonal warming and cooling of surface waters are nearly fully compensated by biology-driven pCO_2 variations in the regional domain. However, in the nearshore domain, circulation contributes most to the seasonal pCO_2 variability.

Despite the importance of the NHCS, measurements of pCO_2 along the Peruvian coast are still rare. This precludes a detailed analysis of a number of processes that affect pCO_2 variability, such as the rapid sea surface warming and the iron limitation of primary production (Chavez et al., 2007; Friederich et al., 2008). In addition, the lack of high frequency pCO_2 observations does not allow a characterization of the short-term variability of the CO_2-carbonate system which remains open to debate. This is further complicated by the highly variable ocean circulation, high levels of mesoscale activity and interannual to interdecadal variability (Feely et al., 2006; Landschützer et al., 2014). For instance, ENSO contributes to the seawater pCO_2 variability by inducing changes in the thermocline depth, wind patterns and, consequently, upwelling rates (Feely et al., 1999; Chavez et al., 1999; Wanninkhof et al., 2013; Rödenbeck et al., 2014). Although we made substantial progress in elucidating the most important contributors to seawater pCO_2 variability, our simulations did not contain nonseasonal variability. That is why we conducted a parallel experiment which consisted in reconstruct the interannual pCO_2 variability and associated fluxes in order to have an insight with regards the ENSO-driven carbon emittance. It is found that the air-sea CO_2 flux variability in the upwelling region results from combined ENSO-related ΔpCO_2 and wind speed variations. In general, during an average El Niño episode, gas transfer velocity anomalies tend to increase the air-sea CO_2 flux, while ΔpCO_2 anomalies tend to diminish it. Conversely, during an average La Niña

episode, variations in gas transfer velocity tend to decrease the air-sea CO_2 flux, while ΔpCO_2 anomalies tend to increase it. The weaker CO_2 source behavior during El Niño conditions could be explained mainly due to variations in the underlying mechanisms that directly impact DIC concentrations, consequently pCO_2^{sw}, and the efficiency of the CO_2 exchange across the air-sea interface. As such, the downwelling-like pattern induced during El Niño peaks renders the upwelled water warm and DIC-depleted. This reduction in the upward carbon supply is compensated by more efficient gas exchange at the air-sea interface due to the strengthening of the winds. In contrast, the strong CO_2 source behavior during La Niña conditions results from enhanced upwelling which brings colder and CO_2-repleted waters to the surface, thus increasing pCO_2^{sw} and associated CO_2 efflux. On the other hand, the spatially-integrated CO_2 flux was calculated over the upwelling region. In summary, based on the model assumptions and approach, during El Niño the total amount of carbon retained in the most productive region in the NHCS is about half a million tons of carbon that normally would have been lost to the atmosphere as CO_2. During La Niña, one million tons of carbon is additionally released from the upwelling region, thus contributing to the atmospheric CO_2 accumulation. Despite the similarities between different El Niño/La Niña episodes of different strengths throughout the analysis period, each ENSO event has their own characteristics, hence, generalizations here presented are mean to be to describe the average response of the NHCS to both ENSO phases. An important caveat is also related to the inferred CO_2-carbonate variables because they are limited by the model's ability to simulate the ENSO phenomenon. In addition, the anthropogenically driven increase of atmospheric CO_2 was not fully separated from inferred CO_2 fluxes, and their associated anomalies still contain the combined natural and anthropogenic variability. Another disadvantage of the approach is that it

is assumed that the ocean carbon cycle is in steady state in face of changing climate and ocean chemistry. Furthermore, complex positive and negative feedbacks between simulated ocean physics and biology may largely impact pCO_2 over multidecadal time scales, therefore, even though the CO_2-carbonate model has realistic sensitivity to ENSO, the variability of the CO_2 fluxes could be biased. In spite of these caveats and within the framework of the model assumptions, results obtained in this study are considered robust and may help to predict how the NHCS will react during ENSO events and probably in a climate change context. Further studies are still needed in order to understand the complete response of the carbonate system throughout an ENSO event in the Humboldt EBUS, as such, a sensitivity analysis of the drivers and the mechanisms behind the ENSO-driven spatiotemporal variability of pCO_2^{sw} would be highly desirable. This could be addressed in a future work.

Chapter X

Final considerations

We reject the hypothesis (see Section II) related to the biological response in face of the global warming-induced strengthening of the upwelling circulation, which says that the increase on primary production would be proportional to the magnitude of the wind intensification. It is shown that instead of a proportional enhancement in primary production due to increased winds ($\sim 40\%$ larger), the NHCS becomes only 5% more productive ($+5$ mol C m^{-2} yr^{-1}) when compared to a climatological modern winds scenario, which makes it more resilient in the face of contemporary climate change effects. As demonstrated, the NHCS behaves as a strong CO_2 source rather than a sink in spite of high levels of biological production. Furthermore, this CO_2 source nature follows the upwelling intensity throughout the year, from a climatological perspective.

We support the hypothesis (see Section II) related to the parameters that control seawater pCO_2, which are temperature and DIC. However, it is shown that the effect of larger DIC concentrations, due to coastal upwelling, in increasing pCO_2 is up to

three times larger than the effect of low SST in decreasing seawater pCO_2 within the nearshore domain. In regard to the mechanisms behind the spatiotemporal variability of seawater pCO_2 and associated air-sea CO_2 fluxes, we show that the high nearshore pCO_2 values is primarily the result of coastal upwelling, which is incompletely compensated by biology. This relatively low degree of biological compensation results from a spatiotemporal decoupling. This is, the area where the full potential of the biological drawdown of CO_2 is achieved is found further offshore which explains the high pCO_2 values found in the 100 km-wide coastal strip. The temporal decoupling is related to the so-called "paradoxical cycle"of primary production, which is opposite to the seasonal cycle of the upwelling intensity, rendering the biological component less efficient when the physical component becomes stronger. As a consequence, the hypothesis related to the fact that biology do not keep up with the additional supply of upwelling-driven DIC (see Section II) is partially supported.

The non-seasonal variability on the emittance of the air-sea CO_2 fluxes showed a negative (positive) anomaly on the source behavior in the upwelling region during an average El Niño (La Niña) episode. Thus, our results supported the last hypothesis (see Section II) which says that the cold phase of ENSO, La Niña, largely contributes to the atmospheric CO_2 accumulation.

Appendices

Articles

O primeiro manuscrito, de autoria de Rodrigo Mogollón e Paulo H.R. Calil, é intitulado ***"Counterintuitive effects of global warming-induced wind patterns on primary production in the Northern Humboldt Current System"*** e foi publicado no periódico ***"Global Change Biology"*** em Abril de 2018.

[Original article]

A versão original pode ser accesada no seguinte link:

https://onlinelibrary.wiley.com/doi/full/10.1111/gcb.14171

[Supplementary information]

A informação adicional pode ser accesada no seguinte link:

https://onlinelibrary.wiley.com/action/downloadSupplement?doi=10.1111%2Fgcb.14171&file=gcb14171-sup-0001-Supinfo.pdf

O segundo manuscrito, de autoria de Rodrigo Mogollón e Paulo H.R. Calil, é intitulado ***"Modelling the mechanisms and drivers of the spatiotemporal variability of pCO_2 and air–sea CO_2 fluxes in the Northern Humboldt Current System"*** e foi publicado no periódico ***"Ocean Modelling"*** em Outubro de 2018.

[Original article]

A versão original pode ser accesada no seguinte link:

https://www.sciencedirect.com/science/article/pii/S1463500318300428

[Supplementary information]

A informação adicional pode ser accesada no seguinte link:

https://ars.els-cdn.com/content/image/1-s2.0-S1463500318300428-mmc1.pdf

[Research data]

A data é disponibilizada no seguinte link:

http://dx.doi.org/10.17632/fdbj8wz8cm.2

Biogeochemical parameterization

PISCES parameters	Standard value (Kane et al., 2010)	Peru value in reference experiment and in Albert et al. (2010)	Parameter definition
Conc0	2.e-6	–	Phosphate half saturation (μmol P l^{-1})
Conc1	10E-6	–	Phosphate half saturation for diatoms (μmol P l^{-1})
Conc3	0.1E-9	–	Iron half saturation for diatoms (nmol Fe l^{-1})
Grosip	0.151	**0.06** (0.08)	Mean Si/C ratio
Pislope	4	3	*P–I* slope for nano ($(W m^{-2})^{-1} d^{-1}$)
Pislope2	4	3	*P–I* slope for diatoms ($(W m^{-2})^{-1} d^{-1}$)
Excret	0.05	0.1	Excretion ratio of nano
Excret2	0.05	0.1	Excretion ratio of diatoms
Wsbio	3	–	POC sinking speed (m d^{-1})
Wsbio2	50	–	Big particles sinking speed (m d^{-1})
Wchl	0.001	–	Maximum aggregation rate for nano (d^{-1} mol C^{-1})
Wchld	0.02	–	Maximum aggregation rate for diatoms (d^{-1} mol C^{-1})
Resrat	0.03	–	Exsudation rate of zooplankton
Resrat2	0.008	0.005	Exsudation rate of mesozooplankton
Mprat	0.01	–	Phytoplankton mortality rate (d^{-1})
Mprat2	0.01	–	Diatoms mortality rate (d^{-1})
Grazrat	4	–	Maximal zoo grazing rate (d^{-1})
Grazrat2	0.7	–	Maximal mesozoo grazing rate (d^{-1})
Mzrat2	0.03	0.05	Mesozooplankton mortality rate ($(\mu mol C l^{-1}) d^{-1}$)
Xprefc	1	–	Zoo preference for phyto
Xprefp	0	–	Zoo preference for POC
Xprefz	1	–	Zoo preference for zoo
Unass	0.3	–	Nonassimilated fraction of phyto by zoo
Unass2	0.3	–	Nonassimilated fraction of P by mesozoo
Xkgraz	20.E-6	–	Half saturation constant for grazing (μmol C l^{-1})
Xkgraz2	20.E-6	–	Half saturation constant for grazing 2 (μmol C l^{-1})
Xkmort	1.E-7	–	Half saturation constant for mortality (μmol C l^{-1})
Xksi1	2.E-6	1.50E-06	Half saturation constant for Si uptake (μmol Si l^{-1})
Xksi2	3.33E-6	4.00E-06	Half saturation constant for Si/C (μmol Si l^{-1})
Xremip	0.025	–	Remineralization rate of POC (d^{-1})
Xremik	0.3	0.2	Remineralization rate of DOC (d^{-1})
Xsirem	0.015	**0.025** (0.015)	Remineralization rate of Si (d^{-1})
Xkdoc2	417.E-6	–	Second half-sat. of DOC remineralization (μmol C l^{-1})
Xprefpoc	0.2	–	Zoo preference for POC
Concnnh4	1.E-7	–	NH4 half saturation for phyto (μmol P l^{-1})
Concdnh4	5.E-7	–	NH4 half saturation for diatoms (μmol P l^{-1})
Nitrif	0.05	–	NH4 nitrification rate (d^{-1})
Epsher2	0.33	–	Efficiency of mesozoo growth
Epsher	0.33	–	Efficiency of microzoo growth
Sigma1	0.6	–	Fraction of microzoo excretion as DOM-
Sigma2	0.6	–	Fraction of mesozoo excretion as DOM-
Zprefp	0.6	0.5	Microzoo preference for nanophyto
Zprefd	0.5	–	Microzoo preference for diatoms
Chlcnm	0.033	–	Minimum Chl/C in nanophytoplankton (mg Chl/mg C)
Chlcdm	0.05	–	Minimum Chl/C in diatoms (mg Chl/mg C)
cmask	0.1	**0.5** (0.1)	Nearshore source input of iron (non-dimensional)

Figure 1: Biogeochemical parameterization, adapted from Echevin et al. (2014a)

Bibliography

Albert, a., Echevin, V., Lévy, M., e Aumont, O. (2010). Impact of nearshore wind stress curl on coastal circulation and primary productivity in the Peru upwelling system. *Journal of Geophysical Research*, 115(C12):C12033.

Archer, D., Takahashi, T., Sutherland, S., Goddard, J., Chipman, D., Rodgers, K., e Ogura, H. (1996). Daily, seasonal and interannual variability of sea-surface carbon and nutrient concentration in the equatorial pacific ocean. *Deep Sea Research Part II: Topical Studies in Oceanography*, 43(4-6):779–808.

Arruda, R., Calil, P. H., Bianchi, A. A., Doney, S. C., Gruber, N., Lima, I., e Turi, G. (2015). Air-sea co 2 fluxes and the controls on ocean surface pco 2 seasonal variability in the coastal and open-ocean southwestern atlantic ocean: a modeling study. *Biogeosciences*, 12(19):5793–5809.

Aumont, O. e Bopp, L. (2006). Globalizing results from ocean in situ iron fertilization studies. *Global Biogeochemical Cycles*, 20(2).

Aumont, O., Éthé, C., Tagliabue, A., Bopp, L., e Gehlen, M. (2015). Pisces-v2:

an ocean biogeochemical model for carbon and ecosystem studies. *Geoscientific Model Development Discussions*, 8(2).

Aumont, O., Maier-Reimer, E., Blain, S., e Monfray, P. (2003). An ecosystem model of the global ocean including fe, si, p colimitations. *Global Biogeochemical Cycles*, 17(2).

Bakker, D. C., Pfeil, B., Landa, C. S., Metzl, N., O'brien, K. M., Olsen, A., Smith, K., Cosca, C., Harasawa, S., Jones, S. D., et al. (2016). A multi-decade record of high-quality fco 2 data in version 3 of the surface ocean co 2 atlas (socat). *Earth System Science Data*, 8(2):383.

Bakun, A. (1990). Global climate change and intensification of coastal ocean upwelling. *Science*, 247(4939):198–201.

Bakun, A., Black, B. A., Bograd, S. J., Garcia-Reyes, M., Miller, A. J., Rykaczewski, R. R., e Sydeman, W. J. (2015). Anticipated effects of climate change on coastal upwelling ecosystems. *Current Climate Change Reports*, 1(2):85–93.

Bakun, A., Field, D. B., Redondo-Rodriguez, A., e Weeks, S. J. (2010). Greenhouse gas, upwelling-favorable winds, and the future of coastal ocean upwelling ecosystems. *Global Change Biology*, 16(4):1213–1228.

Bakun, A. e Weeks, S. J. (2008). The marine ecosystem off peru: What are the secrets of its fishery productivity and what might its future hold? *Progress in Oceanography*, 79(2):290–299.

Balmaseda, M. A., Vidard, A., e Anderson, D. L. (2008). The ecmwf ocean analysis system: Ora-s3. *Monthly Weather Review*, 136(8):3018–3034.

Barber, R. e Kogelschatz, J. (1990). Nutrients and productivity during the 1982/83 el niño. Em *Elsevier oceanography series*, volume 52, pgs. 21–53. Elsevier.

Behrenfeld, M. J., Boss, E., Siegel, D. A., e Shea, D. M. (2005). Carbon-based ocean productivity and phytoplankton physiology from space. *Global biogeochemical cycles*, 19(1).

Behrenfeld, M. J. e Falkowski, P. G. (1997). Photosynthetic rates derived from satellite-based chlorophyll concentration. *Limnology and oceanography*, 42(1):1–20.

Behrenfeld, M. J., O'Malley, R. T., Siegel, D. A., McClain, C. R., Sarmiento, J. L., Feldman, G. C., Milligan, A. J., Falkowski, P. G., Letelier, R. M., e Boss, E. S. (2006). Climate-driven trends in contemporary ocean productivity. *Nature*, 444(7120):752.

Belmadani, A., Echevin, V., Codron, F., Takahashi, K., e Junquas, C. (2014). What dynamics drive future wind scenarios for coastal upwelling off peru and chile? *Climate dynamics*, 43(7-8):1893–1914.

Bittig, H. C., Steinhoff, T., Claustre, H., Fiedler, B., Williams, N. L., Sauzède, R., Körtzinger, A., e Gattuso, J.-P. (2018). An alternative to static climatologies: Robust estimation of open ocean co2 variables and nutrient concentrations from t, s, and o2 data using bayesian neural networks. *Frontiers in Marine Science*, 5:Art–Nr.

Borges, A., Delille, B., e Frankignoulle, M. (2005). Budgeting sinks and sources of co2 in the coastal ocean: Diversity of ecosystems counts. *Geophysical research letters*, 32(14).

Bosilovich, M. G., Akella, S., Coy, L., Cullather, R., Draper, C., Gelaro, R., Kovach, R., Liu, Q., Molod, A., Norris, P., et al. (2015). Merra-2: Initial evaluation of the climate. *Series on Global Modeling and Data Assimilation, NASA/TM*, 104606.

Bourgeois, T., Orr, J. C., Resplandy, L., Terhaar, J., Ethé, C., Gehlen, M., e Bopp, L. (2016). Coastal-ocean uptake of anthropogenic carbon. *Biogeosciences*, 13(14):4167–4185.

Brady, R. X., Lovenduski, N. S., Alexander, M. A., Jacox, M., e Gruber, N. (2019). On the role of climate modes in modulating the air-sea co2 fluxes in eastern boundary upwelling systems. *Biogeosciences*, 16(2):329–346.

Brink, K., Halpern, D., Huyer, A., e Smith, R. (1983). The physical environment of the peruvian upwelling system. *Progress in Oceanography*, 12(3):285–305.

Brochier, T., Echevin, V., Tam, J., Chaigneau, A., Goubanova, K., e Bertrand, A. (2013). Climate change scenarios experiments predict a future reduction in small pelagic fish recruitment in the humboldt current system. *Global change biology*, 19(6):1841–1853.

Carr, M.-E. (2001). Estimation of potential productivity in eastern boundary currents using remote sensing. *Deep Sea Research Part II: Topical Studies in Oceanography*, 49(1-3):59–80.

Carr, M.-E. e Kearns, E. J. (2003). Production regimes in four eastern boundary current systems. *Deep Sea Research Part II: Topical Studies in Oceanography*, 50(22-26):3199–3221.

Casey, K. S., Brandon, T. B., Cornillon, P., e Evans, R. (2010). The past, present,

and future of the avhrr pathfinder sst program. Em *Oceanography from Space*, pgs. 273–287. Springer.

Chamorro, A., Echevin, V., Colas, F., Oerder, V., Tam, J., e Quispe-Ccalluari, C. (2018). Mechanisms of the intensification of the upwelling-favorable winds during el niño 1997–1998 in the peruvian upwelling system. *Climate Dynamics*, pgs. 1–17.

Chavez, F., Strutton, P., Friederich, G., Feely, R., Feldman, G., Foley, D., e McPhaden, M. (1999). Biological and chemical response of the equatorial pacific ocean to the 1997-98 el niño. *Science*, 286(5447):2126–2131.

Chavez, F., Takahashi, T., Cai, W., Friederich, G., Hales, B., Wanninkhof, R., e Feely, R. (2007). Coastal oceans. *The First State of the Carbon Cycle Report (SOCCR): The North American Carbon Budget and Implications for the Global Carbon Cycle*, pgs. 157–166.

Chelton, D. B., Deszoeke, R. A., Schlax, M. G., El Naggar, K., e Siwertz, N. (1998). Geographical variability of the first baroclinic rossby radius of deformation. *Journal of Physical Oceanography*, 28(3):433–460.

Colas, F., Capet, X., McWilliams, J., e Shchepetkin, a. (2008). 1997–1998 El Niño off Peru: A numerical study. *Progress in Oceanography*, 79(2-4):138–155.

Copin-Montégut, C. e Raimbault, P. (1994). The peruvian upwelling near 15 s in august 1986. results of continuous measurements of physical and chemical properties between 0 and 200 m depth. *Deep Sea Research Part I: Oceanographic Research Papers*, 41(3):439–467.

Dabrowski, T., Lyons, K., Berry, A., Cusack, C., e Nolan, G. D. (2014). An

operational biogeochemical model of the north-east atlantic: model description and skill assessment. *Journal of Marine Systems*, 129:350–367.

Dee, D. P., Uppala, S. M., Simmons, A., Berrisford, P., Poli, P., Kobayashi, S., Andrae, U., Balmaseda, M., Balsamo, G., Bauer, d. P., et al. (2011). The era-interim reanalysis: Configuration and performance of the data assimilation system. *Quarterly Journal of the royal meteorological society*, 137(656):553–597.

Doney, S. C., Lima, I., Feely, R. A., Glover, D. M., Lindsay, K., Mahowald, N., Moore, J. K., e Wanninkhof, R. (2009). Mechanisms governing interannual variability in upper-ocean inorganic carbon system and air–sea co 2 fluxes: Physical climate and atmospheric dust. *Deep Sea Research Part II: Topical Studies in Oceanography*, 56(8):640–655.

Doney, S. C., Ruckelshaus, M., Duffy, J. E., Barry, J. P., Chan, F., English, C. A., Galindo, H. M., Grebmeier, J. M., Hollowed, A. B., Knowlton, N., et al. (2011). Climate change impacts on marine ecosystems.

Echevin, V., Albert, A., Lévy, M., Graco, M., Aumont, O., Piétri, A., e Garric, G. (2014a). Intraseasonal variability of nearshore productivity in the northern humboldt current system: The role of coastal trapped waves. *Continental Shelf Research*, 73:14–30.

Echevin, V., Albert, A., Lévy, M., Graco, M., Aumont, O., Piétri, A., e Garric, G. (2014b). Intraseasonal variability of nearshore productivity in the Northern Humboldt Current System: The role of coastal trapped waves. *Continental Shelf Research*, 73:14–30.

Echevin, V., Aumont, O., Ledesma, J., e Flores, G. (2008a). The seasonal cycle of surface chlorophyll in the peruvian upwelling system: A modelling study. *Progress in Oceanography*, 79(2):167–176.

Echevin, V., Aumont, O., Ledesma, J., e Flores, G. (2008b). The seasonal cycle of surface chlorophyll in the Peruvian upwelling system: A modelling study. *Progress in Oceanography*, 79(2-4):167–176.

Echevin, V., Colas, F., Chaigneau, A., e Penven, P. (2011). Sensitivity of the Northern Humboldt Current System nearshore modeled circulation to initial and boundary conditions. *Journal of Geophysical Research*, 116(C7):C07002.

Espinoza-Morriberón, D., Echevin, V., Colas, F., Tam, J., Ledesma, J., Vásquez, L., e Graco, M. (2017). Impacts of e l n iño events on the p eruvian upwelling system productivity. *Journal of Geophysical Research: Oceans*, 122(7):5423–5444.

Espinoza Morriberón, D., Echevin, V., Colas, F., Tam Málaga, J. L., Gutiérrez Aguilar, D. A., Graco, M. I., Ledesma Rivera, J., e Quispe Ccalluari, C. (2018). Oxygen variability during enso in the tropical south eastern pacific. *Frontiers in Marine Science*, 5:526.

Espinoza-Morriberon, D., Echevin, V., Tam, J., Ledesma, J., Oliveros-Ramos, R., Ramos, J., e Romero, C. Y. (2016). Validación biogeoquímica de una simulación interanual del modelo acoplado roms-pisces en el pacífico sudeste. *Revista peruana de Biología*, 23(2):159–168.

Fay, A. e McKinley, G. (2013). Global trends in surface ocean pco2 from in situ data. *Global Biogeochemical Cycles*, 27(2):541–557.

Feely, R., Takahashi, T., Wanninkhof, R., McPhaden, M., Cosca, C., Sutherland, S., e Carr, M.-E. (2006). Decadal variability of the air-sea co2 fluxes in the equatorial pacific ocean. *Journal of Geophysical Research: Oceans*, 111(C8).

Feely, R. A., Boutin, J., Cosca, C. E., Dandonneau, Y., Etcheto, J., Inoue, H. Y., Ishii, M., Le Quéré, C., Mackey, D. J., McPhaden, M., et al. (2002). Seasonal and interannual variability of co 2 in the equatorial pacific. *Deep Sea Research Part II: Topical Studies in Oceanography*, 49(13):2443–2469.

Feely, R. A., Wanninkhof, R., Cosca, C. E., Murphy, P. P., Lamb, M. F., e Steckley, M. D. (1995). Co2 distributions in the equatorial pacific during the 1991–1992 enso event. *Deep Sea Research Part II: Topical Studies in Oceanography*, 42(2-3):365–386.

Feely, R. A., Wanninkhof, R., Goyet, C., Archer, D. E., e Takahashi, T. (1997). Variability of c02 distributions and sea-air fluxes in the central and eastern equatorial pacific during the 199–1994 el nin o. *Deep Sea Research Part II: Topical Studies in Oceanography*, 44(9-10):1851–1867.

Feely, R. A., Wanninkhof, R., Takahashi, T., e Tans, P. (1999). Influence of el niño on the equatorial pacific contribution to atmospheric co 2 accumulation. *Nature*, 398(6728):597.

Friederich, G., Walz, P., Burczynski, M., e Chavez, F. (2002). Inorganic carbon in the central california upwelling system during the 1997–1999 el niño–la niña event. *Progress in Oceanography*, 54(1):185–203.

Friederich, G. E., Ledesma, J., Ulloa, O., e Chavez, F. P. (2008). Air–sea carbon

dioxide fluxes in the coastal southeastern tropical pacific. *Progress in Oceanography*, 79(2):156–166.

Garcia, H., Locarnini, R., Boyer, T., Antonov, J., Baranova, O., Zweng, M., Reagan, J., e Johnson, D. (2014). World ocean atlas 2013, volume 3: Dissolved oxygen, apparent oxygen utilization, and oxygen saturation. *NOAA Atlas NESDIS*, 75:27.

Garcia, H. E., Locarnini, R. A., Boyer, T. P., Antonov, J. I., Baranova, O. K., Zweng, M. M., Reagan, J. R., Johnson, D. R., Mishonov, A. V., e Levitus, S. (2013). World ocean atlas 2013. volume 4, dissolved inorganic nutrients (phosphate, nitrate, silicate).

García-Reyes, M., Sydeman, W. J., Black, B., Rykaczewski, R., Schoeman, D., Thompson, S., e Bograd, S. (2013). Relative influence of oceanic and terrestrial pressure systems in driving upwelling-favorable winds. *Geophysical Research Letters*, 40(19):5311–5315.

Garric, G., Parent, L., Greiner, E., Drévillon, M., Hamon, M., Lellouche, J.-M., Régnier, C., Desportes, C., Le Galloudec, O., Bricaud, C., et al. (2017). Performance and quality assessment of the global ocean eddy-permitting physical reanalysis glorys2v4. Em *EGU General Assembly Conference Abstracts*, volume 19, pg. 18776.

GLOBALVIEW-CO2 (2013). Cooperative global atmospheric data integration project. 2013, updated annually. multi-laboratory compilation of synchronized and gap-filled atmospheric carbon dioxide records for the period 1979-2012. Compiled by NOAA Global Monitoring Division Boulder, Colorado, U.S.A.

Good, S. A., Martin, M. J., e Rayner, N. A. (2013). En4: Quality controlled ocean

temperature and salinity profiles and monthly objective analyses with uncertainty estimates. *Journal of Geophysical Research: Oceans*, 118(12):6704–6716.

Graco, M. I., Ledesma, J., Flores, G., e Girón, M. (2007). Nutrientes, oxígeno y procesos biogeoquímicos en el sistema de surgencias de la corriente de humboldt frente a perú. *Revista peruana de biología*, 14(1):117–128.

Gruber, N. (2011). Warming up, turning sour, losing breath: ocean biogeochemistry under global change. *Philosophical Transactions of the Royal Society of London A: Mathematical, Physical and Engineering Sciences*, 369(1943):1980–1996.

Gruber, N., Gloor, M., Fletcher, S. E. M., Doney, S. C., Dutkiewicz, S., Follows, M. J., Gerber, M., Jacobson, A. R., Joos, F., Lindsay, K., et al. (2009). Oceanic sources, sinks, and transport of atmospheric co2. *Global Biogeochemical Cycles*, 23(1).

Gruber, N., Lachkar, Z., Frenzel, H., Marchesiello, P., Münnich, M., McWilliams, J. C., Nagai, T., e Plattner, G.-K. (2011). Eddy-induced reduction of biological production in eastern boundary upwelling systems. *Nature geoscience*, 4(11):787–792.

Hales, B., Takahashi, T., e Bandstra, L. (2005). Atmospheric co2 uptake by a coastal upwelling system. *Global Biogeochemical Cycles*, 19(1).

Hauri, C., Gruber, N., Plattner, G.-K., Alin, S., Feely, R. A., Hales, B., e Wheeler, P. A. (2009). Ocean acidification in the california current system. *Oceanography*, 22(4):60–71.

Huyer, A., Knoll, M., Paluszkiewicz, T., e Smith, R. L. (1991). The peru undercurrent:

a study in variability. *Deep Sea Research Part A. Oceanographic Research Papers*, 38:S247–S271.

Inoue, H. Y. e Sugimura, Y. (1992). Variations and distributions of co2 in and over the equatorial pacific during the period from the 1986/88 el niño event to the 1988/89 la niña event. *Tellus B*, 44(1):1–22.

Iriarte, J. L. e González, H. E. (2004). Phytoplankton size structure during and after the 1997/98 el niño in a coastal upwelling area of the northern humboldt current system. *Marine ecology progress series*, 269:83–90.

Ishii, M., Feely, R. A., Rodgers, K. B., Park, G.-H., Wanninkhof, R., Sasano, D., Sugimoto, H., Cosca, C., Nakaoka, S.-i., Telszewski, M., et al. (2014). Air-sea co2 flux in the pacific ocean for the period 1990–2009.

Jähne, B. e Haußecker, H. (1998). Air-water gas exchange. *Annual Review of Fluid Mechanics*, 30(1):443–468.

Jones, C. D., Collins, M., Cox, P. M., e Spall, S. A. (2001). The carbon cycle response to enso: A coupled climate–carbon cycle model study. *Journal of Climate*, 14(21):4113–4129.

Key, R. M., Olsen, A., van Heuven, S., Lauvset, S. K., Velo, A., Lin, X., Schirnick, C., Kozyr, A., Tanhua, T., Hoppema, M., et al. (2015). Global ocean data analysis project, version 2 (glodapv2).

Kubota, M., Iwasaka, N., Kizu, S., Konda, M., e Kutsuwada, K. (2002). Japanese ocean flux data sets with use of remote sensing observations (j-ofuro). *Journal of Oceanography*, 58(1):213–225.

Lachkar, Z. e Gruber, N. (2011). What controls biological production in coastal upwelling systems? insights from a comparative modeling study. *Biogeosciences*, 8(10):2961–2976.

Lachkar, Z. e Gruber, N. (2013). Response of biological production and air–sea co 2 fluxes to upwelling intensification in the california and canary current systems. *Journal of Marine Systems*, 109:149–160.

Landschützer, P., Gruber, N., Bakker, D., Landschützer, P., Bakker, D., Haumann, F., Rödenbeck, C., van Heuven, S., Hoppema, N. M., Sweeney, C., et al. (2015a). A 30 years observation-based global monthly gridded sea surface pco2 product from 1982 through 2011. *Carbon Dioxide Information Analysis Center, Oak Ridge National Laboratory, US Department of Energy, Oak Ridge, TN*.

Landschützer, P., Gruber, N., Bakker, D., e Schuster, U. (2014). Recent variability of the global ocean carbon sink. *Global Biogeochemical Cycles*, 28(9):927–949.

Landschützer, P., Gruber, N., Haumann, F. A., Rödenbeck, C., Bakker, D. C., Van Heuven, S., Hoppema, M., Metzl, N., Sweeney, C., Takahashi, T., et al. (2015b). The reinvigoration of the southern ocean carbon sink. *Science*, 349(6253):1221–1224.

Laruelle, G. G., Landschützer, P., Gruber, N., Tison, J.-L., Delille, B., e Regnier, P. (2017). Global high-resolution monthly p co 2 climatology for the coastal ocean derived from neural network interpolation. *Biogeosciences*, 14(19):4545.

Lauvset, S. K., Key, R. M., e Perez, F. F. (2016). A new global interior ocean mapped climatology: the 1x1 glodap version 2. *Earth System Science Data*, 8(2):325.

Lee, Z., Weidemann, A., Kindle, J., Arnone, R., Carder, K. L., e Davis, C. (2007). Euphotic zone depth: Its derivation and implication to ocean-color remote sensing. *Journal of Geophysical Research: Oceans*, 112(C3).

Liu, W. T., Tang, W., e Polito, P. S. (1998). Nasa scatterometer provides global ocean-surface wind fields with more structures than numerical weather prediction. *Geophysical Research Letters*, 25(6):761–764.

Lovenduski, N. S., Gruber, N., Doney, S. C., e Lima, I. D. (2007). Enhanced co2 outgassing in the southern ocean from a positive phase of the southern annular mode. *Global Biogeochemical Cycles*, 21(2).

Marchesiello, P., McWilliams, J. C., e Shchepetkin, A. (2003). Equilibrium structure and dynamics of the california current system. *Journal of Physical Oceanography*, 33(4):753–783.

Maréchal, D. (2004). A soil-based approach to rainfall-runoff modelling in ungauged catchments for england and wales.

McKinley, G. A., Follows, M. J., e Marshall, J. (2004). Mechanisms of air-sea co2 flux variability in the equatorial pacific and the north atlantic. *Global Biogeochemical Cycles*, 18(2).

Meehl, G. A. e Washington, W. M. (1996). El niño-like climate change in a model with increased atmospheric co2 concentrations. *Nature*, 382(6586):56.

Messié, M., Ledesma, J., Kolber, D. D., Michisaki, R. P., Foley, D. G., e Chavez, F. P. (2009). Potential new production estimates in four eastern boundary upwelling ecosystems. *Progress in Oceanography*, 83(1):151–158.

Millero, F. J. (2007). The marine inorganic carbon cycle. *Chemical reviews*, 107(2):308–341.

Mogollón, R. e Calil, P. H. (2017). On the effects of enso on ocean biogeochemistry in the northern humboldt current system (nhcs): A modeling study. *Journal of Marine Systems*.

Mogollón, R. e Calil, P. H. (2018a). Counterintuitive effects of global warming-induced wind patterns on primary production in the northern humboldt current system. *Global Change Biology*, 24(7):3187–3198.

Mogollón, R. e Calil, P. H. (2018b). Modelling the mechanisms and drivers of the spatiotemporal variability of pco2 and air–sea co2 fluxes in the northern humboldt current system. *Ocean Modelling*, 132:61–72.

Moll, A. e Radach, G. (2003). Review of three-dimensional ecological modelling related to the north sea shelf system: Part 1: models and their results. *Progress in Oceanography*, 57(2):175–217.

Montégut, C. D. B., Madec, G., Fischer, A. S., Lazar, A., e Iudicone, D. (2004). Mixed layer depth over the global ocean: An examination of profile data and a profile-based climatology. *Journal of Geophysical Research*, 109:C12003.

Montes, I., Colas, F., Capet, X., e Schneider, W. (2010). On the pathways of the equatorial subsurface currents in the eastern equatorial Pacific and their contributions to the Peru-Chile Undercurrent. *Journal of Geophysical Research*, 115(C9):C09003.

Montes, I., Dewitte, B., Gutknecht, E., Paulmier, A., Dadou, I., Oschlies, A., e Garçon, V. (2014). High-resolution modeling of the eastern tropical pacific

oxygen minimum zone: Sensitivity to the tropical oceanic circulation. *Journal of Geophysical Research: Oceans*, 119(8):5515–5532.

Montes, I., Schneider, W., Colas, F., Blanke, B., e Echevin, V. (2011). Subsurface connections in the eastern tropical Pacific during La Niña 1999–2001 and El Niño 2002–2003. *Journal of Geophysical Research*, 116(C12):C12022.

Narayan, N., Paul, A., Mulitza, S., e Schulz, M. (2010). Trends in coastal upwelling intensity during the late 20th century. *Ocean Science*, 6(3):815.

Ñiquen, M. e Bouchon, M. (2004). Impact of el niño events on pelagic fisheries in peruvian waters. *Deep sea research part II: topical studies in oceanography*, 51(6-9):563–574.

Olsen, A., Key, R. M., van Heuven, S., Lauvset, S. K., Velo, A., Lin, X., Schirnick, C., Kozyr, A., Tanhua, T., Hoppema, M., et al. (2016). The global ocean data analysis project version 2 (glodapv2)–an internally consistent data product for the world ocean. *Earth System Science Data*, 8(2):297.

Oort, A. H. e Yienger, J. J. (1996). Observed interannual variability in the hadley circulation and its connection to enso. *Journal of Climate*, 9(11):2751–2767.

Pauly, D. e Christensen, V. (1995). Primary production required to sustain global fisheries. *Nature*, 374(6519):255–257.

Pennington, J. T., Mahoney, K. L., Kuwahara, V. S., Kolber, D. D., Calienes, R., e Chavez, F. P. (2006). Primary production in the eastern tropical pacific: A review. *Progress in Oceanography*, 69(2):285–317.

Penven, P. (2005). Average circulation, seasonal cycle, and mesoscale dynamics of the Peru Current System: A modeling approach. *Journal of Geophysical Research*, 110(C10):C10021.

Peters, W., Jacobson, A. R., Sweeney, C., Andrews, A. E., Conway, T. J., Masarie, K., Miller, J. B., Bruhwiler, L. M., Pétron, G., Hirsch, A. I., et al. (2007). An atmospheric perspective on north american carbon dioxide exchange: Carbontracker. *Proceedings of the National Academy of Sciences*, 104(48):18925–18930.

Quispe, J. e Vásquez Espinoza, L. (2015). índice" labcos" para la caracterización de eventos el niño y la niña frente a la costa del perú, 1976-205.

Rayner, P. J., Law, R. M., e Dargaville, R. (1999). The relationship between tropical co2 fluxes and the el niño-southern oscillation. *Geophysical Research Letters*, 26(4):493–496.

Risien, C. M. e Chelton, D. B. (2008). A global climatology of surface wind and wind stress fields from eight years of quikscat scatterometer data. *Journal of Physical Oceanography*, 38(11):2379–2413.

Rödenbeck, C., Bakker, D. C., Metzl, N., Olsen, A., Sabine, C. L., Cassar, N., Reum, F., Keeling, R. F., e Heimann, M. (2014). Interannual sea-air co 2 flux variability from an observation-driven ocean mixed-layer scheme. *Biogeosciences Discussions*, 11:3167–3207.

Rykaczewski, R. R. e Dunne, J. P. (2010). Enhanced nutrient supply to the california current ecosystem with global warming and increased stratification in an earth system model. *Geophysical Research Letters*, 37(21).

Rykaczewski, R. R., Dunne, J. P., Sydeman, W. J., García-Reyes, M., Black, B. A., e Bograd, S. J. (2015). Poleward displacement of coastal upwelling-favorable winds in the ocean's eastern boundary currents through the 21st century. *Geophysical Research Letters*, 42(15):6424–6431.

Salvatteci, R., Field, D., Gutiérrez, D., Baumgartner, T., Ferreira, V., Ortlieb, L., Sifeddine, A., Grados, D., e Bertrand, A. (2018). Multifarious anchovy and sardine regimes in the humboldt current system during the last 150 years. *Global Change Biology*, 24(3):1055–1068.

Sanchez, G., Calienes, R., e Zuta, S. (2000). The 1997-98 el niño and its effects on the coastal marine ecosystem off peru. *Reports of California Cooperative Oceanic Fisheries Investigations*, 41:62–86.

Sarmiento, J. L. e Gruber, N. (2006). Ocean biogeochemical dynamics.

Sarmiento, J. L., Slater, R., Barber, R., Bopp, L., Doney, S. C., Hirst, A., Kleypas, J., Matear, R., Mikolajewicz, U., Monfray, P., et al. (2004). Response of ocean ecosystems to climate warming. *Global Biogeochemical Cycles*, 18(3).

Sauzède, R., Bittig, H. C., Claustre, H., Pasqueron de Fommervault, O., Gattuso, J.-P., Legendre, L., e Johnson, K. S. (2017). Estimates of water-column nutrient concentrations and carbonate system parameters in the global ocean: A novel approach based on neural networks. *Frontiers in Marine Science*, 4:128.

Shchepetkin, A. F. e McWilliams, J. C. (2005). The regional oceanic modeling system (ROMS): a split-explicit, free-surface, topography-following-coordinate oceanic model. *Ocean Modelling*, 9(4):347–404.

Shchepetkin, A. F. e McWilliams, J. C. (2009). Correction and commentary for "Ocean forecasting in terrain-following coordinates: Formulation and skill assessment of the regional ocean modeling system" by Haidvogel et al., J. Comp. Phys. 227, pp. 3595–3624. *Journal of Computational Physics*, 228(24):8985–9000.

Signorini, S. R., Mannino, A., Najjar, R. G., Friedrichs, M. A., Cai, W.-J., Salisbury, J., Wang, Z. A., Thomas, H., e Shadwick, E. (2013). Surface ocean pco2 seasonality and sea-air co2 flux estimates for the north american east coast. *Journal of Geophysical Research: Oceans*, 118(10):5439–5460.

Simpson, J. J. e Zirino, A. (1980). Biological control of ph in the peruvian coastal upwelling area. *Deep Sea Research Part A. Oceanographic Research Papers*, 27(9):733–743.

Stocker, T. (2014). *Climate change 2013: the physical science basis: Working Group I contribution to the Fifth assessment report of the Intergovernmental Panel on Climate Change*. Cambridge University Press.

Storto, A., Masina, S., e Navarra, A. (2015). Evaluation of the cmcc eddy-permitting global ocean physical reanalysis system (c-glors, 1982–2012) and its assimilation components. *Quarterly Journal of the Royal Meteorological Society*.

Stow, C. A., Jolliff, J., McGillicuddy Jr, D. J., Doney, S. C., Allen, J. I., Friedrichs, M. A., Rose, K. A., e Wallhead, P. (2009). Skill assessment for coupled biological/physical models of marine systems. *Journal of Marine Systems*, 76(1-2):4–15.

Stramma, L., Johnson, G. C., Sprintall, J., e Mohrholz, V. (2008). Expanding oxygen-minimum zones in the tropical oceans. *science*, 320(5876):655–658.

Strub, P. T., Combes, V., Shillington, F. A., e Pizarro, O. (2013). Currents and processes along the eastern boundaries. *Ocean Circulation and Climate: A 21st Century Perspective*, pgs. 339–384.

Strub, P. T., Mesías, J. M., Montecino, V., Rutlant, J., e Salinas, S. (1998). Strub et al 1998.pdf. Em Robinson, A. R. e Brink, K. H., editores, *The Sea, Volume 11*, capítulo Coastal oc, pgs. 273–314.

Sydeman, W., García-Reyes, M., Schoeman, D., Rykaczewski, R., Thompson, S., Black, B., e Bograd, S. (2014). Climate change and wind intensification in coastal upwelling ecosystems. *Science*, 345(6192):77–80.

Takahashi, K., Mosquera, K., e Reupo, J. (2014). El índice costero el niño (icen): historia y actualización. *Boletín Técnico del Instituto Geofísico del Perú*, 1:8–9.

Takahashi, T., Sutherland, S. C., Feely, R. A., e Cosca, C. E. (2003). Decadal variation of the surface water pco2 in the western and central equatorial pacific. *Science*, 302(5646):852–856.

Takahashi, T., Sutherland, S. C., e Kozyr, A. (2018). Global ocean surface water partial pressure of co2 database: Measurements performed during 1957–2017 (version 2017).

Takahashi, T., Sutherland, S. C., Wanninkhof, R., Sweeney, C., Feely, R. A., Chipman, D. W., Hales, B., Friederich, G., Chavez, F., Sabine, C., et al. (2009). Climatological mean and decadal change in surface ocean pco2, and net sea–air co2 flux over the global oceans. *Deep Sea Research Part II: Topical Studies in Oceanography*, 56(8-10):554–577.

Takahashi K., Mosquera K., R. J. (2014). El Índice costero el niño (icen): historia y actualización, boletín técnico "generación de modelos climáticos para el pronóstico de la ocurrencia del fenómeno el niño. Instituto Geofísico del Perú. 1, 2, 8-9.

Tanhua, T., Bates, N. R., e Körtzinger, A. (2013). The marine carbon cycle and ocean carbon inventories. Em *International Geophysics*, volume 103, pgs. 787–815. Elsevier.

Tegen, I. e Fung, I. (1995). Contribution to the atmospheric mineral aerosol load from land surface modification. *Journal of Geophysical Research: Atmospheres*, 100(D9):18707–18726.

Torres, R., Turner, D. R., Rutllant, J., e Lefèvre, N. (2003). Continued co2 outgassing in an upwelling area off northern chile during the development phase of el niño 1997–1998 (july 1997). *Journal of Geophysical Research: Oceans*, 108(C10).

Torres, R., Turner, D. R., Silva, N., e Rutllant, J. (1999). High short-term variability of co2 fluxes during an upwelling event off the chilean coast at 30 s. *Deep Sea Research Part I: Oceanographic Research Papers*, 46(7):1161–1179.

Trenberth, K. E., Stepaniak, D. P., e Caron, J. M. (2002). Interannual variations in the atmospheric heat budget. *Journal of Geophysical Research: Atmospheres*, 107(D8):AAC–4.

Turi, G., Lachkar, Z., e Gruber, N. (2014). Spatiotemporal variability and drivers of pco 2 and air–sea co 2 fluxes in the california current system: an eddy-resolving modeling study. *Biogeosciences*, 11(3):671–690.

Van Heuven, S., Pierrot, D., Rae, J., Lewis, E., e Wallace, D. (2011). Matlab program

developed for co2 system calculations. *Oak Ridge, Tennessee: Carbon Dioxide Information Analysis Center, Oak Ridge National Laboratory, US Department of Energy. pp. ORNL/CDIAC-105b*.

Wanninkhof, R. (1992). Relationship between wind speed and gas exchange over the ocean. *Journal of Geophysical Research: Oceans*, 97(C5):7373–7382.

Wanninkhof, R. (2014). Relationship between wind speed and gas exchange over the ocean revisited. *Limnology and Oceanography: Methods*, 12(6):351–362.

Wanninkhof, R., Park, G.-H., Takahashi, T., Sweeney, C., Feely, R. A., Nojiri, Y., Gruber, N., Doney, S. C., McKinley, G. A., Lenton, A., et al. (2013). Global ocean carbon uptake: magnitude, variability and trends.

Weatherall, P., Marks, K., Jakobsson, M., Schmitt, T., Tani, S., Arndt, J. E., Rovere, M., Chayes, D., Ferrini, V., e Wigley, R. (2015). A new digital bathymetric model of the world's oceans. *Earth and Space Science*, 2(8):331–345.

Weiss, R. (1974). Carbon dioxide in water and seawater: the solubility of a non-ideal gas. *Marine chemistry*, 2(3):203–215.

Wentz, F., Scott, J., Hoffman, R., Leidner, M., Atlas, R., e Ardizzone, J. (2015). Remote sensing systems cross-calibrated multi-platform (ccmp) 6-hourly ocean vector wind analysis product on 0.25 deg grid, version 2.0. *Proc. Remote Sens. Syst*.

Westberry, T., Behrenfeld, M., Siegel, D., e Boss, E. (2008). Carbon-based primary productivity modeling with vertically resolved photoacclimation. *Global Biogeochemical Cycles*, 22(2).

Williams, R. G. e Follows, M. J. (2011). *Ocean dynamics and the carbon cycle: Principles and mechanisms*. Cambridge University Press.